VNiVERSiDAD Đ SALAMANCA

CAMPUS DE EXCELENCIA INTERNACIONAL

Departamento de Ingeniería Cartográfica y del Terreno

Tesis doctoral

Desarrollo de geotecnologías aplicadas a la inspección y monitorización de entornos industriales

Esteban Ruiz de Oña Crespo

2023

Universidad de Salamanca

Escuela Politécnica Superior de Ávila

Departamento de Ingeniería Cartográfica y del Terreno

Autor:

Esteban Ruiz de Oña Crespo

Directores:

Dr. Pablo Rodríguez Gonzálvez
Dr. Manuel Rodríguez Martín

2023

Informe de los directores de Tesis

La presente Tesis Doctoral titulada *"Desarrollo de geotecnologías aplicadas a la inspección y monitorización de entornos industriales"* realizada y presentada por D. Esteban Ruiz de Oña Crespo, es el resultado de un proceso investigador llevado a cabo por el doctorando a lo largo de cinco cursos académicos, que ha cristalizado en la verticalización de varios desarrollos software con orientación comercial, todos ellos en relación con la aplicación de técnicas geomáticas para la solución de necesidades del ámbito del mantenimiento de instalaciones industriales. La totalidad de la Tesis Doctoral se ha desarrollado dentro del marco de los proyectos SMART-WELD e INSPECTOR acometidos por la empresa Itos3D Engineering S.L., con la cual el doctorando tiene contrato vigente desde el año 2016.

Los resultados obtenidos con las metodologías presentadas dieron lugar a la publicación de artículos científicos, cuatro de los cuales se incluyen en el presente documento. Cabe destacar la gran calidad de los artículos incluidos en esta tesis, refrendada por su publicación en revistas internacionales de prestigio y de acceso abierto, sometidas a un proceso de revisión anónimo por pares e indexadas en el cuartil segundo del Journal Citation Report (JCR). Estos, por orden de calidad de la publicación, se distribuyen del siguiente modo:

- Un artículo en la revista "Remote Sensing" indexada en el JCR en la 9ª posición dentro de la categoría de teledetección, en la que hay 30 revistas (2º cuartil) en el año de publicación.

- Dos artículos en la revista "Applied Sciences" indexada en el JCR en la 39ª posición dentro de la categoría de ingeniería multidisciplinar, en la que hay 92 revistas (2º cuartil), según los últimos datos disponibles a fecha del presente informe.

- Un artículo en la revista "Drones" indexada en el JCR en la 10ª posición dentro de la categoría de teledetección, en la que hay 34 revistas (2º cuartil), según los últimos datos disponibles a fecha del presente informe.

Como se reseñó anteriormente, el doctorado ha participado activamente en creación de varias herramientas software, todas ellas protegidas bajo el registro

nacional de la propiedad intelectual relativas a tareas de inspección y monitorización de diversos entornos industriales mediante la aplicación de geotecnologías; dichas soluciones (WeldMap, SunMap & InspectorMap) acompañan a otra serie de librerías y desarrollos distribuidos bajo licencia de software libre con el consecuente beneficio de toda la comunidad científica.

En consecuencia, la Tesis Doctoral *"Desarrollo de geotecnologías aplicadas a la inspección y monitorización de entornos industriales"* realizada por D. Esteban Ruiz de Oña Crespo, se ajusta, de forma óptima, a las condiciones requeridas para la presentación de la misma por la modalidad de "Compendio de publicaciones", conforme los requisitos expuestos en el Reglamento de Doctorado de la Universidad de Salamanca; así como a ser candidata a la "Mención Industrial" dado que presenta resultados originales y suficientes de acuerdo a los requisitos y reglamentos establecidos por la Universidad de Salamanca y el artículo 15 bis del Real Decreto 195/2016 publicado en el BOE del 3 de Junio de 2016 sobre Mención Industrial en el título de Doctor en este aspecto.

Por todos los motivos mencionados, esta Tesis Doctoral es favorable para obtener el grado de Doctor por la Universidad de Salamanca en el programa de doctorado en Geotecnologías Aplicadas a la Construcción, Energía e Industria.

Lo que firman, a todos los efectos oportunos, en Ávila, a 7 de junio de 2023

Dr. Pablo Rodríguez Gonzálvez   Dr. Manuel Rodríguez Martín

Listado de artículos publicados

La presente tesis doctoral está constituida por un compendio de cuatro artículos científicos, publicados en revistas internacionales de alto impacto. A continuación, se enumeran estas publicaciones:

1. **WELDMAP: A Photogrammetric Suite Applied to the Inspection of Welds**

   Esteban Ruiz de Oña Crespo[1], Manuel Rodríguez Martín[2], Pablo Rodríguez Gonzálvez[3], Rocío Mora[1] and Diego González Aguilera[1]

   [1] Department of Cartographic and Land Engineering, Higher Polytechnic School of Ávila, Universidad de Salamanca, Hornos Caleros 50, 05003 Ávila, Spain
   [2] Department of Mechanical Engineering, Higher Polytechnic School of Zamora, Campus Viriato, Universidad de Salamanca, Avenida Requejo 33, 49022 Zamora, Spain
   [3] Department of Mining Technology, Topography and Structures, Universidad de León, Av. Astorga s/n, 24401 Ponferrada, Spain

2. **Validation of Portable Mobile Mapping System for Inspection Tasks in Thermal and Fluid–Mechanical Facilities**

   Manuel Rodríguez Martín[1,2], Pablo Rodríguez Gonzálvez[3], Esteban Ruiz de Oña Crespo[4] and Diego González Aguilera[4]

   [1] Department of Mechanical Engineering, Universidad de Salamanca, 37700, Béjar (Salamanca), Spain
   [2] Technological Department, Catholic University of Ávila, 05005, Ávila, Spain
   [3] Department of Mining Technology, Topography and Structures. Universidad de León, 24401, Ponferrada (Spain), Spain
   [4] Department of Cartographic and Land Engineering. Universidad de Salamanca, 05003, Ávila, Spain

3. **SunMap: Towards Unattended Maintenance of Photovoltaic Plants Using Drone Photogrammetry**

David Hernández López[1], Esteban Ruíz de Oña[2], Miguel A. Moreno[1] and Diego González Aguilera[2]

[1] Institute for Regional Development, University of Castilla la Mancha, Campus Universitario s/n, 02071 Albacete, Spain
[2] Department of Cartographic and Land Engineering, Higher Polytechnic School of Ávila, University of Salamanca, Hornos Caleros 50, 05003 Ávila, Spain

4. **INSPECTORMAP: A Spatial Data Infrastructure Applied to the Maintenance of Solar Plants Using Free Satellite Imagery**

Esteban Ruiz de Oña Crespo, María Sánchez Aparicio, Susana del Pozo and Diego González Aguilera

Department of Cartographic and Land Engineering, Higher Polytechnic School of Ávila, University of Salamanca, Hornos Caleros 50, 05003 Ávila, Spain

Resumen

El desarrollo tecnológico de las últimas dos décadas ha supuesto un cambio radical que está llevando a un nuevo paradigma en el que se entremezclan el mundo físico y el digital. Estos cambios han influido enormemente en la sociedad, modificando las formas de comunicación, acceso a información, ocio, trabajo, etc. Asimismo, la industria ha adoptado estas tecnologías disruptivas, las cuales están contribuyendo a lograr un mayor control y automatización del proceso productivo. En el ámbito industrial, las tareas de mantenimiento son críticas para garantizar el correcto funcionamiento de una planta o instalación, ya que influyen directamente en la productividad y pueden suponer un elevado costo adicional. Las nuevas tecnologías están posibilitando la monitorización continua y a la inspección automatizada, proporcionando herramientas auxiliares a los inspectores que mejoran la detección de fallos y permiten anticipar y optimizar la planificación de las tareas de mantenimiento.

Con el objetivo de desarrollar herramientas que aporten mejoras en las tareas de mantenimiento en industria, la presente tesis doctoral se basa en el estudio de como las geotecnologías pueden aportar soluciones óptimas en la monitorización e inspección. Debido a la gran variedad de entornos industriales, las herramientas de apoyo al mantenimiento deben adaptarse a cada caso en concreto. En este aspecto, y con el fin de demostrar la adaptabilidad de la geomática y las geotecnologías, se han estudiado instalaciones industriales de ámbitos muy diversos, como una sala de máquinas (escenario interior), plantas fotovoltaicas (escenario exterior) y soldaduras (interior y exterior).

La escala de los escenarios objeto de estudio ha sido muy variada, desde las escalas más pequeñas, para el estudio de las soldaduras y la sala de máquinas, a las escalas más grandes, en los estudios de evolución de la vegetación y presencia de masas de agua en plantas fotovoltaicas. Las geotecnologías demuestran su versatilidad para trabajar a distintas escalas, con soluciones que permiten un gran detalle y precisión, como la fotogrametría de rango cercano y el sistema de escaneado portátil (Portable Mobile Mapping System - PMMS), y otras que pueden abarcar zonas más amplias del territorio, como es el caso de la teledetección o la fotogrametría con drones.

Según lo expuesto anteriormente, el enfoque de la tesis ha sido el estudio de

elementos o instalaciones industriales a diferentes escalas. En el primer caso se desarrolló una herramienta para el control de calidad externo de soldaduras utilizando fotogrametría de rango cercano y algoritmos para la detección automática de defectos. En el segundo caso se propuso el uso de un PMMS para optimizar la toma de datos en tareas de inspección en instalaciones fluidomecánicas. En el tercer caso se utilizó la fotogrametría con drones y la combinación de imágenes RGB y térmicas con algoritmos de visión computacional para la detección de patologías en paneles fotovoltaicos. Finalmente, para la monitorización de la vegetación y la detección de masas de agua en el entorno de plantas fotovoltaicas, se empleó la teledetección mediante el cálculo de índices espectrales.

Abstract

The technological development of the last two decades has brought about a radical change that is leading to a new paradigm in which the physical and digital worlds are intertwined. These changes have had a great impact on society, modifying communication methods, access to information, leisure, work, etc. In addition, the industry has adopted these disruptive technologies, which are contributing to achieving greater control and automation of the production process. In the industrial sector, maintenance tasks are critical to ensuring the proper operation of a plant or facility, as they directly influence productivity and can involve high additional costs. New technologies are making continuous monitoring and automated inspection possible, providing auxiliary tools to inspectors that improve fault detection and allow for the anticipation and optimization of maintenance task planning.

With the aim of developing tools that provide improvements in maintenance tasks in industry, this doctoral thesis is based on the study of how geotechnologies can provide optimal solutions in monitoring and inspection. Due to the great variety of industrial environments, maintenance support tools must adapt to each specific case. In this regard, and in order to demonstrate the adaptability of geomatics and geotechnologies, industrial installations from very diverse areas have been studied, such as a machine room (indoor scenario), photovoltaic plants (outdoor scenario), and welding (indoor and outdoor scenarios).

The scale of the studied scenarios has been very varied, ranging from smaller scales for the study of welds and machine rooms, to larger scales in the studies of vegetation evolution and the presence of bodies of water in photovoltaic plants. Geotechnologies demonstrate their versatility to work at different scales, with solutions that allow for great detail and precision, such as close-range photogrammetry and the Portable Mobile Mapping System (PMMS), as well as others that can cover larger areas of the territory, such as remote sensing or photogrammetry with drones.

The focus of the thesis has been the study of industrial elements or installations at different scales. In the first case, a tool was developed for external quality control of welding, using close-range photogrammetry and algorithms for automatic defect detection. In the second case, the use of a PMMS is proposed to optimize data

collection in fluid-mechanical installation inspection tasks. In the third case, drone photogrammetry and the combination of RGB and thermal images with computer vision algorithms were used for the detection of pathologies in photovoltaic panels. Finally, for the monitoring of vegetation and the detection of water masses in the environment of photovoltaic plants, remote sensing was employed through the calculation of spectral indices.

Índice general

Índice de figuras

Capítulo 1

Introducción

Capítulo 1

Introducción

En toda planta o instalación industrial se deben realizar periódicamente inspecciones de mantenimiento de toda máquina, equipo o instalación que sea fundamental para el correcto funcionamiento de las mismas. Estas inspecciones tienen el objetivo de examinar y evaluar los equipos, comprobando si estos están operando normalmente e identificando fallas que deberán ser corregidas mediante un mantenimiento correctivo.

Históricamente, desde la Primera Revolución Industrial, el mantenimiento se ejecutaba cuando era estrictamente necesario, es decir, cuando algún elemento fallaba y era necesario arreglarlo o reemplazarlo [1]. Con la posguerra y el auge de la producción se produjo un gran avance en la recopilación y evaluación de datos, así como la mejora de los requisitos de calidad de los productos. La necesidad de reducir los tiempos de inactividad de los equipos, debido al alto coste asociado a la falta de productividad durante esos periodos, hizo necesaria una planificación de las actividades de mantenimiento.

El impacto del mantenimiento, la reparación y la renovación en plantas e instalaciones industriales supone entre un 15 y un 60 % de su coste operativo total[2]. Otros autores cifran el gasto en más de 1.500 millones de euros al año sólo en la Unión Europea y más de 7.000 millones de euros en todo el mundo[3]. Por otra parte, más de 50 millones de empleos están directamente vinculados al mantenimiento y 150 millones indirectamente[3]. A esto se une que las regulaciones y la legislación cada vez son más exigentes en criterios ambientales y de seguridad. Debido a estos motivos la industria ha tenido que adaptarse adoptando nuevas tecnologías que permitan automatizar en gran medida las tareas de mantenimiento y anticiparse al fallo. En este contexto de incorporación de nuevas tecnologías disruptivas surge la Industria 4.0 y, asociada a ella, el Mantenimiento 4.0.

1.1. Monitorización e inspección en industria

1.1.1. Industria 4.0

Desde los inicios de la industrialización, los grandes saltos tecnológicos han dado lugar a cambios de paradigma que *a posteriori* se han definido como **revoluciones industriales**[4], dando como resultado profundas transformaciones económicas y sociales. La **Primera Revolución Industrial** supuso la transformación de las sociedades agrarias y rurales en industriales y urbanas. El trabajo manual y de tracción animal fue sustituido por maquinaría, siendo la máquina de vapor el gran avance que permitió el rápido desarrollo de esta época. La **Segunda Revolución Industrial** fue impulsada por nuevas formas de energía, como la electricidad y el petróleo, el descubrimiento de nuevos metales, como el acero, el aluminio y el cobre, así como por la era de los grandes inventos, como fueron la bombilla, el teléfono, la dinamita y el automóvil. La **Tercera Revolución Industrial** o **Revolución Digital** fue principalmente impulsada gracias al desarrollo de los circuitos integrados (CI) o microchips[5]. Dentro de estos, los microprocesadores y los chips de memoria han posibilitado el desarrollo de sistemas de computación cada vez más potentes que, junto con Internet y las Tecnologías de la información y la comunicación (TIC), han transformado (y lo siguen haciendo) la industria, la sociedad y la economía.

Actualmente estamos metidos de lleno en la llamada **Cuarta Revolución Industrial** o **Industria 4.0**, si bien ya se empieza a hablar de una futura **Industria 5.0**[6][7]. La Industria 4.0, término introducido por primera vez por Henning Kagermann, Wolfgang Wahlster y Wolf-Dieter Lukas en el año 2011 en la *Hannover Messe* (Feria de Hannover)[8], está cambiando radicalmente todos los procesos industriales, desde el planeamiento a la fabricación, la distribución y el mantenimiento.

El cambio que plantea la Industria 4.0 se basa en la adopción de nuevas tecnologías avanzadas para lograr la automatización del proceso productivo. Estas tecnologías combinadas hacen que las fábricas e instalaciones industriales pasen a estar equipadas con sensórica, robótica y software especifico, convirtiéndose así en fábricas inteligentes[9] en la cuales será posible la monitorización y el control de los procesos productivos mediante la recopilación y análisis de datos y la optimización en la toma de decisiones. El *Boston Consulting Group* ha identificado las tecnologías que constituyen los nueve pilares tecnológicos de la Industria 4.0[10][11]:

1. **Big Data y análisis**: El concepto de *Big Data* se aplica a conjuntos de datos de gran tamaño, diversos y complejos, procedentes principalmente de nuevas fuentes de datos. Estos conjuntos de datos, debido a su gran volumen, no pueden ser procesados por el software de procesamiento de datos convencional. En los últimos años el volumen de macrodatos se ha disparado. Los usuarios generan enormes cantidades de datos, pero con la

llegada del Internet de las cosas (IoT) cada vez hay un mayor número de objetos y dispositivos conectados a Internet que generan multitud de datos sobre patrones de uso de los clientes y el rendimiento de los productos. En el contexto de la Industria 4.0, la recopilación y evaluación exhaustiva de datos procedentes de muchas fuentes distintas servirá para apoyar la toma de decisiones en tiempo real.

2. **Robots autónomos**: Los robots se llevan utilizando desde hace mucho tiempo para realizar tareas complejas en entornos industriales. Estos pueden utilizarse en diversos ámbitos, como la producción, la logística y las actividades de distribución, y pueden ser controlados a distancia por humanos. Con la Industria 4.0 cada vez serán más flexibles y autónomos e interactuarán entre sí, trabajarán con seguridad codo con codo con los humanos y aprenderán de ellos.

3. **Simulación**: Los simulacros en entornos virtuales sirven para emular el funcionamiento de máquinas, procesos y personas en tiempo real antes de ponerlos en marcha. Herramientas como la simulación y la realidad virtual se han importado desde el sector videojuegos para integrarse en procesos industriales [12].

4. **Integración horizontal y vertical de sistemas**: La mayoría de los sistemas informáticos actuales no están plenamente integrados. Las empresas, los proveedores y los clientes rara vez están estrechamente integrados, como tampoco lo están departamentos como los de ingeniería, producción y servicios. Con la Industria 4.0, fabricantes, proveedores y clientes estarán estrechamente conectados mediante sistemas informáticos lo que permitirá cadenas de valor verdaderamente automatizadas.

5. **Internet de las cosas**: El IoT consiste en un gran número de dispositivos inteligentes, interconectados a través de medios cableados o inalámbricos, que interactúan y se coordinan para alcanzar un objetivo. El Internet industrial de los objetos (IIoT) forma parte de la evolución general del IoT, pero tiene necesidades particulares que lo diferencian de los demás sistemas y servicios de IoT, como son la necesidad de integrar controladores lógicos programables (PLC) y sistemas de supervisión, control y adquisición de datos (SCADA)[13].

6. **Computación en nube (CC)**: La computación en la nube proporciona una arquitectura flexible en la que los datos y los recursos están descentralizados y son accesibles desde diversos entornos industriales. La computación en la nube ha cambiado la forma de usar, almacenar y compartir datos, servicios y aplicaciones para usos industriales[14].
   Dentro de la computación en nube se pueden distinguir tres tipos: el software como servicio (SaaS), donde el cliente accede a través de internet a un

servicio ofrecido por un proveedor; la plataforma como servicio (PaaS), que permite a los clientes acceder a sus aplicaciones en la nube; y la infraestructura como servicio (IaaS), que ofrece actividades básicas como puede ser el almacenamiento y el procesamiento masivo de datos.

7. **Fabricación aditiva**: La necesidad de producción de piezas y productos altamente personalizados en la Industria 4.0 convierte a la fabricación aditiva en una tecnología clave dada su capacidad para crear objetos complejos con una gran velocidad de producción[15]. La fabricación aditiva consiste en la fabricación de piezas a partir de modelos 3D según diferentes procesos en función de las características del material empleado.

8. **Realidad aumentada (RA)**: La realidad aumentada permite que los operadores se conviertan en operadores 4.0[16][17], facilitando la interacción entre humanos y máquinas, el control remoto en tareas de mantenimiento y la asistencia en las tareas de inspección visual.

9. **Ciberseguridad**: La conectividad de los equipos y dispositivos mediante IIoT suponen nuevas formas de acceso para ataques maliciosos y *malware*. Debido a esto la ciberseguridad cobra especial relevancia en la Industria 4.0.

Todas estas tecnologías pasan a estar conectadas a lo largo de la cadena de valor más allá de una única empresa. Estos sistemas conectados o sistemas ciberfísicos interactúan entre si mediante protocolos web y permiten analizar los datos para predecir fallos y tomar decisiones. La Industria 4.0 permite recopilar y analizar datos entre máquinas, lo que permitirá procesos más rápidos, flexibles y eficientes para producir bienes de mayor calidad a costes reducidos.

La integración digital de la información permite llevar a cabo negocios en un flujo cíclico continuo de información y acciones entre el mundo físico y digital. Este flujo se conoce como *Physical to Digital to Physical* (PDP) y sigue los siguientes pasos:

- **Del ámbito físico al digital**: Mediante sensores y software avanzado se capturan datos del mundo físico y se crea un registro digital.

- **Del ámbito digital al digital**: La información se analiza en sistemas de analítica avanzada e inteligencia artificial, permitiendo generar análisis y predicciones en tiempo real.

- **Del ámbito digital al físico**: Mediante la aplicación de algoritmos se traducen las decisiones del ámbito digital para realizar acciones y cambios en el ámbito físico.

En la Industria 4.0 los costes de mantenimiento se consideran generadores de valor. Esto contrasta con la situación de épocas pasadas cuando se consideraba el mantenimiento como un coste que se debía reducir ya que la tendencia era reparar máquinas o equipos sólo cuando fallaban[3].

1.1.2. Mantenimiento 4.0

La norma española UNE-EN-13306:2018[18] describe el mantenimiento como "la combinación de todas las acciones técnicas, administrativas y de gestión durante el ciclo de vida de un elemento destinadas a conservarlo o restaurarlo a un estado en el que puede realizar la función requerida". Un elemento puede fallar por causas muy diversas como el desgaste (el cual aumenta con el uso), el envejecimiento, el uso indebido o la degradación. En función de si el mantenimiento se realiza antes de que se produzca un fallo o después, se habla respectivamente de mantenimiento preventivo o de mantenimiento correctivo.

El mantenimiento correctivo es aquel que se aplica cuando debido a una avería es necesaria la sustitución de un elemento para que los equipos o maquinaria vuelvan a funcionar correctamente. A su vez se divide en mantenimiento correctivo inmediato, cuando no se puede posponer debido a consecuencias inaceptables, y mantenimiento correctivo diferido, cuando se puede retrasar su ejecución según una serie de reglas dadas. Este tipo de mantenimiento puede a llegar a ser muy crítico, según el grado de afectación de la falla, debido al coste de sustitución del elemento dañado y al tiempo que la instalación deba permanecer inactiva.

El mantenimiento preventivo está orientado a evitar o minimizar en lo posible la probabilidad de fallo de un elemento. Incluso en el caso de tener que realizar paradas por reparaciones, el mantenimiento predictivo permite realizarlas de forma planificada reduciendo de esta forma los costes asociados. Dentro del mantenimiento predictivo tenemos el mantenimiento predeterminado, el cual consiste en tareas de inspección realizadas regularmente según criterios técnicos cuyo objetivo es reducir la probabilidad de fallos en los equipos y asegurar el correcto funcionamiento de los mismos. Por otra parte, también tenemos el mantenimiento predictivo basado en la condición, en el cual se realiza un análisis de la condición de un elemento mediante su observación directa por parte de un operador, su monitorización o la realización de diferentes pruebas en función de su naturaleza. Según el resultado de la inspección y análisis del elemento se procede a realizar las acciones de mantenimiento en caso de ser necesarias.

El mantenimiento predictivo es el centro de mantenimiento 4.0. Es un tipo de mantenimiento basado en la condición en el que el uso combinado de las tecnologías citadas en la industria 4.0 permiten la monitorización continua de un elemento y el análisis automático de los datos capturados para anticipar la detección de equipamientos afectados y así reducir el tiempo de inactividad no programado y mejorar la productividad. La combinación de datos históricos con los datos recopilados en tiempo real permite evaluar la evolución de la degradación de un elemento y anticipar un mantenimiento predictivo activo.

1.1.3.   Monitorización y control en mantenimiento

La monitorización industrial es el proceso de control en tiempo real de los sistemas de una planta o instalación industrial con el objetivo de garantizar que estén funcionando de forma correcta. Las tareas de monitorización incluyen la recopilación de datos en tiempo real, como temperatura, presión, vibraciones o humedad, entre otros, y el análisis de parámetros que indiquen posibles fallos. Esto permite anticipar las actuaciones de mantenimiento necesarias en cualquier elemento de la instalación.

La monitorización incluye diferentes técnicas como el análisis de vibraciones, los ultrasonidos, el análisis del lubricante, el análisis de partículas de desgaste, la termografía y la visión computacional. El uso de la visión computacional entra dentro de la inspección visual automatizada que es la técnica desarrollada en esta tesis doctoral.

La inspección visual es un método de control no destructivo, ampliamente usado en industria, basado en la observación de un elemento con el fin de detectar defectos visibles, tales como grietas, abolladuras, defectos de soldaduras, corrosión o deformaciones. La inspección visual directa consiste en la observación de un elemento por parte del inspector a simple vista o con la ayuda de lentes de aumento, microscopios, iluminación auxiliar, reglas, calibres, etc. Por otra parte, la inspección visual remota permite la observación de elementos que, por temas de inaccesibilidad o peligrosidad, no permiten la observación directa. Es el caso del uso de baroscopios flexibles, videoscopios y fibroscopios para acceder al interior de ciertos elementos o el uso de drones, cámaras fijas o plataformas robóticas. En ciertos casos, esta técnica permite a los inspectores realizar inspecciones visuales en lugares de difícil acceso, en ambientes peligrosos o en ubicaciones geográficamente remotas, sin estar físicamente presentes en la ubicación del elemento a inspeccionar.

A parte de la división entre inspección visual directa y remota se puede clasificar la inspección visual en simple, asistida y automatizada. La inspección visual simple es una técnica de control en mantenimiento que se realiza a simple vista sin emplear ninguna herramienta o instrumento auxiliar. La inspección visual asistida emplea herramientas para mejorar la visualización de defectos difíciles de detectar con la inspección visual simple, como lupas, microscopios, cámaras e iluminación especial. Estas tareas de inspección dependen de la formación del inspector y de su habilidad y suponen un gran coste de mano de obra, desplazamientos, formación, etc. La inspección visual automatizada, mediante el uso de cámaras y algoritmos de visión computacional, permite el análisis automático de las imágenes y la detección de defectos difíciles de detectar con la inspección visual simple o la inspección visual asistida. Este tipo de inspección automatizada presenta la ventaja de ser más rápida y precisa que las que dependen de un inspector, reduciendo los costes asociados.

1.2. Geotecnologías

Debido al rápido desarrollo de nuevas tecnologías que se han ido incorporando a los campos de la captura, procesamiento y análisis de información geoespacial, en las últimas décadas han ido apareciendo una serie de términos que muchas veces se tratan como sinónimos. Los términos más populares son geomática, geoinformática (principalmente usado en Europa), tecnología geoespacial (usado en EEUU) y geotecnología (España y América Latina).

El origen del término geomática se remonta al año 1969 cuando Bernard Dubuisson sugirió combinar el prefijo "geo" (en referencia a la Tierra) con "matique" (de la palabra francesa "informatique") [19]. En 1990 Gagnon y Coleman se refirieron a la geomática en estos términos: "La geomática abarca una amplia gama de disciplinas que se pueden unir para crear una imagen detallada pero comprensible del mundo físico y nuestro lugar en él. Estas disciplinas incluyen la topografía, la cartografía, la teledetección, los sistemas de información geográfica (SIG) y el sistema de posicionamiento global (GPS)"[20]. Actualmente el termino geomática está recogido por la norma ISO/TC211/WG1 N119 donde se define como la "disciplina relacionada con la recopilación, distribución, almacenamiento, análisis, procesamiento, presentación de datos geográficos o información geográfica".

El término geoinformática fue introducido inicialmente por el sueco Samuelson en 1988. Posteriormente, en 1993, el alemán Manfred Ehlers definió la geoinformática como el "arte, ciencia o tecnología que se ocupa de la adquisición, almacenamiento, procesamiento, producción, presentación y difusión de geoinformación"[22].

Dado que las definiciones de geomática y geoinformática utilizan prácticamente los mismos términos (adquisición, almacenamiento, procesamiento, difusión) Artur Krawczyk ha tratado de definir de forma más clara ambos términos:

La geomática es el conocimiento y la capacidad de usar sistemas de información para integrar datos sobre objetos espaciales y fenómenos espacio-temporales relacionados con la superficie de la Tierra, con el fin de realizar análisis espaciales, pronosticar y visualizar su estado y cambios[23].

La geoinformática es la programación de aplicaciones, estructuras de datos espaciales y análisis de objetos y fenómenos espacio-temporales referidos a la superficie terrestre, junto con el diseño, desarrollo y mantenimiento del software y servicios web destinados al modelado y análisis de los datos espaciales[23].

Por otra parte, el término geotecnologías (originado a partir de la combinación de "tecnología geoespacial") abarca multitud de herramientas y técnicas usadas en

el campo del procesamiento de datos espaciales tanto por la geomática como por la geoinformática.

A continuación se hace una breve descripción de las geotecnologías empleadas en la presente tesis doctoral.

Fotogrametría

La fotogrametría es la ciencia y técnica que permite obtener la forma y dimensiones de los objetos mediante el empleo de fotografías. Actualmente, gracias a los avances en visión computacional, la reconstrucción tridimensional precisa de un objeto es un proceso muy automatizado. La técnica SfM (*Structure from Motion*) garantiza una gran robustez al apoyarse en la detección automática de puntos homólogos, el *matching* robusto de los mismos y la orientación y autocalibración mediante un ajuste de haces. Por otra parte, la técnica MVS (*MutiView Stereo*) permite la generación de modelos de nubes de puntos densos.

La flexibilidad de la fotogrametría permite trabajar a muy diferentes escalas y precisiones. La fotogrametría de rango cercano permite obtener precisiones submilimétricas (como por ejemplo la fotogrametría industrial) o centimétricas (arquitectura, patrimonio). En el lado contrario esta la fotogrametría aérea tradicional en la cual es posible abarcar grandes extensiones de terreno.

Gracias a su robustez y precisión, así como a la facilidad para adaptarse a diferentes escalas y escenarios, la fotogrametría es una de las técnicas más usadas para la reconstrucción tridimensional, compitiendo en muchos casos con el LiDAR (*Light Detection and Ranging*) o los escáneres láser terrestres, siendo comparativamente una técnica de bajo coste.

Si bien la fotogrametría basada en SfM garantiza gran precisión en la reconstrucción de escenas tridimensionales, el modelo generado carece de orientación y escala. Además, dependiendo del patrón de vuelo, la calibración automática puede no eliminar toda la distorsión de los productos resultantes dando lugar al efecto *Bowling*[24]. Este efecto se puede mitigar tomando ciertas precauciones al planificar el vuelo[25], usando puntos de control en el terreno o empleando las técnicas de posicionamiento preciso RTK (*Real Time Kinematic*) o PPK (*Post Processed Kinematic*).

Tradicionalmente el uso de puntos de control era algo fundamental para garantizar productos precisos, al incluirlos en el ajuste de haces del modelo. En la actualidad, si bien se siguen empleando los puntos de control con frecuencia, han aparecido dos tecnologías que han demostrado ser igualmente precisas[26], ya que el uso de PPK o RTK garantiza la precisión centimétrica de las posiciones de las cámaras. Esto permite realizar una georreferenciación de los modelos obtenidos por fotogrametría, ya sea mediante una transformación rígida[27] o incluyendo las posiciones de las cámaras en el ajuste de haces.

En cuanto a la operativa, la diferencia entre RTK y PPK reside en que el primero trabaja en tiempo real mientras que el segundo lo hace en postproceso.

En RTK tanto el dron como la base reciben lecturas de las diferentes constelaciones de satélites disponibles, siendo además necesario un enlace constante entre ambos que proporcione las correcciones en tiempo real. En el caso de PPK no existe el enlace entre la base y el dron y las correcciones se aplican en postproceso con los datos de la base y el dron.

Teledetección

La teledetección es la técnica de adquisición remota de datos de La Tierra u otros planetas mediante sensores instalados en satélites y aeronaves, que detectan y registran la energía reflejada o emitida. En función de los sensores empleados se puede hablar de teledetección activa o pasiva. Los sensores pasivos miden la intensidad de la radiación electromagnética reflejada o emitida en ciertas bandas del espectro electromagnético, generalmente visible, infrarroja, infrarroja térmica y de microondas. Estos sensores miden la temperatura de la superficie terrestre y marina (banda infrarroja térmica), las propiedades de la vegetación (bandas visible e infrarroja), las propiedades de las nubes y los aerosoles (ultravioleta), y otros atributos físicos. Por otra parte, los sensores activos emiten una señal hacia el objeto y miden la radiación retornada. Ejemplos de este tipo son el Radar (*radio detection and ranging*) y el LiDAR.

En 1972 la National Aeronautics and Space Administration (NASA) y el United States Geological Survey (USGS) lanzaron el programa Landsat, desplegando el primer satélite de observación de la tierra. Sin embargo, la democratización de la teledetección llegó en el año 2008 con la publicación de los datos Landsat bajo licencia libre y abierta. En el ámbito europeo, la Comisión Europea y la Agencia Espacial Europea (ESA) lanzaron en 2014 el satélite Sentinel 1A dentro del programa Copernicus[28].

Hasta la fecha 9 satélites han formado parte de la misión Landsat, siendo Lansat-9 el último en ser lanzado el 27 de septiembre de 2021. Actualmente están en funcionamiento Landsat-8 y Landsat-9 con unas características muy similares y un periodo de revisita de 16 días.

La misión Sentinel-2 sirve de apoyo a diversos servicios y aplicaciones ofrecidos por Copernicus, como la gestión del territorio, la agricultura, el control de catástrofes, las operaciones de ayuda humanitaria y la cartografía de riesgos. Está constituida por dos satélites gemelos en la misma orbita, pero en fase de 180º para permitir un periodo de revisita de 5 días.

Además de los satélites pertenecientes a los diferentes programas de observación terrestre de las agencias espaciales también hay satélites comerciales que destacan por la gran resolución espacial de sus productos. Entre los satélites comerciales se pueden citar GeoEye, WorldView, Spot, QuickBird, RapidEye y Pleiades.

Escáner láser 3D

Un escáner láser o escáner láser 3D es un sensor activo que mediante la emisión de un pulso láser y la medición de la señal devuelta permite obtener la distancia

a un punto del objeto escaneado. A su vez, el pulso láser es dirigido mediante un espejo para barrer la escena en una dirección, mientras que en la otra dirección el barrido se realiza mediante el desplazamiento o el giro del sensor.

En cuanto al principio de medición, los más empleados en aplicaciones geomáticas son los escáneres de tiempo de vuelo y los de diferencia de fase. Los primeros se basan en la medición del tiempo entre la emisión del haz láser y su retorno tras reflejarse en el objeto escaneado. Estos escáneres tienen la ventaja de permitir distancias más grandes. Los escáneres de diferencia de fase se basan en la emisión de una serie de pulsos láser de diferente longitud de onda, que son comparadas con las reflejadas por el objeto. Este tipo de escáneres presentan la ventaja de permitir una mayor precisión en la medición y en la cantidad de puntos registrados.

En función de método de captura de datos podemos distinguir entre escáneres estáticos, cuando el escáner se sitúa sobre una base fija y realiza el barrido de la escena, y móviles, cuando el escáner se desplaza por la escena ya sea embarcado en un dron, un vehículo o transportado por un operador. Dentro de los primeros se encuentran los escáneres láser terrestres (TLS) que se caracterizan por su precisión, rapidez y la densidad de puntos capturados. Los primeros escáneres móviles dependían para posicionarse de un sistema global de navegación por satélite (*Global Navigation Satellite System* - GNSS) y una unidad de medición inercial (*Inertial Measurement Unit* - IMU) lo que restringía su uso a exteriores y generalmente se limitaba a sistemas montados en vehículos. Las mejoras en la metodología *Simultaneous Location And Mapping* (SLAM) han permitido el escaneo móvil de escenarios tanto exteriores como interiores con sistemas portátiles o con sistemas montados en plataformas móviles [29].

Infraestructura de datos espaciales (IDE)

Una IDE es una combinación de tecnologías, normativas y estándares abiertos que permiten organizar, publicar y acceder a información geoespacial a través de internet.

El *Open Geospatial Consortium* (OGC) define una serie de estándares que permiten la interoperabilidad de la información geoespacial, es decir servir y/o consumir tanto mapas ráster como vectoriales, acceder a la información almacenada en las bases de datos, consultar un catálogo de servicios, trabajar con formatos estándar, etc. En concreto los estándares más usados son:

- **Web Map Service (WMS)** [30]: Proporciona una interfaz HTTP (*Hypertext Transfer Protocol*) para solicitar imágenes cartográficas georreferenciadas. El origen de los datos puede ser vectorial, ráster o una base de datos geoespacial.

- **Web Feature Service (WFS)** [31]: Define una interfaz HTTP para la consulta y edición de entidades geográficas.

- ***Web Coverage Service*** **(WCS)**: Interfaz HTTP que permite el acceso a coberturas geoespaciales, como pueden ser modelos digitales del terreno (MDT), Radar, datos atmosféricos, etc.

- ***Geography Markup Language*** **(GML)** [32]: Gramática XML para expresar características geográficas. GML sirve como lenguaje de modelado para sistemas geográficos y como formato de intercambio abierto para transacciones geográficas en Internet.

- ***Keyhole Markup Language*** **(KML)**: Formato XML orientado a la visualización geográfica, que incluye anotaciones de mapas e imágenes.

1.2.1. Geotecnologías en la industria

El uso de las geotecnologías en la industria posibilita una mejor gestión y planificación al proporcionar herramientas que permiten la monitorización y el registro de información de diversas variables dentro de un entorno industrial. Además, permite el procesamiento, análisis y visualización de los datos geoespaciales resultantes, lo cual capacita a las empresas para tomar decisiones de manera más efectiva.

La aplicación de las geotecnologías en industria puede llegar a abarcar todo el ciclo de vida de una instalación industrial, desde el planeamiento a la rehabilitación final del entorno (una vez acabada la vida útil de la instalación), pasando por las tareas de construcción, inspección y mantenimiento.

En el planeamiento y construcción de cualquier instalación industrial el uso de las geotecnologías es indispensable. La elección de la ubicación de una instalación industrial tiene que cumplir una serie de requisitos técnicos, medioambiental, geológicos y geográficos. Los sistemas de información geográfica (SIG) permiten realizar un análisis geográfico con todos estos requisitos permitiendo obtener las zonas idóneas para el emplazamiento. Los MDT, obtenidos por fotogrametría o Li-DAR, y las ortofotografías son productos ampliamente usados en el planeamiento y ejecución de obras.

La fotogrametría es una técnica muy usada en industria gracias a la flexibilidad para adaptarse a diferentes escalas y entornos. Con la fotogrametría de rango cercano es posible alcanzar unas grandes precisiones y por tanto se usa en numerosos campos de la industria como la fabricación de automóviles, en industrias aeronáuticas o en ingeniería naval[33]. El uso de fotogrametría con drones se lleva usando con éxito desde hace unos pocos años en diversas tareas de inspección en instalaciones y entornos industriales como líneas eléctricas[34], industria petrolera y gasística[35] y en minería[36][37]. El uso de drones equipados con una cámara termográfica se viene aplicando en la detección de patologías en paneles fotovoltaicos[38][39]. Otra de las grandes ventajas de los drones es que constituyen una solución segura y fiable para inspeccionar zonas de difícil acceso o peligrosas.

En el control de flotas la geolocalización ha sido desde el inicio el componente fundamental para permitir el seguimiento de flotas de vehículos y barcos[40]. Hoy en día han entrado en juego nuevas tecnologías, como las cadenas de bloques, el *Big Data* y el procesamiento en la nube, que han posibilitado que el control de flotas sirva también para tareas de planificación. Aquí entran en juego los SIG y las IDE que permiten el cálculo de rutas óptimas y la gestión de incidencias en tiempo real.

Uno de los mayores avances en los últimos años está siendo la navegación autónoma de vehículos. A parte de la visión computacional basada en análisis de imágenes, las tecnologías empleadas para el guiado de vehículos incluyen GNSS, LiDAR, Radar e IMU[41][42].

Cuando una instalación industrial, mina o cantera llega al fin de su vida útil se debe proceder a la rehabilitación del entorno. En este caso se han venido empleado varias geotecnologías como la fotogrametría[43], la teledetección[44][45] y el LiDAR[46].

1.3. Hipótesis de trabajo

Anteriormente se ha visto como el uso de la geomática nos provee de una serie de geotecnologías que permiten trabajar en multitud de escenarios, tanto dentro de edificios como en exteriores, a diferentes escalas y precisiones o en entornos de difícil acceso. A su vez, la geoinformática permite el desarrollo de software específico que facilite el análisis e interpretación de los datos capturados, la automatización de tareas de descarga de información y el procesamiento de datos para la generación de productos derivados, así como de facilitar la toma de decisiones en las tareas de inspección.

La línea de investigación seguida en esta tesis doctoral parte del supuesto de que el uso de geotecnologías puede ser adecuado para la mejora de los procesos de inspección y monitorización en entornos industriales. De esta forma se establecen las siguientes hipótesis de trabajo:

- La fotogrametría de rango cercano es un método no invasivo y de bajo coste que se puede emplear para la generación de modelos 3D que sirvan en la inspección de soldaduras.

- Se pueden desarrollar algoritmos basados en visión computacional para analizar la geometría y características de uniones soldadas a partir de imágenes.

- Se puede utilizar la teledetección para el mantenimiento de entornos industriales a gran escala como los parques fotovoltaicos.

- El uso de imágenes satelitales libres permite un ahorro de costes en la inspección de entornos industriales en exteriores.

- El uso de un sistema de escaneado portátil puede sustituir a un escáner láser terrestre en tareas de inspección de inspección en instalaciones fluidomecánicas.

- El uso de librerías de código abierto permite un desarrollo más rápido de las herramientas software.

- La centralización del procesamiento de los datos y almacenamiento de la información en la nube permite una optimización de recursos.

- El uso de los estándares OGC garantizan el consumo de la información generada como servicios WMS y WFS desde cualquier SIG o IDE.

- El uso de cámaras termográficas permite la detección de puntos calientes en paneles fotovoltaicos.

- Las técnicas de visión computacional permiten la segmentación automática de los paneles de una planta fotovoltaica.

- La fotogrametría con drones apoyada en PPK/RTK garantiza la georreferenciación precisa de los paneles fotovoltaicos y los puntos calientes detectados.

1.4. Objetivos

El objetivo principal de la presente tesis doctoral es el estudio y desarrollo de geotecnologías orientadas a la automatización en la inspección y mantenimiento en entornos industriales de distinta índole y diferentes escalas.

A continuación, se enumeran los objetivos específicos:

- Creación de una herramienta que permita a los inspectores realizar el control de calidad externo de las soldaduras de forma sencilla y eficiente sin necesidad de inspecciones visuales ni herramientas externas, y evitando así la subjetividad e imprecisión del protocolo clásico.

- Validar la usabilidad de un sistema de escaneado portátil para la optimización en la toma de datos en las tareas de inspección en instalaciones fluidomecánicas.

- Desarrollo de una herramienta software para la detección automática del tipo de patología conocido como punto caliente en paneles fotovoltaicos, partiendo de imágenes de cámaras RGB y termográficas capturadas con drones, garantizando productos cartográficos de alta calidad y la geolocalización precisa de las patologías.

- Desarrollar una IDE para la automatización y monitorización de las tareas de detección de vegetación inusual y cuerpos de agua en las cercanías de plantas fotovoltaicas.

1.5. Estructura de la tesis

La presente tesis doctoral se presenta por la modalidad de compendio de artículos científicos siguiendo la normativa específica de la Universidad de Salamanca que regula las enseñanzas oficiales de doctorado[47]. Se incluyen cuatro artículos científicos publicados en revistas internacionales de impacto JCR (*Journal Citation Reports*).

El documento de la tesis se estructura en un total de seis capítulos y dos apéndices según se detallan a continuación.

Capitulo 1. Introducción

El capítulo introductorio proporciona un primer acercamiento a las tareas de mantenimiento e inspección de entornos industriales y a las problemáticas detectadas en las mismas. A continuación, se hace una descripción de la geomática y las geotecnologías como herramientas que pueden ser usadas para la automatización de las tareas de mantenimiento en instalaciones industriales. Por último, se establecen las hipótesis de trabajo y los objetivos de la tesis doctoral.

Capítulo 2. Automatización en la inspección de soldaduras con fotogrametría de rango cercano

En este capítulo se ha abordado el desarrollo de una herramienta que facilite a los inspectores la realización del control de calidad externo de las soldaduras sin necesidad de inspecciones visuales ni herramientas externas. Este desarrollo fue publicado en forma de artículo científico bajo el título *"WELDMAP: A Photogrammetric Suite Applied to the Inspection of Welds"*.

Capítulo 3. Validación de sistema de escaneado portátil para tareas de inspección

El presente capítulo se centra en la validación de un sistema de escaneado portátil para tareas de inspección en instalaciones fluidomecánicas. Para su validación se empleó como verdad terreno los resultados obtenidos con un TLS.

En este capítulo se incluye el artículo *"Validation of Portable Mobile Mapping System for Inspection Tasks in Thermal and Fluid–Mechanical Facilities"*.

Capítulo 4. Mantenimiento de plantas fotovoltaicas mediante fotogrametría

En el cuarto capítulo se aborda el desarrollo de una aplicación para la detección de patologías en plantas fotovoltaicas, empleando drones y una combinación de imágenes visibles y térmicas.

En este capítulo se incluye el artículo *"SunMap: Towards Unattended Maintenance of Photovoltaic Plants Using Drone Photogrammetry"*.

Capítulo 5. Mantenimiento de plantas fotovoltaicas con teledetección

En este artículo se describe el desarrollo de la IDE INSPECTORMAP cuyo objetivo es servir como herramienta para la monitorización de vegetación inusual y cuerpos de agua en las cercanías de plantas fotovoltaicas.

El desarrollo de la IDE INSPECTORMAP se recoge en la publicación *"INSPECTORMAP: A Spatial Data Infrastructure Applied to the Maintenance of Solar Plants Using Free Satellite Imagery"*.

Capítulo 6. Conclusiones

Este capítulo contiene la discusión técnica de los resultados y conclusiones alcanzados a lo largo del desarrollo de esta tesis doctoral. A su vez, se establecen las posibles líneas de trabajo futuras que pueden surgir a partir de los trabajos desarrollados.

Apéndice A. Indexación y factor de impacto de las publicaciones

Este primer apéndice proporciona información acerca de diferentes métricas de evaluación de impacto y relevancia, como el factor de impacto (FI), de las revistas científicas en las cuales se han publicado los artículos que conforman la presente tesis doctoral.

Apéndice B. Software

Este segundo apéndice presenta el software desarrollado durante la elaboración de la tesis doctoral.

Capítulo 2

Automatización en la inspección de soldaduras con fotogrametría de rango cercano

Capítulo 2

Automatización en la inspección de soldaduras con fotogrametría de rango cercano

En este capítulo se incluye el artículo *"WELDMAP: A Photogrammetric Suite Applied to the Inspection of Welds"* publicado en la revista *Applied Sciences* en febrero de 2022.

2.1. Resumen

La soldadura es un componente clave en los campos de la ingeniería y la construcción, ya que cualquier defecto en una soldadura puede afectar significativamente a las propiedades mecánicas de las juntas, lo que puede provocar la disminución de la vida útil de la estructura o incluso su colapso. Para evaluar el cordón de soldadura y detectar posibles imperfecciones y fallas superficiales, es fundamental llevar a cabo tareas de inspección y seguimiento de acuerdo con los requisitos establecidos en las normativas. No obstante, la inspección visual depende de factores subjetivos, como la habilidad del inspector, ya que tradicionalmente la inspección se realiza a simple vista o con la asistencia de herramientas de uso manual. Según los problemas observados en la inspección manual, el primer objetivo abordado en el desarrollo de esta tesis fue dotar a los inspectores de una herramienta de inspección visual automatizada, eficiente y sencilla, que permitiese realizar el control de calidad externo de las soldaduras de forma sencilla y eficiente, evitando así la subjetividad e imprecisiones del protocolo clásico.

La fotogrametría de rango cercano es una técnica no invasiva que permite la reconstrucción tridimensional de los cordones de soldadura y garantiza la precisión suficiente para realizar mediciones de defectologías según los requisitos de los estándares internacionales. La integración del proceso fotogramétrico con al-

goritmos para la automatización de los análisis de defectología han dado lugar al *software* WELDMAP cuya descripción se recoge en el apéndice B.4.

Los defectos objeto de estudio fueron el exceso de metal de soldadura, desalineamiento lineal, desalineamiento angular y porosidad. Estos defectos se analizaron mediante el estudio de secciones transversales a lo largo de la soldadura, tomando como referencia el eje del cordón y siguiendo los límites establecidos en la normativa internacional. El primer paso es la clasificación automática de la nube de puntos para distinguir entre la placa izquierda, la placa derecha y el cordón. Una vez extraídos estos elementos se generan automáticamente las secciones transversales, cuyo análisis permite identificar fallas e imperfecciones de acuerdo con los cuatro defectos previamente definidos.

Para la validación del flujo de trabajo de WELMAP se generó un conjunto de datos de diferentes tipologías de soldaduras, adquiridas tanto en escenarios reales como en laboratorio utilizando muestras específicas. La resolución y la precisión logradas por la fotogrametría mejoraron sustancialmente en comparación con las obtenidas por los métodos utilizados actualmente, basados en la inspección visual de las soldaduras utilizando dispositivos manuales.

Article

WELDMAP: A Photogrammetric Suite Applied to the Inspection of Welds

Esteban Ruiz de Oña [1], Manuel Rodríguez-Martin [2], Pablo Rodríguez-Gonzálvez [3], Rocio Mora [1] and Diego González-Aguilera [1,*]

1 Department of Cartographic and Land Engineering, Higher Polytechnic School of Ávila, Universidad de Salamanca, Hornos Caleros 50, 05003 Ávila, Spain; estebanrdo@usal.es (E.R.d.O.); rociomora@usal.es (R.M.)
2 Department of Mechanical Engineering, Higher Polytechnic School of Zamora, Campus Viriato, Universidad de Salamanca, Avenida Requejo 33, 49022 Zamora, Spain; ingmanuel@usal.es
3 Department of Mining Technology, Topography and Structures, Universidad de León, Av. Astorga s/n, 24401 Ponferrada, Spain; p.rodriguez@unileon.es
* Correspondence: daguilera@usal.es; Tel.: +34-920-353-500 (ext. 3820)

Abstract: This paper presents a new tool for external quality control in welds using close-range photogrammetry. The main contribution of the developed approach is the automatic assessment of welds based on 3D photogrammetric models, enabling objective and accurate analyses through an in-house tool that was developed, WELDMAP. As a result, inspectors can perform external quality control of welds in a simple and efficient way without requiring visual inspections or external tools, and thus avoiding the subjectivity and imprecisions of the classical protocol. The tool was validated with a large dataset in laboratory tests as well as in real scenarios.

Keywords: welding; photogrammetry; non-destructive tests (NDT); quality control; software development

1. Introduction

Welding is a very important task in the field of engineering and construction, since welds that are not properly carried out reduce the mechanical properties of joints, minimising their effective service life, and possibly promoting their collapse, which could entail drastic consequences, being that welding joints are the weakest links in assemblies [1]. For this reason, quality requirements are highly standardised (e.g., [2–4] and also highly specified for specific cases such as pressure vessels [5]).

Therefore, welding is a joining process that requires inspection and monitoring tasks. The visual inspection is a simple and widely extended non-destructive test modality [6], which is applied for the assessment of weld bead geometry and the detection of surface imperfections and flaws. Visual inspection tests are regulated by the standard [7].

The application of visual inspection allows for detecting defects and imperfections that have a manifestation on the surface of the weld. The taxonomy of defectology in welds is widely established by the international quality standards (e.g., [3,4]). So, inspection techniques are aimed at detecting and evaluating defects established in these norms. Visual inspection, as a non-destructive testing method, should be implemented by inspectors with training and expertise who have acquired a level of competence also established by the international standards (e.g., [8]). These inspectors are often engineers with extensive knowledge of the welding process and who have passed several exams to demonstrate that they have the right skills.

The inspector usually has the obligation to visit the welds on-site to evaluate the quality of each weld performed according to the international standards, which entails a significant economic investment [6]. In addition, the inspector must evaluate the weld at the site, often in a very short time and record the information of each weld in an analogical

way or in traditional databases. To do this, it is common to use different auxiliary tools to evaluate the quality of welds such as tweezers or weld gadget kits [9]. These tools, being for manual use, generate measures with significant errors and especially result in visual fatigue for the inspector.

Currently, some authors are investigating other, more sophisticated techniques for the detection and identification of external pathologies in welds: laser systems [10,11], scanning cameras [12], hybrid laser-based systems and cameras [13–16], stereo imagery [12,17], close-range photogrammetry [9,18], and, finally, active thermography systems as supports for visual inspection, which are applied directly to the study of cracks in welds [19].

Among these techniques, close-range photogrammetry and laser scanning allow the accurate three-dimensional reconstruction of weld bead geometries in a non-invasive way. Such 3D models can be used for the inspection of external welding imperfections and defects. However, there are several differences in terms of operating principle (i.e., active versus passive sensors), working range, and cost-efficiency ratio. The reader can find more information about this comparison in [20,21]. Close-range photogrammetry has been used for the generation of 3D models that allow for the analysis of defects such as overlap and lack of fusion, among others [9]. It has also been used for the three-dimensional assessment of plaque misalignment [22]. In [9], a pioneering method of inspection based on close-range photogrammetry was established. For its part, active systems such as laser scanning have been also used for the evaluation of the external quality of welds. In [22], authors used a structured light system, which allows the accurate assessment of the weld bead according to the quality criteria. The procedure developed enables the extraction of metric information about the thickness and the deformation angle of the welds. However, to date, there is not a global solution that integrates the 3D reconstruction of welds with the automatic assessment of their external quality according to international standards.

Therefore, this paper presents a software, WELDMAP, which allows systematising the external assessment of welds based on close-range photogrammetry, integrating algorithms to implement defectology analysis in an appropriate manner in accordance with the quality standards.

After this introduction, the document has been structured as follows: Section 2 describes the methodology, highlighting the key steps for the 3D welds' reconstruction and their defectology analysis. The experimental results are listed and discussed in Section 3. Finally, Section 4 is devoted to outlining the main conclusions and future perspectives.

2. Methods

Currently available commercial products devoted to the quality control of welds bypass the use of robust and accurate 3D models and are more focused on the assessment of internal defectology using consolidated non-destructive techniques (e.g., X-ray, ultrasounds, etc.). Considering this limitation, an in-house software, named WELDMAP, has been developed with the aim of providing a robust tool for the external inspection of welds. Based on the advantages offered by computer vision (low-cost and flexibility) and photogrammetry (accuracy and reliability), together with the different algorithms specifically developed for quality control, the information for the inspection of welds can be computed, analysed, and monitored in an efficient way. As a result, objective and accurate expert reports can be generated by the inspectors. Figure 1 outlines the main workflow codified in the software WELDMAP. The following sections will explain this software's methodology.
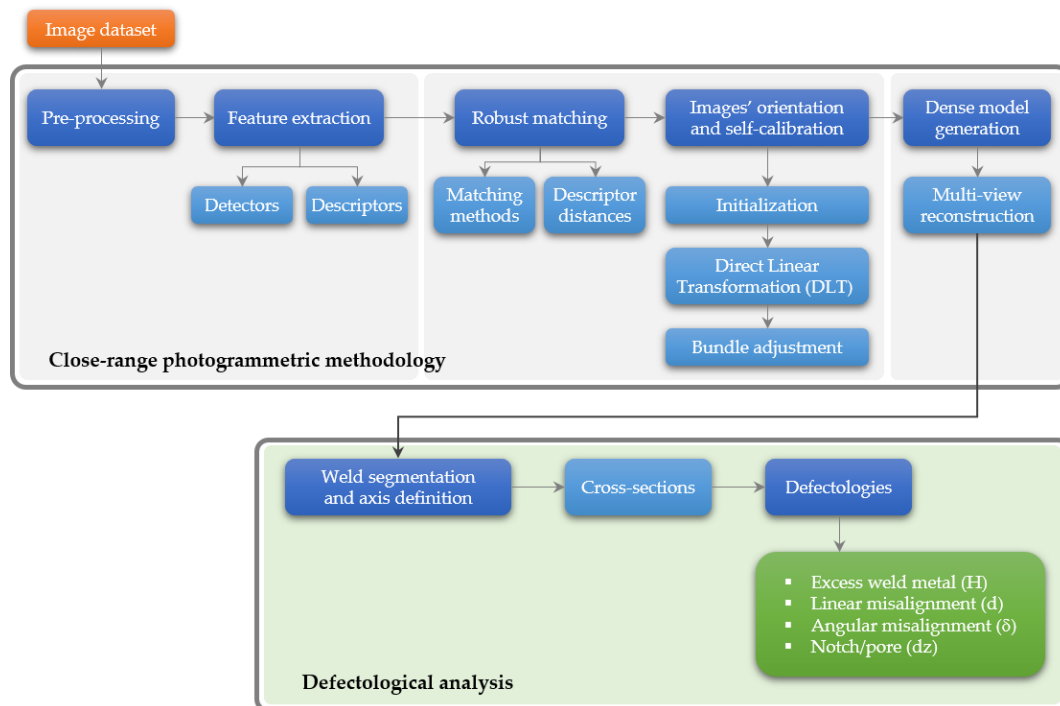
Figure 1. WELDMAP: structure and modules organisation.

2.1. Close-Range Photogrammetric Methodology

The photogrammetric pipeline is a process oriented to obtain a dense and three-dimensional point cloud of a weld's surface through the application of different algorithms and phases, which will be detailed in the following subsections.

Extraction and Matching of Features

Since image acquisitions were not only limited to vertical but also an oblique point of view, the processing of the images must incorporate last advances and algorithms in computer vision for images matching [23] and images orientation [24,25]. Before extracting and matching features, images must be pre-processed in order to improve the radiometric contents and ease the successive feature extraction. Image pre-processing has been reported in many papers as a fundamental step, particularly in those cases where the texture quality is non-favourable [26–28]. Different pre-processing algorithms are available in WELDMAP, including, among others: ACEBSF [29], POHE [30], RSWHE [31], Wallis [32], etc. This step is facultative but highly suggested in order to achieve better results in the feature extraction and matching step.

WELDMAP implements diverse sets of detectors (e.g., SIFT [33], SURF [34], MSER [35], MSD [36], ORB [37], AKAZE [38], BRISK [39], etc.) and descriptors (e.g., BOOST [40], BRIEF [41], DAISY [42], FREAK [43], etc.) to let the user run and test different combinations and assess the results in different conditions. Any kind of combination is allowed in the software. For each detector–descriptor, several advance parameters can be defined by the user.

Finally, the features extracted are matched robustly using geometric constraints in order to guarantee that they match the same point. To this end, WELDMAP uses projective geometry and more precisely homography, based on epipolar geometry, to refine the matching. Considering this, cameras could be uncalibrated and the possible presence of outliers in the matching, fundamental matrix, and RANSAC [44] are used to verify the matchings from a geometrical point of view.

2.2. Orientation and Dense Model Generation

2.2.1. Images' Orientation and Self-Calibration

The cameras' orientation and self-calibration were performed hierarchically in three steps following the pipeline of Figure 1:

- First, the initialisation of the first image pair was carried out, selecting the best pair of images. To this end, a trifold criterion was established for selecting the initial image pair: (i) guarantee a good ray intersection; (ii) contain a considerable number of matching points; (iii) present a good matching points distribution along the image format. Note that initialising with a good image pair usually results in a more reliable and accurate reconstruction.
- Second, once the image pair was initialised, image triangulation was performed through the direct linear transformation (DLT) [45], taking the matching points and the camera pose provided by the fundamental matrix as input data. Afterwards, and considering this initial image pair as a reference, new images were firstly registered and then triangulated using again the DLT. The DLT allows us to estimate first the camera pose and then to triangulate matching points in a direct way, that is, without initial approximations and without calibration camera parameters. As a result, 2D–3D correspondences are provided together with the registration of the images.
- Third, although all the images were registered and triangulated based on DLT, this method suffers from limited accuracy and reliability, which could drift quickly to a non-convergent state. To cope with this problem, a bundle adjustment (BA) based on a collinearity condition [24] was applied with a threefold purpose: (i) compute registration and triangulation together and in a global way; (ii) consider the estimation of the inner parameters of the camera, self-calibration; (iii) obtain more accuracy and precision in the image orientation and self-calibration, using a non-linear iterative procedure supported by the collinearity condition that minimises the reprojection error.

As a result of this orientation and self-calibration stage, an integrated registration and triangulation are obtained which entails that all images are connected and related according to the camera pose (rotation matrix and translation vector), without forgetting the inner parameters of the camera (self-calibration).

2.2.2. Dense Model Generation

Once we had solved the orientation and self-calibration of the imagery dataset, a multi-view reconstruction approach [46] that combines stereo and shape-from-shading energies into a single optimisation scheme was used. Particularly, this method uses image gradients to transition between stereo-matching (which is more accurate at large gradients) and Lambertian shape-from-shading (which is more robust). Furthermore, the dense model generation approach uses an energy function that can be optimised efficiently, using a smooth surface representation based on bicubic patches [47], which allows for defining a surface per view that has continuous depth and normals.

2.3. Defectology Analysis

Imperfections are anomalies that occur in the welded joint. They are considered as a flaw when, due to their magnitude or location, they could compromise the integrity and/or functionality of the part and/ or cause the failure of the joint. The generation of accurate and reliable photogrammetric point clouds models allows the application of different analyses oriented to the extraction of characteristics and the detailed evaluation of the state of the bead (Figure 2). In particular, the defectology analysis was developed considering four different types of defects (references in [2]) and the limits established in the international standard [3]:

- *Excess weld metal* (*H*) (ref. 502): it is related to the height of the bead over the plaque, *H*. The following criterion (B level) is established: $H \geq 1$ mm $+ 0.1 \times T$, *T* being the

width of the bead (max h = 0.5 mm). If this value exceeds 10% of the bead width, a defectology warning will be generated.

- *Linear misalignment* (*d*) (ref. 5071): it is related to the different heights between plaques, *d*. The following criterion (B level) is established: $d \geq 0.1 \times t$, *t* being the thickness of the plaque. If this value exceeds 10% of the plaque thickness, a defectology warning will be generated.
- *Angular misalignment* (δ) (ref. 508): it is related to the different orientations between plaques, δ. The following criterion (C level) is established: $\delta [n_l - n_r] \geq 2°$, being n_l and n_r the normal vector of plaque left and right, respectively.
- *End crater pipe* (*dz*) (ref. no. 2025): it consists of the detection of holes or depressed areas in the weld beam, *dz*. The most efficient way to detect them is by analysing the transversal profiles resulting from the weld, establishing a threshold of $dz < 0.2\ t$, *t* being the thickness of the plaque, with a maximum of 2 mm (D level).
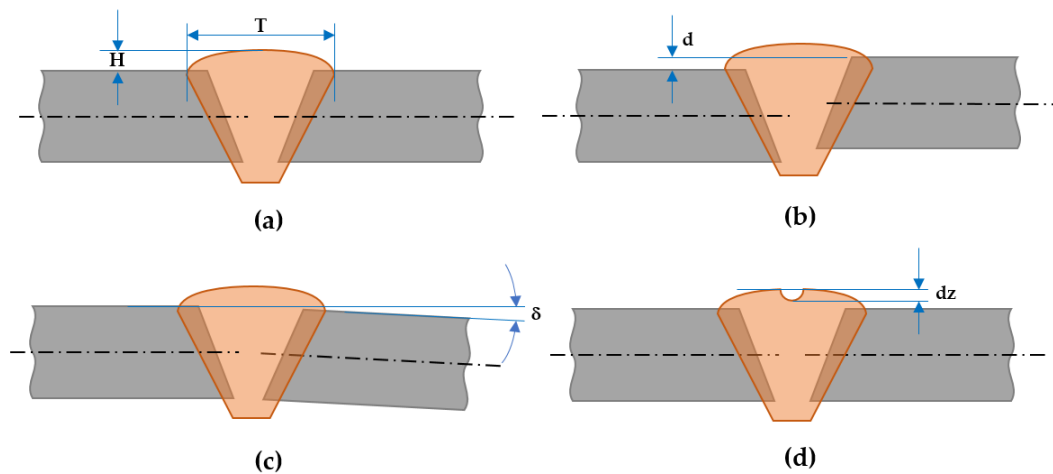
Figure 2. Defects and quality criterions considered in the WELDMAP software: (**a**) excess weld metal; (**b**) linear misalignment; (**c**) angular misalignment; (**d**) crater.

All these defects were analysed using cross-sections along the weld, using the axis of the bead as a reference. Although the software allows the assessment of the weld from an automatic point of view, the photogrammetric point clouds allow for inspecting the main metric characteristics of the weld (quantitative analysis), as well as its visual appearance (qualitative analysis). For instance, the existence of possible friction-affected areas and/or corrosion zones can also be evaluated from a qualitative point of view.

2.3.1. Weld Segmentation and Axis Definition

For the segmentation and extraction of the weld axis, the algorithm classifies the points by computing a set of geometric attributes and minimising a globally regularised energy (Equation (1)). Particularly, different pointwise geometric attributes have been applied (i.e., orthogonal distance to plane, eigenvalues, elevation, etc.) accompanied by geometric relationships between characteristics and classes (energy functions) which have made it possible to classify the point clouds according to 3 classes: (i) left plaque; (ii) right plaque; (iii) bead. Classification is achieved by minimising an energy function over the input point cloud by selecting, for each point, the classification type that gives the best score. More precisely, an energy minimisation was proposed to classify the point cloud. The energy function $E(x)$ is defined as a sum of partial data terms $E_{di}(x_i)$ and pairwise

geometric relationships defined by the standard Potts model [48], which integrates spatial coherence between neighbouring elements:

$$E(x) = \sum_{i=1...N} E_{di}(x_i) + \gamma \sum_{i \sim j} 1_{x_i \neq x_j} \tag{1}$$

where $\gamma > 0$ is the parameter of the Potts model which quantifies the regularisation force, $i \sim j$ represent the pairs of neighbouring points, and $1_{\{.\}}$ is the characteristic function. The partial data term $E_{di}(x_i)$ measures the coherence of the class x_i at the ith point. A Graph-Cut based algorithm [49] is applied to minimise the energy function and get a solution.

Finally, once the photogrammetric point clouds have been classified in three different classes, the axis of the bead is extracted based on the computation of centroids along the bead, using RANSAC algorithm (RANdom SAmple Consensus) for the robust fit of the axis [50].

2.3.2. Cross-Sections Generation and Defects Analysis

Once the bead and the plaques have been extracted, an automatic cross-sectional analysis can be performed using the extracted axis as reference. With this analysis, it is possible to locate flaws and imperfections according to the four defects previously defined (Figure 2). Cross-sections are plotted successively and automatically along the direction of the weld axis. The distance between sections could be freely chosen by the inspector according to the level of resolution required, the type of weld, the material, and the defects or imperfections to be detected and measured [9].

Finally, the four defects considered in Figure 2 can be checked for each cross-section deriving a complete analysis of the whole weld, as follows:

- The excess weld metal, H, was computed automatically, extracting the width of the bead based on the semantic classification of the bead along the axis and taking the median as a robust reference [51].
- The linear misalignment, d, was computed automatically, extracting the orthogonal distance between plaques based on the classification of the plaques along the axis and considering the median as a robust reference. The thickness of the weld, t, was provided by the manufacturer or measured directly in the 3D model.
- The angular misalignment, δ, was computed by applying principal component analysis (PCA) to those points in P_l, P_r that belong to the left and right plaques previously classified. Particularly, the third eigenvector was estimated as a normal vector for each plaque, n_l, n_r and thus used for computing the angular misalignment, δ, between plaques. Here, a threshold value of 0.9 was empirically defined, so normal vectors with the lower vertical component were discarded.
- The presence of notches or pores, dz, was computed adjusting a plane to the plaques previously classified using RANSAC algorithm [50] and analysing the orthogonal distance from the cross-sections to the fitted plane. All those points that generate an orthogonal distance ≥ 2 mm were considered as notches or pores.

3. Results and Discussion

3.1. Study Cases

A dataset composed of different types of metallic welds and joints was used to validate the WELDMAP software. We try to cope with different welds typologies in order to adapt the tool to its demanded use. This dataset was generated with images acquired in different real scenarios (e.g., shipyard and industry) and in the laboratory using specific samples (Figure 3).

Figure 3. Different types of metallic welds acquired in real scenarios and in the laboratory.

3.2. Results and Discussion

The results were obtained by applying the workflow outlined in Figure 1 and the defectology analysed, described in Figure 2, taking multiple RGB images as input data. These images were acquired using a photogrammetric stereoscopic arm composed of two reflex cameras (Canon EOS 700D) with two macro-lenses (EF-S 60 mm) (Figure 4). Trying to check the robustness of the feature extraction and matching process codified in WELDMAP, we used also images acquired with a compact handheld camera (Panasonic Lumix DMC-FZ38). In this case, images were acquired by varying their distances and perspective to reinforce the invariability of the detectors and descriptors.

Subsequently, the images were uploaded to WELDMAP. At each stage of the process (Figure 1) the final user can choose among different algorithms. In order to help the final user to choose among them, the platform incorporates integrated help for the different application cases.

In order to improve the feature extraction and matching (Figure 5), all input images were pre-processed based on the same algorithm: recursively separated and weighted histogram equalisation (RSWHE) [31], since RSWHE preserves the image brightness more accurately and produces images with better contrast enhancement.

All employed detectors were limited in the maximum number of keypoints (5000) and the used matching strategy was robust matching, supported by RANSAC using the fundamental matrix as a geometric test [25]. All the computations were performed by exploiting parallel and GPU capabilities of the hardware. This setup was enough for providing good matches between images, even in those cases with more geometric and radiometric variations between images (dataset coming from a compact handheld camera).
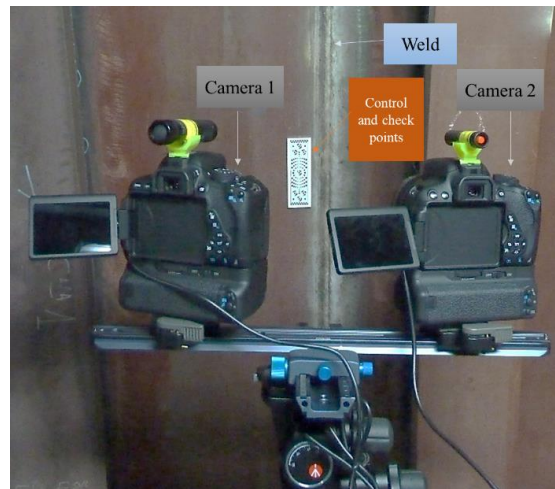
Figure 4. Stereoscopic photogrammetric arm composed by two reflex cameras (Canon EOS 700D) with two macro-lens (EF-S 60 mm).
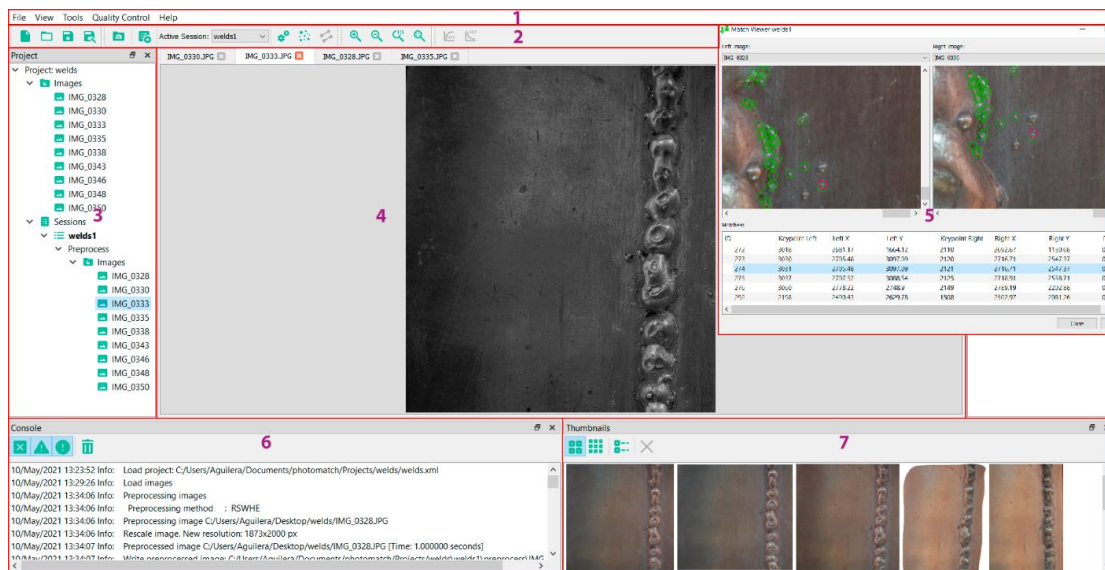
Figure 5. Feature extraction and matching in WELMAP software. In red are highlighted the different parts of the interface: menu (1), toolbar (2), tree view of the different inputs and intermediate results of the projects (3), view of the individual images (4), pop-up window with the matching results (5), console (6), and thumbnails (7).

The best combination was obtained by experimenting with the different welds considered, so that the end user is offered this configuration.

For these cases, an MSD detector [36] combined with an SIFT descriptor [33] was the best combination. For the stereoscopic dataset, the SIFT, supported by the GPU [52], provided very good results. For these cases, the MSD detector [36] combined with SIFT descriptor [33] was the best combination. For the stereoscopic dataset, the SIFT supported by GPU [52] provided very good results.

Once images were connected based on matchings, an orientation and self-calibration of the different sets of images were performed combining triangulation supported by the DLT and the BA using the collinearity condition applied in an incremental way. Likewise,

this registration process allowed us to revalidate the feature extraction and matching, since a wrong feature extraction and matching would entail an incorrect orientation and self-calibration of images. Finally, a dense model of the welds was provided based on the method described above. For the dataset coming from the compact handheld camera, the 3D models of welds were scaled based on a known distance using a codified target as reference. This was not the case for the stereoscopic dataset, since the point cloud are directly scaled based on the known and calibrated baseline. The following figure (Figure 6) outlines the photogrammetric 3D models of welds obtained, as well as the quality of the photogrammetric 3D models generated (Table 1).
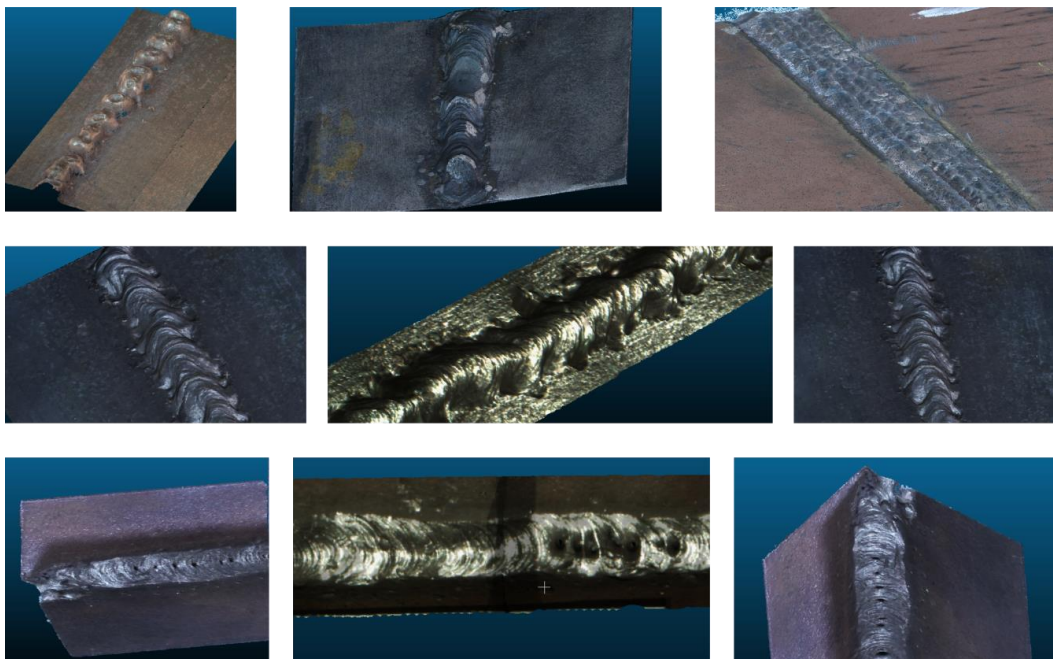
Figure 6. Sample of the 3D photogrammetric models obtained with WELDMAP software.

Table 1. Quality results of the photogrammetric 3D models obtained with the different cameras.

	Photogrammetric Stereoscopic Arm	Compact Handheld Camera
Resolution (mm)	0.05–0.06 mm	≤0.2 mm
Precision (mm)	0.10–0.15 mm	≤0.4 mm

As it was expected, higher quality can be observed in both spatial resolution and precision with the photogrammetric stereoscopic arm. This is due to the strong and efficient configuration defined with the stereoscopic setup in terms of images matching, photogrammetric reconstruction, and dense model generation. Furthermore, the constraint defined by the known baseline between cameras allowed us to work directly with metric models. This is not the case with the compact handheld camera, where the 3D models had to be scaled using artificial targets. On the contrary, it should be noted the greater flexibility and speed of acquisition with the compact handheld sensor, guaranteeing more forward speed and being especially suitable for non-expert operators in photogrammetry, since following a simple protocol of acquisition, the structure from motion approach can successfully solve the photogrammetric 3D model of the weld.

The resolution and precision achieved by photogrammetry improved substantially when compared to the ones achieved by the methods currently used, based on the visual

inspection of welds using manual gadgets (e.g., fillet weld gauge, cam gauge). These analogical methods allow verifying if the fillet is acceptable, but they do not allow technicians to record the geometry of the bead. Furthermore, they do not provide submillimetric accuracy and they are highly dependent on the inspector's skills and expertise. Alternative methods based on geotechnologies have been developed, for example in [53], where a laser-based machine vision system allowed for the monitoring and controlling of welding with a maximum error of 0.55 mm. In [54], a laser line scanner was employed to measure the surface profile of the weld bead. Despite it having a 0.015 mm spatial resolution, it only allowed for measuring a distance of 100 mm with a width of 24 mm. Besides, the classification between bead and base metals was unsatisfactory.

Afterwards, and based on these photogrammetric 3D models, a semantic classification of the welds using geometric features and an unsupervised classification strategy based on Graph Cut was applied, taking three classes as input: left plaque (red colour), right plaque (yellow colour) and bead (blue colour). The axis extraction is outlined in white colour (Figure 7).
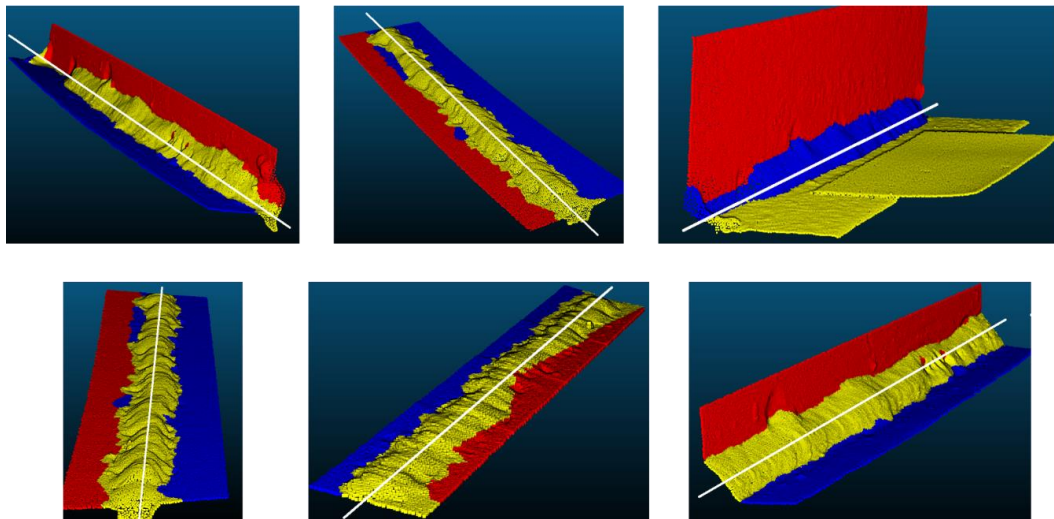

Figure 7. Sample of the semantic weld 3D models taking the plaques (red and blue), bead (yellow), and bead axis (white) as the main elements.

It should be noted the accurate and successful results of the classification strategy based on geometric features and energy function. The energy model has a relatively simple formulation and provides convincing results in practice. Figure 7 shows the potential of the model on different types of welds. Trying to validate the results, we obtained an expert on welds who checked the results, inspecting the semantic 3D models visually.

Once the welds were semantically classified, the quality control of welds was performed based on the four defects defined (Figure 2), using cross-sections as reference. Since the process is fully automatic, cross-sections were generated with 2.5 mm resolution. Figure 8 and Table 2 show the results of the defectological analysis of the welds assessed. Only those welds which present a defect are outlined in Table 2.

In view of Table 2, the efficiency of the WELDMAP tool to detect anomalies automatically is clear. It should be noted that the tool allows you to configure the threshold of defects as well as their percentage to consider if a weld should be rejected. In this sense, it must be emphasised that the welds inspected in situ did not provide any defectology, while the welds analysed in the laboratory (no. 1, 2, 3, 4, 5, 6), which came from defective welds, were those that showed the pathologies outlined in Table 2.
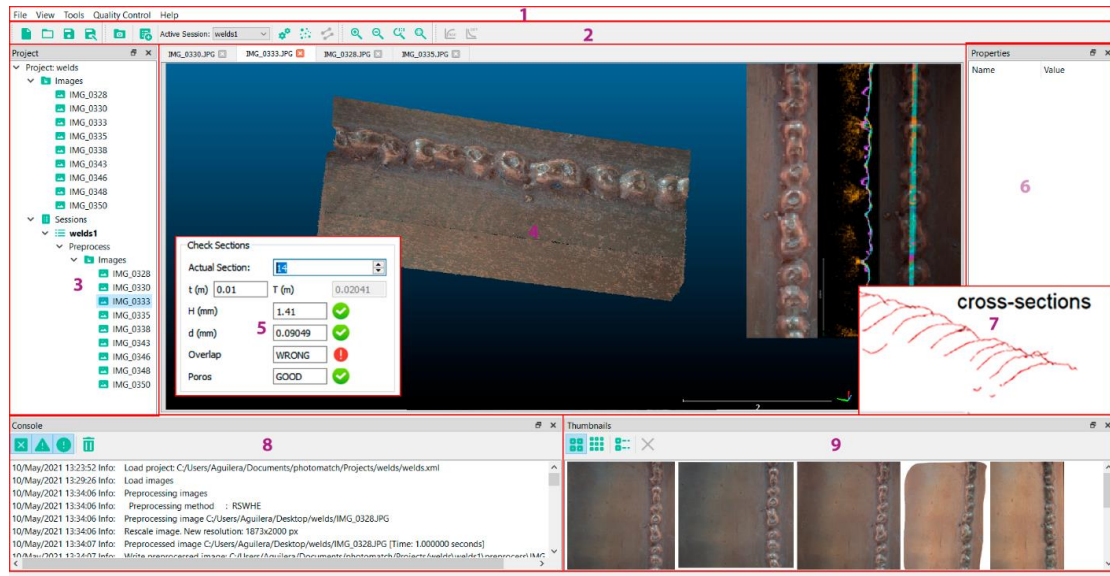
Figure 8. Quality control of welds based on cross-sections and the four defects analysed. In red are highlighted the different parts of the interface: menu (1), toolbar (2), tree view of the different inputs and intermediate results of the projects (3), 3D model viewers (4), pop-up window with the defects analysis (5), property view (6), pop-up window with the cross-sections generated (7), console (8), and thumbnails (9).

Table 2. Results of the four defects assessed in WELDMAP software. In red colour are highlighted those defects which did not pass the threshold established. Only those cross-sections which produced defects are reported in the table. T is the width of the bead, t is the width of the weld, n_l and n_r the normal vectors of the right and left plaques, respectively.

Type of Defect	Criterion for the Quality Assessment (mm/°)	No. Weld	Positioning along Bead Axis x (mm)	Results	
Excess Weld Metal	$H \geq 0.1T + 1$	1	28.2	$2.59 \geq 1.98$	not pass
		4	150.8	$3.01 \geq 1.75$	not pass
		6	161.0	$4.23 \geq 3.98$	not pass
Linear misalignment	$d \geq 0.1t$	1	23.4	$0.75 \geq 0.70$	not pass
		2	74.5	$1.45 \geq 1.20$	not pass
		5	110.9	$0.68 \geq 0.50$	not pass
Angular misalignment	$\delta [n_l - n_r] \geq 2°$	3	15.3	2.5	not pass
		3	90.6	2.7	not pass
		3	115.4	3.0	not pass
Notch or pore	$dz \geq 2$ mm	1	12.3	2.3	not pass
		4	60.6	2.8	not pass
		5	116.3	3.2	not pass

4. Conclusions

In this article, an unprecedented tool has been presented that integrates the possibility of providing smart photogrammetric models based on the quality control of welds. Under the name WELDMAP, the ability to reconstruct 3D welds, both geometrically and radiometrically, allow us to perform external quality control according to normalised standards. More specifically, this article proposes the use of RGB images acquired with reflex cameras as a non-destructive and low-cost technique for the digitisation of welded joints and the automation of their quality control by means of an in-house software, successfully tested

in different scenarios and with different types of welds. The results come to support its usefulness, since today these quality control tasks have been carried out visually supported by expeditious measures, and in most cases with an analogue record.

Looking ahead, it is expected to be able to work with images from other wavelengths (e.g., thermography, X-rays) and new materials (e.g., composites, fibres, etc.), so that multimodal registration techniques have to be incorporated together with the application of artificial intelligence techniques for quality inspection tasks. So, further developments will be carried out to include additional types of defects.

Author Contributions: Conceptualisation, E.R.d.O. and D.G.-A.; methodology, E.R.d.O., M.R.-M., P.R.-G. and D.G.-A.; software, R.M.; validation, M.R.-M. and P.R.-G.; formal analysis, D.G.-A., R.M. and M.R.-M.; writing—original draft preparation, E.R.d.O.; writing—review and editing, M.R.-M. and D.G.-A. All authors have read and agreed to the published version of the manuscript.

Institutional Review Board Statement: Not applicable.

Informed Consent Statement: Not applicable.

Data Availability Statement: Not applicable.

Conflicts of Interest: The authors declare no conflict of interest.

References

1. Nobrega, G.; Souza, M.S.; Rodríguez-Martín, M.; Rodríguez-Gonzálvez, P.; Ribeiro, J. Parametric Optimization of the GMAW Welding Process in Thin Thickness of Austenitic Stainless Steel by Taguchi Method. *Appl. Sci.* **2021**, *11*, 8742. [CrossRef]
2. *ISO 6520-1:2007*; Welding and allied Processes—Classification of Geometric Imperfections in Metallic Materials—Part 1: Fusion Welding. International Organization for Standardization: Geneva, Switzerland, 2007. Available online: https://www.iso.org/standard/40229.html (accessed on 29 December 2021).
3. *ISO 5817:2014*; Welding. Fusion-Welded Joints in Steel, Nickel, Titanium and Their Alloys (Beam Welding Excluded). Quality Levels for Imperfections. International Organization for Standardization: Geneva, Switzerland, 2014. Available online: https://www.iso.org/standard/54952.html (accessed on 29 December 2021).
4. *ISO 10042:2018*; Welding. Arc-Welded Joints in Aluminium and Its Alloys. Quality Levels for Imperfection. International Organization for Standardization: Geneva, Switzerland, 2018. Available online: https://www.iso.org/standard/70566.html (accessed on 29 December 2021).
5. *PD 5500:2018*; Specification for Unfired Fusion Welded Pressure Vessels. British Standards Institution: London, UK, 2018. Available online: https://shop.bsigroup.com/ProductDetail/?pid=000000000030366997 (accessed on 29 December 2021).
6. Rodríguez-Gonzálvez, P.; Rodríguez-Martín, M.; Ramos, L.F.; González-Aguilera, D. 3D reconstruction methods and quality assessment for visual inspection of welds. *Autom. Constr.* **2017**, *79*, 49–58. [CrossRef]
7. *ISO 17637:2016*; Non-Destructive Testing of Welds—Visual Testing of Fusion-Welded Joints. International Organization for Standardization: Geneva, Switzerland, 2016. Available online: https://www.iso.org/standard/67259.html (accessed on 29 December 2021).
8. *ISO 9712:2012*; Non-Destructive Testing—Qualification and Certification of NDT Personnel. International Organization for Standardization: Geneva, Switzerland, 2012. Available online: https://www.iso.org/standard/57037.html (accessed on 29 December 2021).
9. Rodríguez-Martín, M.; Lagüela, S.; González-Aguilera, D.; Rodríguez-Gonzálvez, P. Procedure for quality inspection of welds based on macro-photogrammetric three-dimensional reconstruction. *Opt. Laser Technol.* **2015**, *73*, 54–62. [CrossRef]
10. Zhang, L.; Ke, W.; Ye, Q.; Jiao, J. A novel laser vision sensor for weld line detection on wall-climbing robot. *Opt. Laser Technol.* **2014**, *60*, 69–79. [CrossRef]
11. Lei, T.; Rong, Y.; Wang, H.; Huang, Y.; Li, M. A review of vision-aided robotic welding. *Comput. Ind.* **2020**, *123*, 103326. [CrossRef]
12. Dinham, M.; Fang, G. Autonomous weld seam identification and localisation using eye-in-hand stereo vision for robotic arc welding. *Robot. Comput. Integr. Manuf.* **2013**, *29*, 288–301. [CrossRef]
13. Liu, Y.; Zhang, Y. Control of 3D weld pool surface. *Control Eng. Pract.* **2013**, *21*, 1469–1480. [CrossRef]

14. Caggiano, A.; Nele, L.; Sarno, E.; Teti, R. 3D Digital Reconfiguration of an Automated Welding System for a Railway Manufacturing Application. In Proceedings of the 8th International Conference on Digital Enterprise Technology, Stuttgart, Germany, 25–28 March 2014; Volume 25, pp. 39–45. [CrossRef]

15. Jia, N.; Li, Z.; Ren, J.; Wang, Y.; Yang, Y. 3D reconstruction method based on grid laser and gray scale photo for visual inspection of welds. *Opt. Laser Technol.* **2019**, *119*, 105648. [CrossRef]

16. Lei, T.; Wang, W.; Rong, Y.; Xiong, P.; Huang, Y. Cross-lines laser aided machine vision in tube-to-tube sheet welding for welding height control. *Opt. Laser Technol.* **2020**, *121*, 105796. [CrossRef]

17. Bračun, D.; Sluga, A. Stereo vision based measuring system for online welding path inspection. *J. Mater. Process. Technol.* **2015**, *223*, 328–336. [CrossRef]

18. Rodríguez-Martín, M.; Rodríguez-Gonzálvez, P.; Lagüela, S.; González-Aguilera, D. Macro-photogrammetry as a tool for the accurate measurement of three-dimensional misalignment in welding. *Autom. Constr.* **2016**, *71*, 189–197. [CrossRef]

19. Rodríguez-Martín, M.; Lagüela, S.; González-Aguilera, D.; Rodríguez-Gonzálvez, P. Crack-Depth Prediction in Steel Based on Cooling Rate. *Adv. Mater. Sci. Eng.* **2016**, *2016*, 1016482. [CrossRef]

20. Remondino, F. Heritage Recording and 3D Modeling with Photogrammetry and 3D Scanning. *Remote Sens.* **2011**, *3*, 1104–1138. [CrossRef]

21. Evgenikou, V.; Georgopoulos, A. Investigating 3d reconstruction methods for small artifacts. *Int. Arch. Photogramm. Remote Sens. Spat. Inf. Sci.* **2015**, *XL-5/W4*, 101–108. [CrossRef]

22. Rodríguez-Martín, M.; Rodríguez-Gonzálvez, P.; González-Aguilera, D.; Fernández-Hernández, J. Feasibility Study of a Structured Light System Applied to Welding Inspection Based on Articulated Coordinate Measure Machine Data. *IEEE Sens. J.* **2017**, *17*, 4217–4224. [CrossRef]

23. Gonzalez-Aguilera, D.; Ruiz de Ona, E.; Lopez-Fernandez, L.; Farella, E.M.; Stathopoulou, E.; Toschi, I.; Remondino, F.; Fusiello, A.; Nex, F. Photomatch: An open-source multi-view and multi-modal feature matching tool for photogrammetric applications. *ISPRS Ann. Photogramm. Remote Sens. Spat. Inf. Sci.* **2020**, *43*, 213–219. [CrossRef]

24. Schönberger, J.L.; Frahm, J. Structure-from-Motion Revisited. In *IEEE Conference on Computer Vision and Pattern Recognition (CVPR)*; IEEE: Las Vegas, NV, USA, 2016; pp. 4104–4113.

25. González-Aguilera, D.; López-Fernández, L.; Rodríguez-Gonzálvez, P.; Hernández-López, D.; Guerrero, D.; Remondino, F.; Menna, F.; Nocerino, E.; Toschi, I.; Ballabeni, A.; et al. GRAPHOS–open-source software for photogrammetric applications. *Photogramm. Rec.* **2018**, *33*, 11–29. [CrossRef]

26. Aicardi, I.; Nex, F.; Gerke, M.; Lingua, A.M. An image-based approach for the co-registration of multi-temporal UAV image datasets. *Remote Sens.* **2016**, *8*, 779. [CrossRef]

27. Gaiani, M.; Apollonio, F.I.; Ballabeni, A.; Remondino, F. Securing color fidelity in 3D architectural heritage. *Sensors* **2017**, *17*, 2437. [CrossRef]

28. Jende, P.; Nex, F.; Gerke, M.; Vosselman, G. A fully automatic approach to register mobile mapping and airborne imagery to support the correction of platform trajectories in GNSS-denied urban areas. *ISPRS J. Photogramm. Remote Sens.* **2018**, *141*, 86–99. [CrossRef]

29. Lal, S.; Chandra, M. Efficient algorithm for contrast enhancement of natural images. *Int. Arab. J. Inf. Technol.* **2014**, *11*, 95–102.

30. Liu, Y.F.; Guo, J.M.; Lai, B.S.; Lee, J.D. High efficient contrast enhancement using parametric approximation. In Proceedings of the 2013 IEEE International Conference on Acoustics, Speech and Signal Processing, Vancouver, BC, Canada, 26–31 May 2013; pp. 2444–2448. [CrossRef]

31. Kim, M.; Chung, M.G. Recursively separated and weighted histogram equalization for brightness preservation and contrast enhancement. *IEEE Trans. Consum. Electron.* **2008**, *54*, 1389–1397. [CrossRef]

32. Wallis, K.F. Seasonal adjustment and relations between variables. *J. Am. Stat. Assoc.* **1974**, *69*, 18–31. [CrossRef]

33. Lowe, D.G. Distinctive image features from scale-invariant keypoints. *Int. J. Comput. Vis.* **2004**, *60*, 91–110. [CrossRef]

34. Bay, H.; Tuytelaars, T.; Gool, L.V. SURF: Speeded-Up Robust Features. In *European Conference on Computer Vision*; Springer: Berlin, Germany, 2006; pp. 404–417. [CrossRef]

35. Matas, J.; Chum, O.; Urban, M.; Pajdla, T. Robust wide-baseline stereo from maximally stable extremal regions. *Image Vis. Comput.* **2004**, *22*, 761–767. [CrossRef]

36. Tombari, F.; Di Stefano, L. Interest Points via Maximal Self-Dissimilarities. In *Asian Conference on Computer Vision*; Springer: Cham, Swizerland, 2014; pp. 586–600. [CrossRef]

37. Rublee, E.; Rabaud, V.; Konolige, K.; Bradski, G.R. ORB: An efficient alternative to SIFT or SURF. In Proceedings of the 2011 International Conference on Computer Vision, Barcelona, Spain, 6–13 November 2011; pp. 2564–2571. [CrossRef]

38. Alcantarilla, P.F.; Nuevo, J.; Bartoli, A. Fast explicit diffusion for accelerated features in nonlinear scale spaces. In Proceedings of the British Machine Vision Conference 2013, Bristol, UK, 9–13 September 2013; Volume 34, pp. 1281–1298.

39. Leutenegger, S.; Chli, M.; Siegwart, R. BRISK: Binary robust invariant scalable keypoints. In Proceedings of the 2011 International Conference on Computer Vision, Barcelona, Spain, 6–13 November 2011; pp. 2548–2555. [CrossRef]

40. Trzcinski, T.; Christoudias, M.; Lepetit, V. Learning Image Descriptors with Boosting. *IEEE Trans. Pattern Anal. Mach. Intell.* **2014**, *37*, 597–610. [CrossRef]

41. Calonder, M.; Lepetit, V.; Ozuysal, M.; Trzcinski, T.; Strecha, C.; Fua, P. BRIEF: Computing a local binary descriptor very fast. *IEEE Trans. Pattern Anal. Mach. Intell.* **2011**, *34*, 1281–1298. [CrossRef]

42. Tola, E.; Lepetit, V.; Fua, P. Daisy: An efficient dense descriptor applied to wide-baseline stereo. *IEEE Trans. Pattern Anal. Mach. Intell.* **2010**, *32*, 815–830. [CrossRef]

43. Alahi, A.; Ortiz, R.; Vandergheynst, P. Freak: Fast retina keypoint. In Proceedings of the 2012 IEEE Conference on Computer Vision and Pattern Recognition, Providence, RI, USA, 16–21 June 2012; pp. 510–517. [CrossRef]

44. Schaffalitzky, F.; Zisserman, A. Multi-view matching for unordered image sets, or How do I organize my holiday snaps? In *European Conference on Computer Vision*; Springer: Berlin, Germany, 2002; pp. 414–431.

45. Abdel-Aziz, Y.I.; Karara, H.M.; Hauck, M. Direct linear transformation from comparator coordinates into object space coordinates in close-range photogrammetry. *Photogramm. Eng. Remote Sens.* **2015**, *81*, 103–107. [CrossRef]

46. Langguth, F.; Sunkavalli, K.; Hadap, S.; Goesele, M. Shading-aware multi-view stereo. In *European Conference on Computer Vision*; Springer: Cham, Switzerland, 2016; pp. 469–485.

47. Semerjian, B. A new variational framework for multiview surface reconstruction. In *European Conference on Computer Vision*; Springer: Cham, Switzerland, 2014; pp. 719–734.

48. Li, S. *Markov Random Field Modeling in Image Analysis*; Springer: Cham, Switzerland, 2001.

49. Boykov, Y.; Veksler, O.; Zabih, R. Fast approximate energy minimization via graph cuts. *IEEE Trans. Pattern Anal. Mach. Intell.* **2001**, *23*, 1222–1239. [CrossRef]

50. Fischler, M.A.; Bolles, R.C. Random sample consensus: A paradigm for model fitting with applications to image analysis and automated cartography. *Commun. ACM* **1981**, *24*, 381–395. [CrossRef]

51. Rodríguez-Gonzálvez, P.; Garcia-Gago, J.; Gomez-Lahoz, J.; González-Aguilera, D. Confronting passive and active sensors with non-Gaussian statistics. *Sensors* **2014**, *14*, 13759–13777. [CrossRef] [PubMed]

52. Wu, C. A GPU Implementation of Scale Invariant Feature Transform (SIFT). Available online: https://github.com/pitzer/SiftGPU (accessed on 2 January 2022).

53. Huang, W.; Kovacevic, R. Development of a real-time laser-based machine vision system to monitor and control welding processes. *Int. J. Adv. Manuf. Technol.* **2012**, *63*, 235–248. [CrossRef]

54. Ye, G.; Guo, J.; Sun, Z.; Li, C.; Zhong, S. Weld bead recognition using laser vision with model-based classification. *Robot. Comput. Manuf.* **2018**, *52*, 9–16. [CrossRef]

Capítulo 3

Validación de sistema de escaneado portátil en tareas de inspección

Capítulo 3

Validación de sistema de escaneado portátil en tareas de inspección

En este capítulo se incluye el artículo *"Validation of Portable Mobile Mapping System for Inspection Tasks in Thermal and Fluid–Mechanical Facilities"* publicado en la revista *Remote Sensing* en septiembre de 2019.

3.1. Resumen

Dentro de las tareas de mantenimiento, inspección y seguridad de instalaciones industriales, el registro tridimensional de las mismas tiene gran importancia. Desde hace un par de décadas los TLS se han venido usando para la captura 3D de entornos industriales. Actualmente también contamos con los PMMS que permiten la generación de modelos tridimensionales densos y georreferenciados mientras el operador se desplaza por la escena. Muchas tareas de mantenimiento e inspección podrían realizarse de forma más sencilla y en menos tiempo si se utiliza un PMMS en lugar de un TLS, por tanto, el objetivo de este estudio fue validar la viabilidad del uso de un sistema PMMS para las tareas de inspección en instalaciones térmicas y fluido-mecánicas.

Para la validación del PMMS (GeoSLAM Zeb-Revo) se realizó una comparativa con un TLS (Faro Focus 3D), tomando este último como verdad terreno. Para realizar la comparativa se estableció una metodología orientada a la extracción de los parámetros más críticos para la inspección de instalaciones industriales, la cual permite realizar un análisis cualitativo de diferentes elementos a partir de la nube de puntos generada por el PMMS.

La metodología de captura parte de la configuración de una red de referencia (mediante esferas) para poder georreferenciar las diferentes nubes de puntos ge-

neradas desde el Faro y el Zeb-Revo en el mismo sistema de coordenadas local. Posteriormente se hace un reconocimiento de la zona a escanear para planificar la toma de datos, tratando de minimizar las zonas ocultas y, en el caso del TLS, evitando estacionamientos innecesarios que redundarían en aumentar los errores de alineamiento de las nubes de puntos.

Una vez que ambos conjuntos de datos fueron alineados en el mismo sistema de referencia se usaron diferentes regiones de interés para el ajuste de las primitivas y la evaluación de la calidad a través de un análisis estadístico robusto. Las regiones escogidas para el análisis fueron tuberías, paredes y techos. Para la segmentación de las tuberías se realizó un ajuste de cilindros sobre la nube de puntos con RANSAC (*RANdom SAmple Consensus*). Por otra parte, el método para extraer los planos de piso y pared se basa en el algoritmo de análisis de componentes principales (PCA).

El análisis estadístico robusto permite comparar la desviación de los puntos discretos adquiridos del Zeb-Revo con respecto al cilindro ideal obtenido con Faro. En el caso de los planos ajustados a partir de las nubes de puntos de cada conjunto de datos se evalúa la discrepancia del ángulo entre los vectores normales. Los resultados mostraron desviaciones en las estimaciones de diámetros que oscilaron entre 9 y 16 mm, con resultados aceptables de sesgo y dispersión. En cuanto a la medición de ángulos, se registró una desviación de 1.3 mrad. Además, se demostró que era posible una adecuada diferenciación cualitativa en la nube de puntos de dispositivos que suelen estar presentes en las salas de máquinas, como válvulas de corte, reguladores de presión, entre otros.

Article

Validation of Portable Mobile Mapping System for Inspection Tasks in Thermal and Fluid–Mechanical Facilities

Manuel Rodríguez-Martín [1,2]**, Pablo Rodríguez-Gonzálvez** [3,*] **, Esteban Ruiz de Oña Crespo** [4] **and Diego González-Aguilera** [4]

[1]   Department of Mechanical Engineering, Universidad de Salamanca, 37700 Béjar (Salamanca), Spain; ingmanuel@usal.es
[2]   Technological Department, Catholic University of Ávila, 05005 Ávila, Spain
[3]   Department of Mining Technology, Topography and Structures. Universidad de León, 24401 Ponferrada, Spain
[4]   Department of Cartographic and Land Engineering. Universidad de Salamanca, 05003 Ávila, Spain; estebanrdo@usal.es (E.R.d.O.C.); daguilera@usal.es (D.G.-A.)
*   Correspondence: p.rodriguez@unileon.es; Tel.: +34-987-442-055

check for updates

Abstract: The three-dimensional registration of industrial facilities has a great importance for maintenance, inspection, and safety tasks and it is a starting point for new improvements and expansions in the industrial facilities context. In this paper, a comparison between the results obtained using a novel portable mobile mapping system (PMMS) and a static terrestrial laser scanner (TLS), widely used for 3D reconstruction in civil and industrial scenarios, is carried out. This comparison is performed in the context of industrial inspection tasks, specifically in the thermal and fluid-mechanics facilities in a hospital. The comparison addresses the general reconstruction of a machine room, focusing on the quantitative and qualitative analysis of different elements (e.g., valves, regulation systems, burner systems and tanks, etc.). The validation of the PMMS is provided considering the TLS as ground truth and applying a robust statistical analysis. Results come to confirm the suitability of the PMMS to perform inspection tasks in industrial facilities.

Keywords: optical sensors; robust statistical analysis; portable mobile mapping system; handheld; 3D processing; point cloud

1. Introduction

Traditionally, geomatics techniques have been used mainly for the determination and recording of terrain and outdoor scenarios in surveying engineering. However, they also can be applied in industrial context and energy applications [1–4]. In this way, geomatics techniques can be used to generate three-dimensional models of large and complex scenes as nuclear power plants [5], the generation of as-built models in architecture [6,7] or, even, for metrological tasks related with the quality assessment of products [8–11]. Portable mobile mapping systems (PMMSs) allow the generation of dense, geo-referenced, three-dimensional models while the operator is moving though the scene [12]. This novel technology has been developed in the last years becoming the most innovative and emerging technique in surveying tasks [4].

The scope of application of PMMSs is diverse: from cultural heritage constructions [13] and civil structures to industrial sites [14], indoor spaces [15], and natural environments [16]. PMMSs contain two groups of sensors that act in a synchronized way to reconstruct the scene three-dimensionally: navigation and remote sensing modules. The navigation module usually is based on an inertial

measurement unit (IMU) and, sometimes, it also can be equipped with a Global Navigation Satellite System (GNSS) receiver. The remote sensing module normally is based on a laser scanning sensor and, sometimes, also different types of cameras. A deep review about this emerging technology and the different typologies of PMMSs is presented in [12].

The PMMS analyzed in this paper is the GeoSLAM Zeb-Revo [17] (from now on, Zeb-Revo). Nowadays, it is one of the most widespread PMMSs, and several investigations have addressed its use for different purposes as natural space management [16], cultural heritage documentation [18], underground documentation [19,20], and disaster analysis [21], among others. In Zeb-Revo, the navigation module is based on an IMU, whereas the remote sensing module is a 2D laser profilometer. The latter is a compact laser scanning range finder which is more compact and light-weight than a traditional 3D laser scanner system and its battery consumption is more optimal [22]. In [23], Zeb-Revo and Leica Pegasus-Backpack were compared with a Z+F Terrestrial Laser Scanner (TLS), providing Zeb-Revo discrepancies around 4 cm. In [22], a robust statistical comparison between Zeb-Revo and Leica Pegasus-Backpack was performed. Although it was demonstrated that both systems performed within manufacturer specifications, Zeb-Revo generally outperformed the manufacturer values despite the presence of outliers.

The adequate distribution of thermal and fluid-mechanical equipment (such as boilers, tanks, heat exchangers, valves, and others) within the machine rooms is an important issue that must be subject of a rigorous study, especially in singular facilities such as hospitals. The tasks of expansion, maintenance, inspection, and improvement of thermal and fluid-mechanical installations require prior knowledge of the elements of the installation as a starting point. Additionally, the criteria for the equipment distribution are normally indicated by international and/or national standards and regulations (e.g., [24,25]). For this reason, meeting the geometric and technical requirements based on standards and regulations is a mandatory task for the facilities engineers. Many of these requirements are based on geometrical criteria such as distance among boilers or other equipment, geometric and volumetric conditions of the rooms, spaces for maintenance tasks, empty spaces for emergency exits, etc. The generation of a three-dimensional model of machine rooms using PMMS is a powerful tool to ensure the quality and efficiency of the service, allowing the registration of the different elements and devices of the installation and their state of conservation, reducing in this manner the risk of possible maintenance problems, making future improvement actions easier such as the expansion of the facilities or improvement actions, all based on accurate, scaled, and duly documented geospatial information. The design and calculation of the facilities must be carried out according to the technical criteria indicated in the standards and regulations, for example, the allowed pipe diameters. The design and calculation of the thermal facilities must be carried out according to the technical criteria that indicate standards [26]. The calculation criteria—for example, the location of valves, the dimensions of the equipment, etc.—must be computed following these indications, being the finished facilities subject to inspection processes also regulated by these standards. Due to this, inspection and documentation tasks are mandatory to certify that the installation meets the standards, consequently, the use of methods that three-dimensionally record these spaces are totally justified. In [4], a method based on PMMS is proposed for the maintenance of machine rooms, providing the automatic extraction of pipes with relative deviation ranges between 0.50% and 11.21% of the mean diameter value.

The aim of this work was to validate the inspection effectiveness of a PMMS, Zeb-Revo, by comparing its results with those obtained with a TLS, Faro Focus 3D, whose survey was used as reference. As a result, many maintenance and inspection tasks could be done in a simpler way and in less time if a PMMS is used instead of a TLS. After this introduction, this paper is structured as follows: Section 2 describes the methodology and materials employed. Experimental results are presented in Section 3, along with the robust statistical analysis. Discussion is detailed in Section 4, whereas the main conclusions are presented at the end of the paper (Section 5).

2. Materials and Methods

A specific methodology for data analysis was stablished to compare the potential of the PMMS, Zeb-Revo, for the evaluation of fluid-mechanical facilities, using a TLS, Faro Focus3D, as ground truth.

2.1. Materials

Zeb-Revo [16] can be considered as the natural evolution of the first version, ZEBedee, which was developed by the CSIRO ICT Center in Brisbane (Australia) [27,28]. This scanning device is based on a 2D profilometer (Hokuyo UTM-30LX) which can be displaced using a platform support. Moreover, Zeb-Revo is equipped with an IMU as navigation module, which is continuously rotating during data acquisition. Then, the device can be equipped with a commercial camera GoPro Hero installed to record the scenario during the data acquisition and, in this manner, the different scanned elements can be easily located on video. It is especially useful because Zeb-Revo does not record radiometry information, so differentiating zones only based on geometry (without color information) is difficult. The 2D laser profilometer is a compact laser scanner, which is more efficient, light-weight, and compact than any TLS used for three-dimensional reconstruction [22].

Due to the continuous rotation of the sensor and the movement of the operator, three-dimensional information (i.e., points) is acquired. The data are stored in a server with a hard disk that is located in a backpack, which is part of the equipment. Specific features of the Zeb-Revo are indicated in Table 1.

Table 1. Technical features of the PMMS, Zeb-Revo.

Parameter	Value
Measurement range (indoor) (m)	30
Measurement range (outdoor) (m)	15
Data capture speed (points/s)	43,200
Accuracy	±0.1%
Relative accuracy	1-3 cm
Field of view	270° × 360°
Operating time (h)	4
Scanner dimensions (mm)	86 × 113 × 470
Weight (kg)	0.85
Rotation frequency (Hz)	0.5

For its part, a TLS, FARO Focus3D 120 (from here, Faro) (Figure 1), was used for the scanning of the reference point cloud (ground truth). This device consists on an infrared laser scanner which takes measures directly using the principle of phase shift in the range of 0.60–120 m at a wavelength of 905 nm. Its field of view covers 320° vertically and 360° horizontally, allowing an angular resolution of 0.009° and a measurement rate of 976,000 points per second, recording radiometric information for each point. The precision provided by the manufacturer is of 2 mm in normal lighting conditions with a beam divergence of 0.19 mrad. This device allows a high accuracy three-dimensional reconstruction, so it was chosen as the ground truth [29].

Furthermore, three reference spheres (14.5 cm of diameter) were required and located in different points of the scene to register the different individual point clouds acquired by Faro and, also, for the subsequent alignment of the point clouds acquired by Zeb-Revo. The spheres acted as reference providing a common Coordinate Reference System (CRS) for the comparison.

2.2. Methods

The developed methodology (Figure 2) was designed specifically for the evaluation of the derived products obtained with the PMMS, Zeb-Revo, specifically oriented to the extraction of the most critical parameters for the inspection of industrial facilities. In addition, the methodology allows the qualitative analysis of in-detail elements from the point cloud generated by the PMMS, Zeb-Revo.

Figure 1. Faro Laser Scanner Focus 3D S (Left) by courtesy of www.faro.com; and GeoSlam Zeb-Revo (Right) by courtesy of https://geoslam.com.
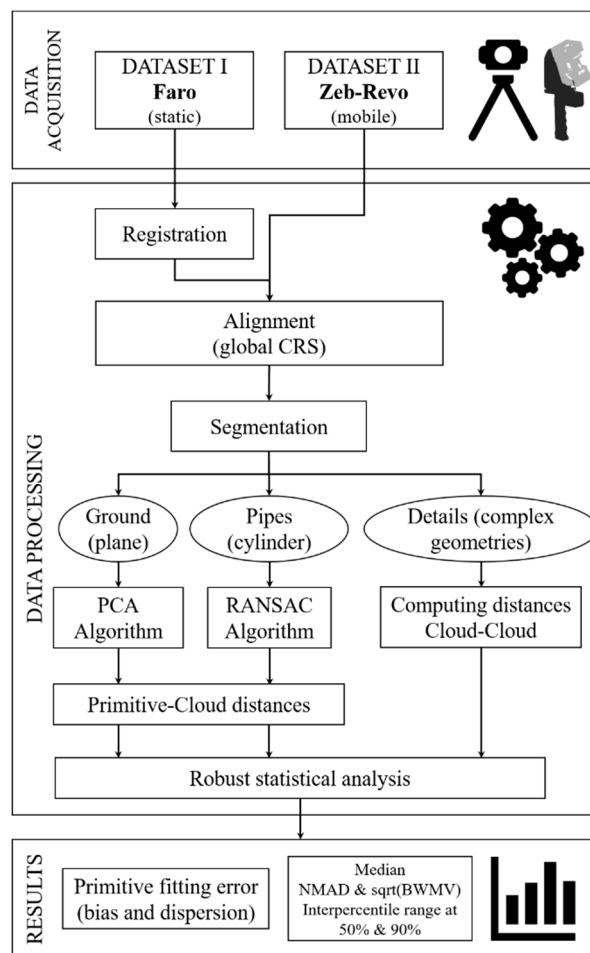
Figure 2. Pipeline for the validation of portable mobile mapping system for inspection tasks in thermal and fluid-mechanical facilities.

2.2.1. Data Acquisition

The first step was the data acquisition which was addressed using both devices (Faro-Dataset I and Zeb-Revo-Dataset II) but, previously, a reference network was set up to analyze the different point clouds generated from Faro and Zeb-Revo in the same CRS. This reference network was designed with

spheres attached to different metal parts of the scene, using neodymium magnets to ensure that they remain static during the data acquisition (Figure 3).

Figure 3. Sphere located in a pillar of the machine room (attached by a neodymium magnet).

Regarding the protocol for data acquisition, the PMMS requires to start and finish in the same position of the scene. For this reason, the trajectory planned using Zeb-Revo follows a closed-loop. This trajectory must be established to specifically cover the complete machine room minimizing occlusions. Please note that the error of this kind of PMMS typically increases with time/length of the walk. The maximum data acquisition time provided by the manufacturer (working in continuous mode) is approximate twenty minutes, after which the quality of the reconstruction may be reduced. This time requirement is enough to scan extensive industrial facilities with a single-loop (if that was not enough, several loops could be used to generate different point clouds). Data acquisition protocol contemplates a preliminary inspection of the scene to plan a suitable data acquisition path, detect potentially physical obstacles (e.g., equipment, tools or pipes on the floor, drips, etc.) that would affect the data acquisition and remove them if it is necessary and/or possible.

Once PMMS data (Dataset II) was acquired, the point cloud of the scene was registered in a local CRS. If ground control points are visible in the acquired data, the point clouds can be georeferenced in a global CRS using a rigid Helmert transformation. Alternatively, the individual point clouds can be also referenced in the same local CRS implementing an iterative closest point (ICP) registration [30]. For additional details about Zeb-Revo processing, the reader is referred to [12].

Data acquisition was performed planning the path inside the building (450 m^2) and requiring approximately four minutes. The total track was about 115 m long, so the walking speed was near 0.43 m·s^{-1}, or 1.6 km·h^{-1}. The front part of the sensor was always oriented in the direction of advance. A part of the followed trajectory and a 3D view of the reconstruction using the manufacturer's software (GeoSLAM) is shown in Figure 4.

Once the Dataset II using the PMMS was obtained, the TLS, Faro, was used to gather the Dataset I, which was used as ground truth. The data acquisition protocol with the TLS was carefully designed, so that the complete scanning area was covered with the minimum number of scans in order to minimize possible alignment errors. In this way, data acquisition with TLS was implemented from four different positions to ensure that the entire scene was covered. The resulting and aligned point cloud of the machine room was used to validate the dataset obtained with Zeb-Revo.

2.2.2. Data Processing

Once data acquisition protocol for Dataset I (Faro) and Dataset II (Zeb-Revo) was implemented, data processing strategy was applied over the point clouds generated with both laser systems, in order to extract the results. Data processing methodology (Figure 2) was fully oriented to compare the obtained results using Zeb-Revo with respect to the ground truth defined with Faro.
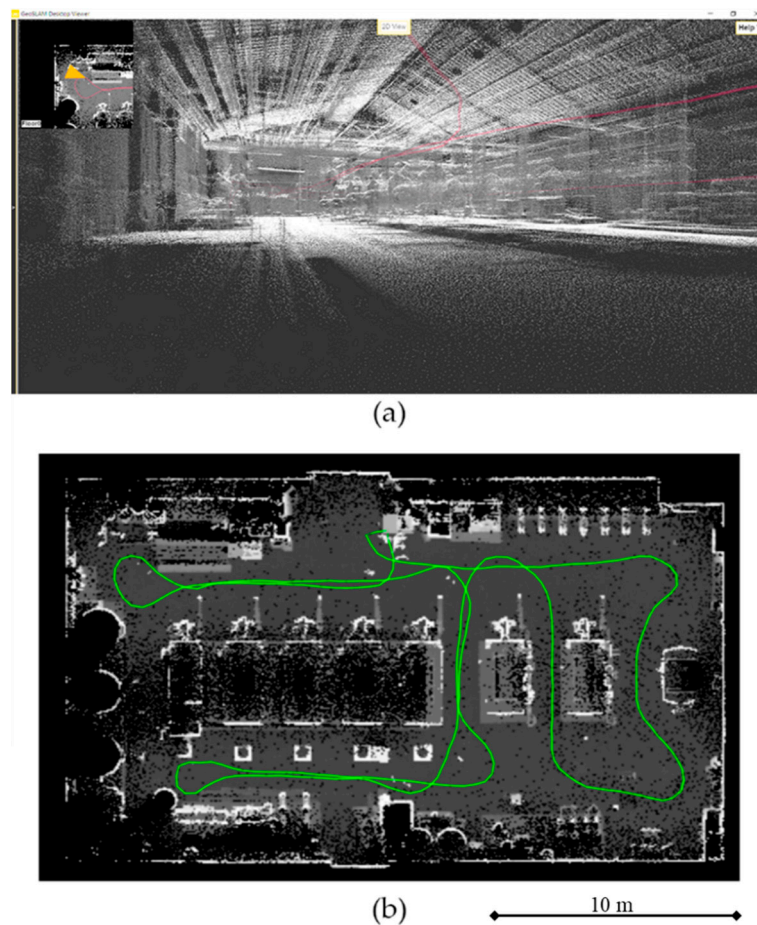
Figure 4. Three-dimensional scene shown by GeoSlam viewer (**a**) and followed trajectory during the data acquisition (green line) (**b**).

Point Clouds Processing: Merging, Alignment, and Segmentation

Dataset I (Faro) was composed by four individual point clouds (Figure 5a) generated from different positions in order to cover the entire scene. Point clouds were merged using the aligning algorithms provided by Faro Scene software. Spheres distributed along the scene were used to stablish plane-to-plane correspondences, which provide the initial approximations for the ICP [31]. As a result, a single point cloud with 165,829,378 points was obtained from the Dataset I (Faro).

Both dataset (Dataset I-Faro, Dataset II-Zeb-Revo) were aligned under the same CRS using the aforementioned spheres. For the alignment process, firstly, the three spheres were segmented for each point cloud and, subsequently, the centers of the spheres were extracted using a RANSAC-based sphere fitting [32]. The standard deviation (SD) resulting from the fitting is shown in Table 2.

In this way, three invariant references (centers of spheres) were obtained with an acceptable fitting error (Table 2), acting as homologous points for each dataset. The average error of the sphere fitting was 3.5 mm and 6.2 mm for the TLS (Dataset I) and the PMMS (Dataset II), respectively. The alignment between both point clouds was implemented by means of CloudCompare [33]. This software provides a registration tool which can align two point clouds if there are at least three corresponding point pairs in both datasets.

The root mean square error (RMSE) of the individual Faro scans was 6.2 mm, whereas the RMSE of the alignment of the PMMS point cloud to the reference system was 12.1 mm. Note that the alignment error between the individual TLS point clouds generates an error propagation in the subsequent analysis—e.g., the cylinder fitting—especially in the small pipes.

Once both datasets (Figure 5) were georeferenced in the same CRS, different regions of interest were used for primitives fitting and quality assessment through a robust statistical analysis (Figure 6).
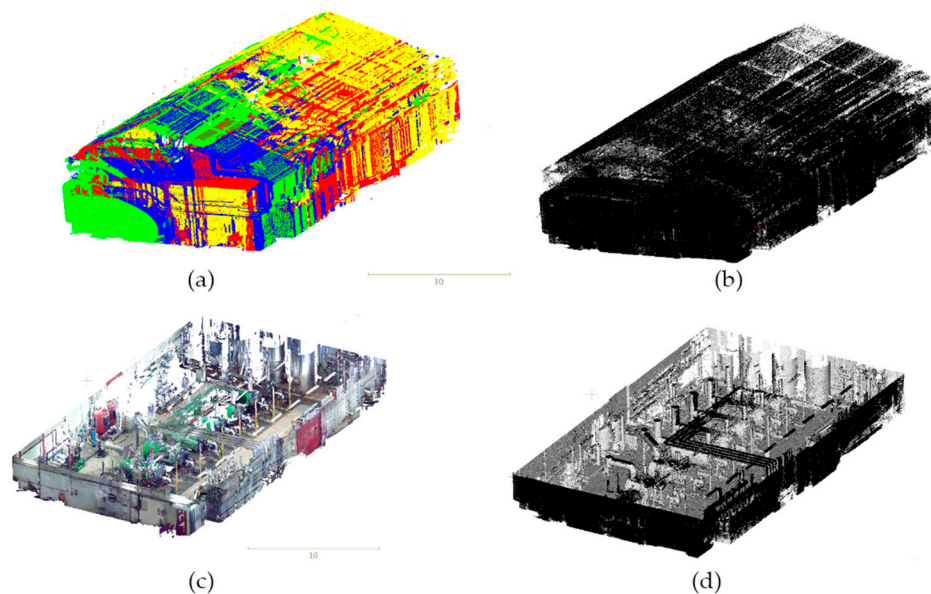
Figure 5. Dataset I: four point clouds obtained and aligned with Faro (**a**). Dataset II: point cloud obtained with Zeb-Revo (**b**). Dataset I: segmented point cloud to appreciate the distribution of facilities using Faro. (**c**). Dataset II: segmented point cloud to appreciate the distribution of facilities using Zeb-Revo (**d**).

**Table 2.** Standard deviation of the RANSAC-based sphere fitting to align both datasets in a global CRS.

Sphere	SD (m)	
	Zeb-Revo	**Faro**
1	±0.0064	±0.0041
2	±0.0067	±0.0038
3	±0.0057	±0.0026

The regions chosen for the analysis are the next:

1. Pipes (cylindrical regions): Thermal and fluid-mechanics facilities as the machine rooms normally have numerous pipes with different diameters, typologies and lengths that join the boilers and other equips with the gas connections, with the residual gas evacuations and with the water circuits. For this reason, focusing on inspection tasks, it can be necessary to check if the installed pipes are appropriate considering the design specification criteria for the thermal and fluid-mechanic facilities and the standards and regulations. Furthermore, the registration of pipes is highly useful for maintenance tasks and the parameters of the installed pipes as the diameter must be also considered for future modifications or expansion of the installation. These reasons motivated the choice of diameters as main parameters to be extracted from the point clouds for the identification of the pipes. In this way, three representative pipe regions were chosen for each boiler (Figure 7). These were chosen for having the smallest diameter (e.g., gas pipes which inject the gas into the boiler) and the largest diameter (e.g., water return pipe). This last was evaluated in two different locations: in the connection with the boiler and in the roof (Figure 7a,b). The aim is to control the deviation between the point clouds used to fit the pipes using Zeb-Revo and Faro.

2. Planes referring to the interior enclosures of the machine room: the planes fitted from the vertical walls and the floor are chosen because these regions have interest for the documentation

of volumetric parameters of the rooms, which are relevant for design and maintenance tasks as calculation of ventilation conditions, lighting design, emergency exists, etc. Furthermore, the relative location between the enclosures, the equipment and pipes are criteria to consider for compliance with standards and regulations.

a.　　Floor plane: One portion of the floor was chosen. The selection of this region was not easy because there were lot of obstacles which prevent its adequate segmentation. This region was selected without obstacles in order to analyze better its deviation (Figure 6).

b.　　Wall plane: Two portions of vertical walls were chosen (Figure 6). Again, these regions were selected without obstacles for providing a better analysis (Figure 6).
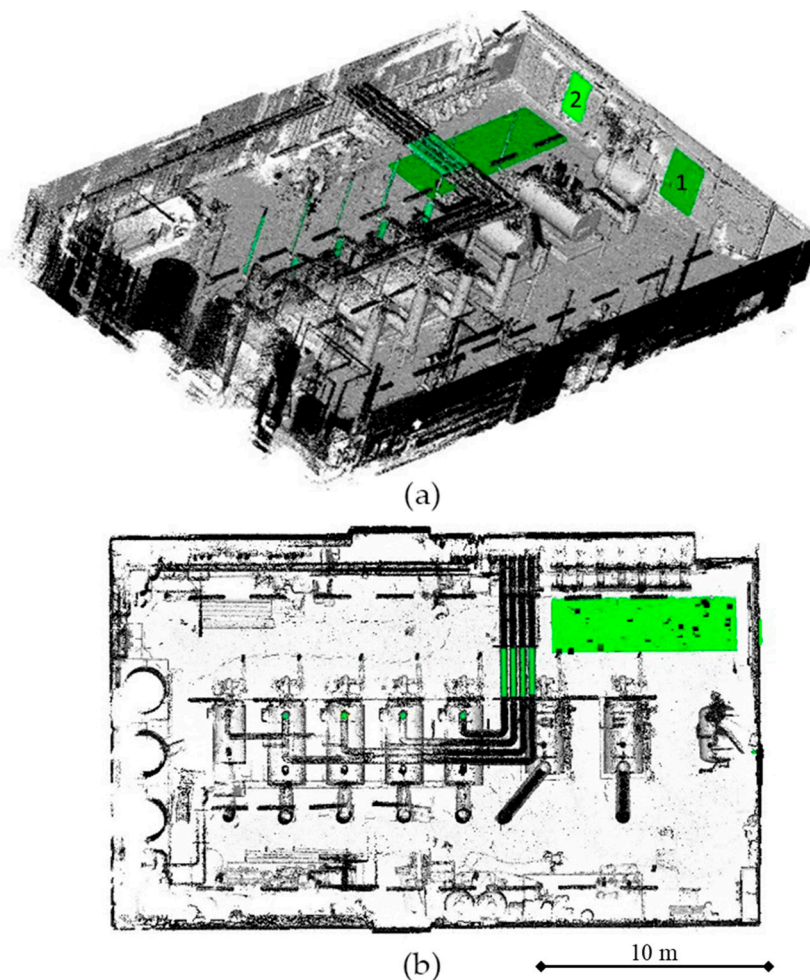
Figure 6. Different regions of interest used to fit the cylinders and planes (marked in green). The wall planes 1 and 2 are numbered in (**a**); while the floor planes and pipes highlighted are also shown in (**b**).

Feature Extraction of Pipes

First, to extract features of pipes a cylinder fitting was applied [32]. Particularly, this algorithm is based on a voting strategy well-known as RANSAC and can be implemented to detect different continuous and idealized geometries from point clouds (e.g., planes, spheres, cylinders, torus, etc.). In this case, the algorithm was applied to fit cylinders from the point clouds acquired in both datasets (Faro, Zeb-Revo). Once the cylinder was fitted, important features as diameters, lengths and a position were obtained. The quality of the adjustment was assessed through the discrepancy of each discrete point with respect to the ideal fitted cylinder.
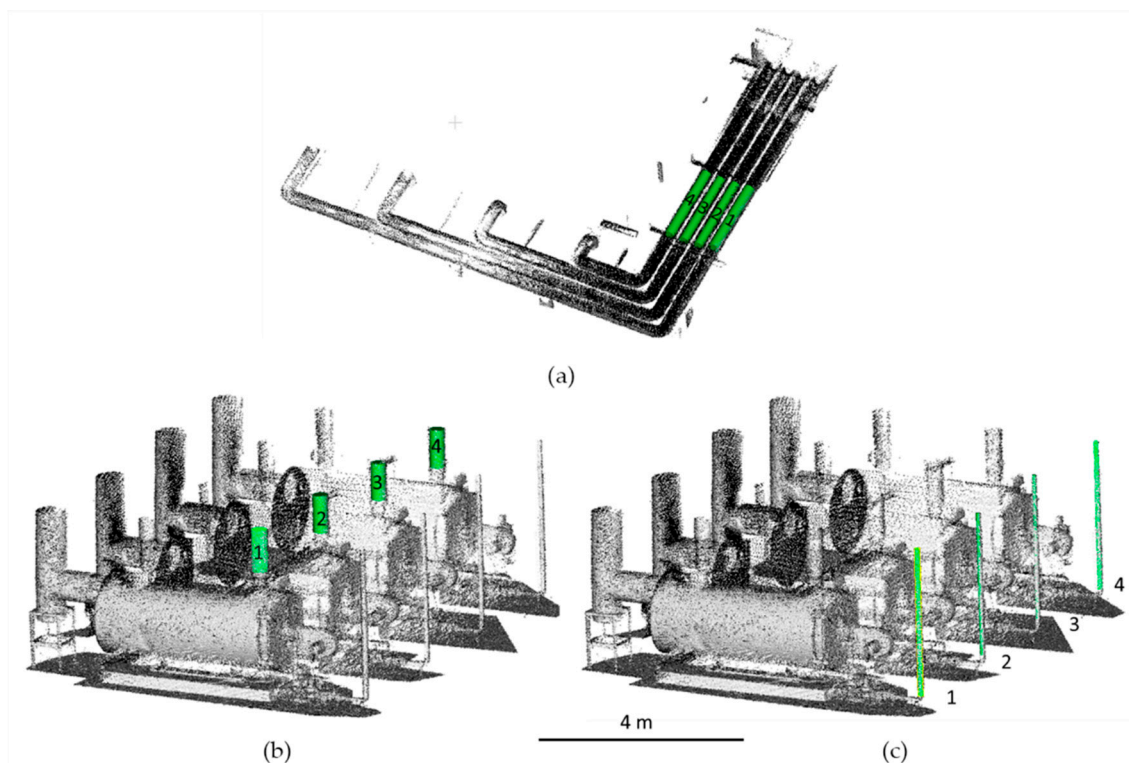
Figure 7. Regions of interest (pipes) used to fit the cylinder primitives: Water return pipe region located in the floor (**a**), water return pipe region located in the boiler (**b**), and gas pipe region (**c**).

Feature Extraction of Floor and Walls

The method to extract the features of the floor and wall regions is based on principal components analysis (PCA) algorithm which has been successfully applied to extract, from photogrammetric point clouds, geometrical features as angles between normal vectors of planes for the misalignment calculation of the steel welded plaques [8,34], as well as to compute the local 3D feature extraction for a machine learning classification of weld beads [35]. Specifically, PCA through the covariance matrix allows us to calculate the main components of the spatial points distribution, using the computation of eigenvectors. For instance, the eigenvector extracted from the smallest eigenvalue (λ_0) indicates the normal direction (v_0) to the fitting plane, and thus the normal direction for the wall and floor planes. Considering a point cloud of n points with coordinates x, y, z where x_m, y_m, z_m are the centroid coordinates, the covariance matrix (2) for each of them is calculated from the matrix of points (**W**). The covariance matrix (**C**) has the values of the variance in the principal diagonal (2). By the diagonalization process of matrix **C**, the eigenvectors of the covariance matrix are obtained, and as a result, the three eigenvalues (λ_1, λ_2, λ_3).

$$\mathbf{W} = \begin{pmatrix} x_1 - x_m & y_1 - y_m & z_1 - z_m \\ \vdots & \vdots & \vdots \\ x_n - x_m & y_n - y_m & z_n - z_m \end{pmatrix} \tag{1}$$

$$\mathbf{C} = \frac{1}{n}\mathbf{W}^T\mathbf{W} = \begin{pmatrix} \sigma_{xx} & \sigma_{yx} & \sigma_{xz} \\ \sigma_{yx} & \sigma_{yy} & \sigma_{yz} \\ \sigma_{zx} & \sigma_{zy} & \sigma_{zz} \end{pmatrix} \tag{2}$$

Using this procedure, planes were fitted from point clouds for both datasets (Faro-Dataset I, Zeb-Revo-Dataset II). The residuals were processed as the distance between each discrete point and the fitted planes. In this way, SD was calculated for the initial evaluation of the quality of the

adjustment. Also, the misalignment between the planes was calculated (in mrad) as the angle between the normal vectors.

Primitive Fitting Error and Robust Statistical Analysis

Once planes and cylinders were fitted, a primitive fitting error was provided. The objective was to compare the Zeb-Revo results (Dataset II) with Faro results (Dataset I) used as ground truth. In this respect, point-primitive distances were computed for the elements described in the previous sections (Figures 6 and 7), concretely for the two pipes (Figure 8) and for all the planes. In addition, a robust statistical analysis was applied over the samples to avoid the effect caused by outliers. In this context, several studies [36–38] demonstrated that in the accuracy assessment of data provided by laser scanner systems, as well as photogrammetry, the hypothesis that errors follow a Gaussian distribution is hardly verified. This might be due to the presence of residual system errors, but also to the presence of undesirable scanned objects [22]. In the following analyses non-parametric estimators, the median m, normalized median absolute deviation (NMAD) (3) and the square root of the biweight midvariance (BWMV) (4), were employed. Specifically, the NMAD (3) allows to compare error dispersions from Gaussian samples, since it is normalized by the inverse of the cumulative distribution function of the Gaussian [39]
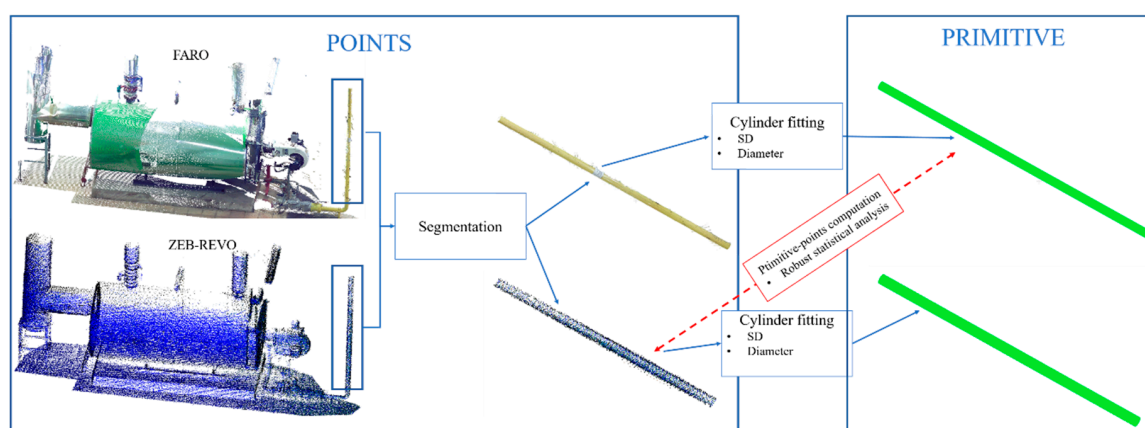
$$\text{NMAD} = 1.4826 \cdot \text{MAD} \tag{3}$$

$$\text{BWMV} = \frac{n\sum_{i=1}^{n} a_i (x_i - m)^2 \left(1 - U_i^2\right)^4}{\left(\sum_{i=1}^{n} a_i \left(1 - U_i^2\right)\left(1 - 5U_i^2\right)\right)^2} \tag{4}$$

$$a_i = \begin{cases} 1, \; if |U_i| < 1 \\ 0, \; if |U_i| \geq 1 \end{cases} \tag{5}$$

$$U = \frac{x_i - m}{9\text{MAD}} \tag{6}$$

being the median absolute deviation MAD (7) the median (m) of the absolute deviations from the data's median (m_x)

$$\text{MAD} = m(|x_i - m_x|) \tag{7}$$

Figure 8. Procedure used to compare the different point clouds in pipes regions. The same procedure is following to compare the plane regions.

Additionally, the interpercentile range (IPR) at 50% and 95% of confidence level were reported. Please note also that due to the asymmetry of the error distribution was not possible to provide a plus-minus range, but an absolute interpercentile range; therefore, the percentile values at 2.5% and 97.5% were reported to outline the aforementioned asymmetry.

3. Results

As consequence of the direct application of the proposed methodology, results were obtained. In this way, a comparison between the cylinders fitted from the two datasets (Faro and Zeb-Revo) is shown in Tables 3–5, whereas the results for the planes fitted (roof and walls) are shown in Table 6. Results from the robust statistical analysis where points from Zeb-Revo were compared with respect to the cylinders and planes fitted from Faro are outlined in Tables 7 and 8.

Table 3. Diameters discrepancies and standard deviations (SD) obtained from the RANSAC cylinder fitting of the pipes: gas pipe regions (Figure 7).

			Gas Pipe			
Regions	Diameter TLS (m)	SD TLS (m)	Diameter PMMS (m)	SD PMMS (m)	Discrepancy (m)	% Discrepancy
1	0.078	±0.001	0.097	±0.008	−0.019	24.08%
2	0.076	±0.001	0.094	±0.008	−0.019	24.70%
3	0.075	±0.001	0.093	±0.007	−0.018	24.34%
4	0.077	±0.001	0.088	±0.007	−0.010	13.08%
					−0.016	21.55%

Table 4. Diameters discrepancies and standard deviations (SD) obtained from the RANSAC cylinder fitting of the pipes: water return pipe regions located in the boiler (Figure 7).

			Water Return Pipe (Connection in the Boiler)			
Regions	Diameter TLS (m)	SD TLS (m)	Diameter PMMS (m)	SD PMMS (m)	Discrepancy (m)	% Discrepancy
1	0.287	±0.002	0.298	±0.021	−0.011	3.94%
2	0.284	±0.003	0.294	±0.014	−0.010	3.52%
3	0.284	±0.003	0.290	±0.014	−0.006	2.11%
4	0.282	±0.003	0.291	±0.016	−0.009	3.34%
					−0.009	3.23%

Table 5. Diameters discrepancies and standard deviations (SD) obtained from the RANSAC cylinder fitting of the pipes: water return pipe regions located in the roof (Figure 7).

			Water Return Pipe (Roof)			
Regions	Diameter TLS (m)	SD TLS (m)	Diameter PMMS (m)	SD PMMS (m)	Discrepancy (m)	% Discrepancy
1	0.285	±0.004	0.275	±0.018	0.010	3.47%
2	0.242	±0.007	0.260	±0.026	−0.018	7.24%
3	0.245	±0.005	0.265	±0.017	−0.020	8.22%
4	0.275	±0.006	0.275	±0.014	−0.000	0.11%
					0.012	4.76%

3.1. Cylinder Fitting for Pipes

The standard deviation (SD) and diameter discrepancies of the cylinders fitted were calculated (Figure 8) (Tables 3–5). Ideally, this discrepancy must be zero but, in this case, it is a useful accuracy measure of the method.

Table 6. Results of the fitting for the vertical planes (walls) and horizontal plane (roof) from point clouds regions (Figure 6).

		Number of Points	Normal Vector Coordinates			SD (m)	Misaligned Angle (Mrad)
			x	y	z		
Floor plane	Faro	3896744	−0.0023	0.0024	1.0000	0.0026	1.334
	Zeb-Revo	120780	−0.0036	0.0027	1.0000	0.0070	
Vertical wall 1	Faro	406026	0.3903	0.9027	−0.0037	0.0019	4.567
	Zeb-Revo	9387	0.3927	0.9197	−0.0033	0.0088	
Vertical wall 2	Faro	443852	0.3935	0.9193	0.0049	0.0017	11.250
	Zeb-Revo	19784	0.3967	0.9179	−0.0058	0.0083	

Table 7. Gaussian vs. Robust statistical analysis: Different regions analyzed (1–4) comparing the discrete points from Zeb-Revo with respect to the fitted surface (cylinder or plane) generated from Faro.

	Gaussian Assessment							Robust Assessment					
	Kurtosis	Skewness	Sample Mean	Sample Deviation	Median	MAD	NMAD	Sqrt (BWMV)	IPR 50%	Perc. 0.025	Perc. 0.975	IPR 95%
Water return pipe (boiler) (2)	6.353	0.618	0.002	0.012	0.001	0.007	0.011	0.012	0.014	−0.020	0.026	0.047
Water return pipe (boiler) (3)	3.694	0.343	0.003	0.014	0.003	0.009	0.014	0.014	0.019	−0.023	0.034	0.057
Gas pipe (2)	2.941	0.202	0.008	0.009	0.007	0.006	0.009	0.009	0.013	−0.009	0.028	0.037
Gas pipe (3)	4.201	−0.043	0.008	0.007	0.008	0.004	0.007	0.007	0.009	−0.006	0.022	0.028
Water return pipe (roof) (3)	32.028	3.213	0.001	0.020	0.000	0.010	0.014	0.015	0.020	−0.030	0.039	0.069
Water return pipe (roof) (4)	3.441	0.047	−0.003	0.014	−0.003	0.009	0.013	0.014	0.018	−0.030	0.026	0.055
Vertical wall (1)	79.303	3.399	−0.027	0.009	−0.027	0.005	0.007	0.008	0.010	−0.042	−0.011	0.031
Vertical wall (2)	4.277	0.184	−0.013	0.008	−0.013	0.005	0.007	0.008	0.010	−0.029	0.005	0.034
Floor plane	11.701	0.146	−0.003	0.007	−0.003	0.004	0.006	0.006	0.008	−0.016	0.011	0.027

Table 8. Summary of bias and dispersion data for the analyzed regions (1–4) comparing the discrete points from Zeb-Revo with respect to the fitted surface (cylinder or plane) generated from Faro.

	Bias	Dispersion					
	Median (mm)	NMAD (mm)	Sqrt (BWMV) (mm)	IPR 50% (mm)	IPR 95% (mm)	Perc 0.025	Perc 0.975
Water return pipe (boiler) (2)	1.4	±10.9	±11.6	14.5	46.5	−20.3	26.3
Water return pipe (boiler) (3)	2.6	±13.7	±14.0	18.6	57.3	−23.2	34.1
Gas pipe (2)	7.5	±9.4	±9.5	12.7	36.6	−9.0	27.6
Gas pipe (3)	8.0	±6.5	±6.8	8.8	28.2	−6.1	22.1
Water return pipe (roof) (3)	−0.4	±14.5	±15.5	19.5	68.8	−29.9	38.9
Water return pipe (roof) (4)	−3.2	±13.4	±13.8	18.2	55.4	−29.7	25.8
Vertical wall (1)	−27.2	±7.1	±7.6	9.7	31.2	−41.8	−10.6
Vertical wall (2)	−12.8	±7.4	±8.0	10.0	34.1	−29.0	5.1
Floor plane	−3.2	±5.9	±6.4	8.0	26.9	−16.3	10.7

The SD for the fitting process for the Dataset I (Faro) was between 1 and 7 mm (being higher in those cylinders located on the roof). These results (Tables 3–5) were considered as reference for comparison (ground truth).

As it was indicated in Tables 3–5, the diameter discrepancies obtained with both sensors (Faro and Zeb-Revo) were between 0.6 and 1.9 cm for all the analyzed pipes, but analyzing discrepancies in relative terms, the deviation between the two diameters of the two cylinders fitted (Faro and Zeb-Revo) was notably higher for small diameter cylinders (21.55%) than for large diameter cylinders (3.2% and 4.8%).

The computation of distances between the point clouds obtained using Zeb-Revo (Dataset II) and the cylinders fitted from the Dataset I (Faro); and the subsequently application of the robust statistical analysis gave some results (Table 7) that can be summarized in the next way:

1. Bias results: the median in the cylinders of bigger diameter is between 2.6 and -3.2 mm, whereas for cylinders of smaller size the median is around 8 mm (Table 7). The latter is compatible with the difference in diameter of approximately 1 cm between the cylinders adjusted for both sensors (Table 3).
2. Dispersion results: Robust analysis using the normalized median absolute deviation (NMAD) and the interpercentile range (IPR) (Tables 7 and 8) shows higher dispersion results for cylinders with larger diameter, always remaining at 1.45 and 0.65 cm, whereas dispersion results are smaller for smaller diameters. The latter and the results of median indicate that there is an initial bias in the cylinders with a small diameter and this error is not due to the dispersion of the data obtained with Zeb-Revo. Please note, that gas pipes shown the highest discrepancies in relative values, but in the present analysis (absolutes values) they are lowest. This behavior is caused by the discrepancy computation which depends inversely proportional to the cylinder diameter.

The robust statistical analysis carried out also discards that the distribution of distances of the points obtained with Zeb-Revo with respect to the cylinders adjusted with Faro follows a Gaussian distribution (on the basis of a visual inspection of a quantile-quantile plot).

3.2. Plane Fitted for Floor and Wall Regions

The standard deviation of the fitting was calculated for each plane (Figure 8). The SD of the fitting is between 1.7 and 2.6 mm for the Dataset I (Faro) and between 7 and 8.8 mm for Dataset II (Zeb-Revo). These results are consistent because the accuracy of Faro is around 2 mm and the expected accuracy of Zeb-Revo is centimetric. The results of Dataset I were considered as reference for comparison for the subsequent robust statistical analysis.

The computation of distances between the cloud of points obtained with Zeb-Revo (Dataset II) and the cylinders fitted from Faro (Dataset I) and the application of the robust statistical analysis gave some results that can be summarized as follows (Table 8):

1. Bias results: The median in vertical planes (walls) was significantly higher than in horizontal plane (floor). It could be the consequence of an initial bias of unknown origin, which, as hypothesis, could be caused by the different surface finish of wall in relation to the floor one, as well, as the relative position and distance regarding the path of the PMMS data acquisition.
2. Dispersion results: Robust statistical analysis with MAD and IPR showed homogeneous dispersion results in all cases (Tables 7 and 8).

### 3.3. In-Detail Elements: Qualitative Analysis

Different discrete elements have been segmented from point clouds in order to qualitatively assess the level of visualization of these. In Figure 9 is shown a gas pressure regulator system (usually installed in thermal installations) located at the entrance of the boilers. As the reader can see, the difference in the resolution between the two datasets is important but the points of the PMMS are enough for the

identification of the valve, because the three elements of the system are distinguishable. Note that both point clouds present outliers.
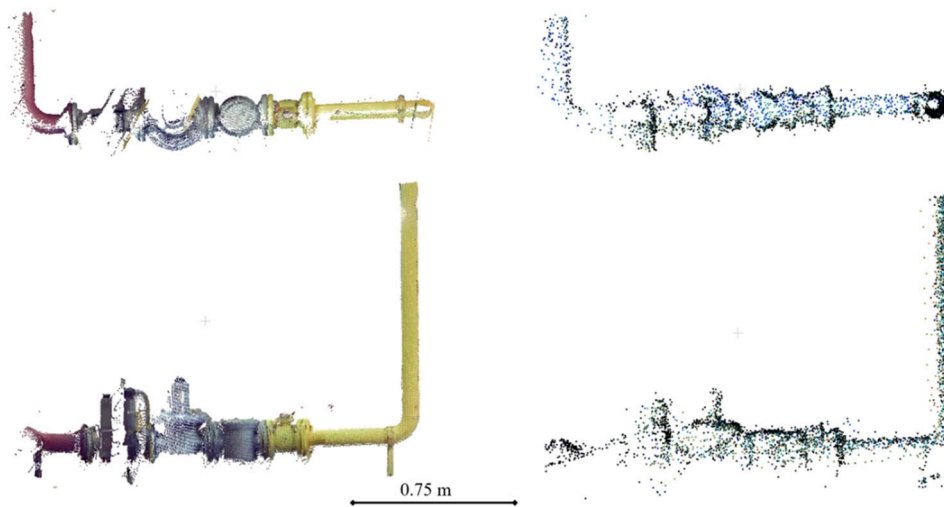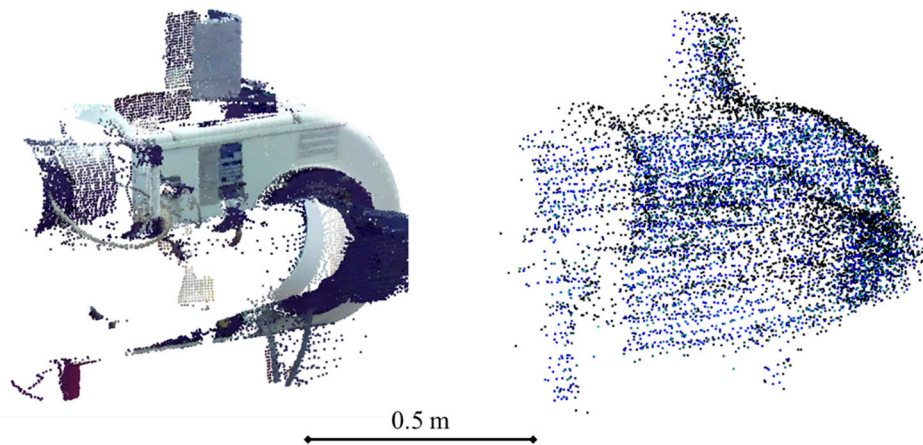

Figure 9. Example of points clouds of the pressure regulation system located at the entrance of the gas in the boilers obtained with Faro (Left) and with Zeb-Revo (Right).

In Figure 10, a cutting valve (usual in most fluid-mechanical installations) is located in the connection to the boiler water pipe. In this, the geometry of the valve is defined in both point clouds, however the final part of the grip is not appreciated in the PMMS point cloud, whereas in the TLS point cloud the valve is fully appreciated. In Figure 11, a boiler burner is shown. In this case, the completeness is higher in the PMMS point cloud but the final part of the grip is not appreciated in the TLS point cloud. This is due to the fact that PMMS takes the data in motion and all the zones are covered, whereas the TLS is static, and the completeness of the models depends on the number of stations of the laser scanner. Finally, a hot water tank is shown in Figure 12. In this case, the same thing happens: the PMMS point cloud is more complete than the TLS point cloud, while this last presents a higher resolution and detail perception.
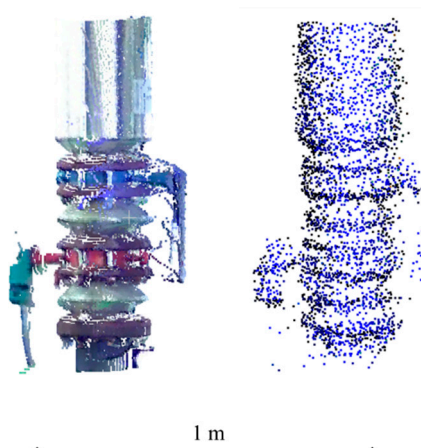
Figure 10. Example of points clouds of the cutting valve at the entrance of the water in the boilers obtained with Faro (Left) and with Zeb-Revo (Right).

Figure 11. Example of points clouds of the burner system located in the boilers obtained with Faro (Left) and with Zeb-Revo (Right).
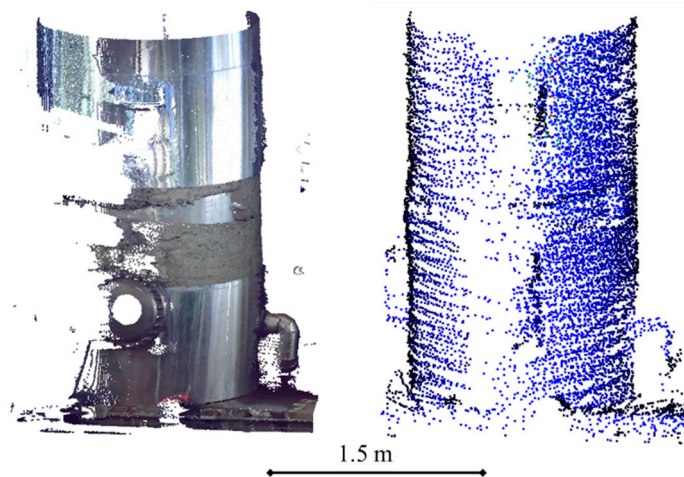
Figure 12. Example of point clouds of the hot water tank obtained with Faro (Left) and with Zeb-Revo (Right).

4. Discussion

Indoor mapping and modeling is probably the main application scenario for PMMS. This becomes even more significant in the specific case of industrial facilities, where the present elements can be reconducted on the basis of parametric geometries and therefore deliver a BIM. For this case, PMMS offers the best compromise between spatial resolution, precision, surveying time, and cost [12].

The potential advantages of PMMS can be summed up on the completeness of the data acquisition thanks to the maneuverability and flexibility of the PMMS in complex scenarios; and the speed of acquisition due to the lack of static stations. Regarding the advantages of the PMMS in relation to the TLS, the key factor is the reduced surveying time. In the present study case, the surveying time for the 4 TLS scans encompassed 28 min and 40 s, whereas the PMMS required only 4 min and 18 s. Ergo, the surveying time was reduced in almost seven times, obtaining at the same a comparable level of completeness.

The results of the primitive fitting are inside the interval expected on the basis of the manufacturer a-priori precision (standard deviation lower than 3 cm). However, in terms of the computed pipe diameters, there was identified a bias. Considering the analysis of the pipes, the bias existing in the smaller pipes is significant. This could be caused by the alignment error during the SLAM processing. Since the precision of the PMMS is about 1 to 3 cm, this error becomes noteworthy for pipes diameters about 8 cm. However, other error sources are not excluded, such as the high curvature of the pipe

and/or the surface finish. As a result, this issue will require further investigations. Regarding the water pipes, due to the larger diameter, the relative discrepancy is lower than 5% (Tables 4 and 5). Please note that in the case of the roof water pipes the discrepancies could reach a bit higher values (up to 8.2% as stated in Table 5). This could be caused by the object–sensor distance and the lower completeness due to the limited point of view and small distance among pipes.

The extension of the pipe analysis from the diameter value up to the complete pipe, the PMMS point cloud discrepancies, against the primitive from TLS, decrease for the small pipes (gas), whereas for the larger (water), the discrepancy is zero centered in a ±3 mm interval. Therefore, the PMMS is a suitable sensor for the maintenance, inspection, and safety tasks in fluid-mechanical installation, due to the lack a significant bias, and relative diameter discrepancies lower than 5%. For the gas pipes (diameters lower than 10 cm), the use of the PMMS is limited to general documentation purposes (e.g., location of the pipes).

The static nature of the TLS data acquisition gave place to occlusions in the reference point cloud, but also non-acquisition of parts of the fluid-mechanical installations (e.g., valves, grips). This first issue (occlusions) could not be especially relevant in the primitive fitting due to the careful planning of data acquisition phase; however, the absence of TLS data causes outliers in the point-to-point analysis. So, this discrete analysis requires to take into account the point's neighborhood to avoid mismatches in the discrepancy calculation. Regarding the non-acquisition of small parts, the dynamic nature of the PMMS makes it more suitable than TLS to document industrial facilities.

Regarding the plane analysis, the primitive fitting from PMMS point cloud is compatible with the technical specifications. The derived robust confidence intervals are more symmetrical than the pipes ones. The IPR 95% lower than 35 mm is a very significant results related to the PMMS ability to record this kind of complex environment. For both vertical planes, a significant bias was detected, that could be caused by the surface finish (in relation to the floor plane). In addition, the object-sensor relative position during the data acquisition path (see Figure 4) could be another explanation for the abovementioned bias. The last possible error source is a residual error from the alignment procedure carried out with spheres. This effect is inevitable, but it is diminished by the fact of being both active sensors (the scale parameter is not expected to be significant), remaining only the error from the sphere network design and sphere centroid extraction. However, the centimetric error provided by the PMMS unlike the millimetric error of the TLS, can generate an error in the alignment of the point clouds which justify the bias. The obtention of additional information as the plane misalignment can check the plane orientation, a normally neglected aspect in the analysis of 3D fitting. As expected, the floor plane misalignment is not significant, since it is in the same precision range than the precision construction levels (approximately 0.1 gons). However, for the wall planes it is noticed a significant put-of-plumb condition, with an equivalent displacement of 2 to 4.5 cm for a four meters height (value which exceeds the tolerances of the support plates of the beams used for industrial installations). This angular discrepancy can be attributed to the aforementioned wall's surface finish, and to a lesser extent, the data acquisition path and the residual error on the alignment of the PMMS in relation to the TLS.

Finally, regarding the robust analysis, it can be noted that a slight overestimation of the dispersion values for the Gaussian assessment in relation to the NMAD. In relation to the robust dispersion parameters, NMAD and the square root of BWMV present compatible values. The robust confidence interval provides information related to the asymmetry of the discrepancy sample. When the non-normality is very pronounced (e.g., kurtosis > 10) the Gaussian-derived confidence interval tend to be overestimated. The comparison with the robust interval, for the present study case, reach difference up to 10 mm for the water return pipe 3 (roof).

5. Conclusions

A quantitative and qualitative comparison between the results obtained using a novel PMMS (Zeb-Revo) and the results obtained with a TLS (Faro) for inspection tasks in thermal and

fluid-mechanical facilities is provided. Point clouds gathered from both devices were aligned in the same coordinate system using a network of spheres. Segmentation of objects of interest (walls, roofs, floors, and pipes) was implemented to fit ideal geometries useful for the extraction of important features of the facility, as cylinder (pipes) and planes (walls and roof) that allow to extract different features of interest. The different results obtained with the two sensors were compared applying a robust statistical analysis to evaluate the real potential of the PMMS. Additionally, different specific devices of interest—such as valves, regulation systems, tanks, or burners—were segmented from the two datasets to qualitatively show the level of detail which allows Zeb-Revo in comparison with Faro. Globally, the PMMS performance is inside the technical specification provided by the manufacturer, as it is shown by other studies [22].

The deviation in the estimation of the diameter in the analyzed pipes using Zeb-Revo (with respect to the dataset obtained with Faro) is between 9 and 16 mm when a RANSAC fitting methodology is applied. This deviation could be acceptable for inspection tasks of industrial facilities such as the one proposed in [4]. This deviation in relative terms is higher for pipes with smaller diameter (21.55% in an 8 cm pipe), whereas this relative deviation is better for pipes with higher diameter (3.23% and 4.8% in a 28 cm pipe), always remaining around the centimetric precision given by the Zeb-Revo manufacturer.

A robust statistical analysis was applied to compare the deviation of the discrete points acquired from Zeb-Revo with respect the ideal cylinder fitted from Faro. This analysis shows acceptable results of bias and dispersion (NMAD between 6.5 and 14.5 mm), but for those cylinders of smaller diameter, a bias is detected (7.5–8 mm). This bias could be the main cause of the high percentage deviation in the diameter measurement of those pipes and the origin is not completely explained (pipe curvature, surface finish, etc.) as stated in the discussion section.

The studied planes fitted from points for each dataset show geometrical similitude. This is evaluated through the angle between the normal vector of the plane generated from Zeb-Revo and the one generated with Faro. The misaligned angle analysis allowed to identify an angular discrepancy for the wall planes, whereas in the case of the floor plane, the value 1.3 mrad can be considered a very good result. However, while the dispersion results studied with NMAD, square root of BWMV and IPR are suitable for the three planes (NMAD between 5.9 and 7.4 mm), a significant bias is detected in vertical planes (median −27.2 and −12.8 mm).

Finally, the extraction and qualitative analysis of the specific in-detail elements from the two datasets shows the differences in terms of resolution between them. The identification of element is obviously more evident using TLS (also considering the color registration, which is an added value for the definition of these elements). However, the completeness of the PMMS point cloud can be even higher than the dataset obtained from TLS, allowing for visual identification of elements commonly used in the facilities, such as cutting valves, pressure regulation systems, and burner systems.

Future works will address the improvement of the processes of alignment that allows to obtain an answer to the problem of the bias.

Author Contributions: Conceptualization, M.R.-M. and P.R.-G.; Methodology, M.R.-M. and P.R.-G.; Data acquisition, M.R.-M. and P.R.-G.; Validation, M.R.-M., P.R.-G., and E.R.d.O.C.; Formal analysis, M.R.-M. and P.R.-G.; Resources, D.G.-A.; Writing—original draft preparation, M.R.-M., P.R.-G., E.R.d.O.C., and D.G.-A.; Writing—review and editing, M.R.-M., P.R.-G., and D.G.-A.

Conflicts of Interest: The authors declare no conflict of interest.

References

1. Gonzalez-Aguilera, D.; Del Pozo, S.; Lopez, G.; Rodriguez-Gonzalvez, P. From point cloud to CAD models: Laser and optics geotechnology for the design of electrical substations. *Opt. Laser Technol.* **2012**, *44*, 1384–1392. [CrossRef]
2. Rodríguez-Gonzálvez, P.; Gonzalez-Aguilera, D.; Lopez-Jimenez, G.; Picon-Cabrera, I. Image-based modeling of built environment from an unmanned aerial system. *Autom. Constr.* **2014**, *48*, 44–52. [CrossRef]

3.   Caldwell, R. Hull inspection techniques and strategy-remote inspection developments. In Proceedings of the SPE Offshore Europe Conference & Exhibition, Aberdeen, UK, 5–8 September 2017.

4.   Rodríguez-Martín, M.; Rodríguez-González, P.; Gonzalez-Aguilera, D.; Nocerino, E. Novel Approach for Three-Dimensional Integral Documentation of Machine Rooms in Hospitals Using Portable Mobile Mapping System. *IEEE Access* **2018**, *6*, 79200–79210. [CrossRef]

5.   Hullo, J.F.; Thibault, G.; Boucheny, C.; Dory, F.; Mas, A. Multi-Sensor As-Built Models of Complex Industrial Architectures. *Remote Sens.* **2015**, *7*, 16339–16362. [CrossRef]

6.   Pătrăucean, V.; Armeni, I.; Nahangi, M.; Yeung, J.; Brilakis, I.; Haas, C. State of research in automatic as-built modeling. *Adv. Eng. Inform.* **2015**, *29*, 162–171. [CrossRef]

7.   Quattrini, R.; Malinverni, E.S.; Clini, P.; Nespeca, R.; Orlietti, E. From TLS to HBIM. High quality semantically-aware 3d modeling of complex architecture. *Int. Arch. Photogramm. Remote Sens. Spat. Inf. Sci.* **2015**, 367–374. [CrossRef]

8.   Rodríguez-Martín, M.; Rodríguez-González, P.; Lagüela, S.; González-Aguilera, D. Macro-photogrammetry as a tool for the accurate measurement of three-dimensional misalignment in welding. *Autom. Constr.* **2016**, *71*, 189–197. [CrossRef]

9.   Rodríguez-González, P.; Rodríguez-Martín, M.; Ramos, L.F.; González-Aguilera, D. 3D reconstruction methods and quality assessment for visual inspection of welds. *Autom. Constr.* **2017**, *79*, 49–58. [CrossRef]

10.   Muhammad, J.; Altun, H.; Abo-Serie, E. Welding seam profiling techniques based on active vision sensing for intelligent robotic welding. *Int. J. Adv. Manuf. Technol.* **2017**, *88*, 127–145. [CrossRef]

11.   Shah, H.N.M.; Sulaiman, M.; Shukor, A.Z.; Kamis, Z.; Rahman, A.A. Butt welding joints recognition and location identification by using local thresholding. *Robot. Comput. Integr. Manuf.* **2018**, *51*, 181–188. [CrossRef]

12.   Nocerino, E.; Rodríguez-González, P.; Menna, F. Introduction to mobile mapping with portable systems. In *Laser Scanning: An Emerging Technology in Structural Engineering*; CRC Press: Boca Raton, FL, USA, 2019; pp. 37–52.

13.   Nocerino, E.; Menna, F.; Toschi, I.; Morabito, D.; Remondino, F.; Rodríguez-González, P. Valorisation of history and landscape for promoting the memory of WWI. *J. Cult. Herit.* **2017**, *29*, 113–122. [CrossRef]

14.   Russhakim, N.A.S.; Ariff, M.F.M.; Majid, Z.; Idris, K.M.; Darwin, N.; Abbas, M.A.; Zainuddin, K.; Yusoff, A.R. The Suitability of Terrestrial Laser Scanning for Building Survey and Mapping Applications. *Int. Arch. Photogramm. Remote Sens. Spat. Inf. Sci.* **2019**, *42*, 663–670. [CrossRef]

15.   Nikoohemat, S.; Peter, M.; Oude Elberink, S.; Vosselman, G. Exploiting indoor mobile laser scanner trajectories for semantic interpretation of point clouds. *ISPRS Ann. Photogramm. Remote Sens. Spat. Inf. Sci.* **2017**, *2017*, 355–362. [CrossRef]

16.   Rodríguez-González, P.; Nocerino, E. Portable Mobile Mapping Systems applied to the Management of Natural Spaces. In *New Developments in Agricultural Research*; Nova Science Publishers: New York, NY, USA, 2019; pp. 1–43.

17.   GeoSlam Zeb-Revo. Available online: https://geoslam.com/solutions/zeb-revo/ (accessed on 13 September 2019).

18.   Chiabrando, F.; Coletta, C.D.; Sammartano, G.; Spanò, A.; Spreafico, A. "Torino 1911" project: A contribution of a slam-based survey to extensive 3D heritage modeling. *Int. Arch. Photogramm. Remote Sens. Spat. Inf. Sci.* **2018**, 225–234. [CrossRef]

19.   Dewez, T.J.B.; Yart, S.; Thuon, Y.; Pannet, P.; Plat, E. Towards cavity-collapse hazard maps with Zeb-Revo handheld laser scanner point clouds. *Photogramm. Rec.* **2017**, *32*, 354–376. [CrossRef]

20.   Masiero, A.; Fissore, F.; Guarnieri, A.; Pirotti, F.; Visintini, D.; Vettore, A. Performance Evaluation of Two Indoor Mapping Systems: Low-Cost UWB-Aided Photogrammetry and Backpack Laser Scanning. *Appl. Sci.* **2018**, *8*, 416. [CrossRef]

21.   Chiabrando, F.; Sammartano, G.; Spanò, A. A comparison among different optimization levels in 3D multi-sensor models. A test case in emergency context: 2016 Italian earthquake. *Int. Arch. Photogramm. Remote Sens. Spat. Inf. Sci.* **2017**, 155–162. [CrossRef]

22.   Nocerino, E.; Menna, F.; Remondino, F.; Toschi, I.; Rodríguez-González, P. Investigation of indoor and outdoor performance of two portable mobile mapping systems. *Proc. SPIE* **2017**, *10332*. [CrossRef]

23.   Tucci, G.; Visintini, D.; Bonora, V.; Parisi, E. Examination of Indoor Mobile Mapping Systems in a Diversified Internal/External Test Field. *Appl. Sci.* **2018**, *8*, 401. [CrossRef]

24. AENOR (Spanish Association for Standardisation). Machine Rooms and Gas Fired Self-Contained Apparatus for Heating or Cooling Generation or Cogeneration, Standard UNE 60601:2013. Available online: https://www.aenor.com/normas-y-libros/buscador-de-normas/une/?c=N0052265 (accessed on 12 November 2014).

25. BOE (Official State Gazette of the Government of Spain). *Real Decreto 2060/2008, de 12 de Diciembre, Por el Que se Aprueba el Reglamento de Equipos a Presión y Sus Instrucciones Técnicas Complementarias*; Ministerio de Industria, Turismo y Comercio: Madrid, Spain, 2009; pp. 12297–12388.

26. BOE (Official State Gazette of the Government of Spain). *Real Decreto 1027/2007, de 20 de Julio, Por el Que se Aprueba el Reglamento de Instalaciones Térmicas en Los Edificios*; Ministerio de la Presidencia: Madrid, Spain, 2007; pp. 35931–35984.

27. Bosse, M.; Zlot, R.; Flick, P. Zebedee: Design of a Spring-Mounted 3-D Range Sensor with Application to Mobile Mapping. *IEEE Trans. Robot.* **2012**, *28*, 1104–1119. [CrossRef]

28. Eyre, M.; Wetherelt, A.; Coggan, J. Evaluation of automated underground mapping solutions for mining and civil engineering applications. *J. Appl. Remote Sens.* **2016**, *10*, 20–39. [CrossRef]

29. Cabo, C.; Del Pozo, S.; Rodríguez-González, P.; Ordóñez, C.; González-Aguilera, D. Comparing Terrestrial Laser Scanning (TLS) and Wearable Laser Scanning (WLS) for Individual Tree Modeling at Plot Level. *Remote Sens.* **2018**, *10*, 540. [CrossRef]

30. Besl, P.; McKay, M. A method for registration of 3-D shapes. *IEEE Trans. Pattern Anal. Mach. Intell.* **1992**, *14*, 239–256. [CrossRef]

31. Wujanz, D.; Barazzetti, L.; Previtali, M.; Scaioni, M. A Comparative Study among Three Registration Algorithms: Performance, Quality Assurance and Accuracy. *Int. Arch. Photogramm. Remote Sens. Spat. Inf. Sci.* **2019**, 779–786. [CrossRef]

32. Schnabel, R.; Wahl, R.; Klein, R. Efficient RANSAC for Point-Cloud Shape Detection. *Comput. Graph. Forum* **2007**, *26*, 214–226. [CrossRef]

33. Cloud Compare. GPL Software (Version 2.9.1). Available online: www.danielgm.net/cc/ (accessed on 7 August 2019).

34. Rodríguez-Martín, M.; Rodríguez-González, P.; Gonzalez-Aguilera, D.; Fernandez-Hernandez, J. Feasibility study of a structured light system applied to welding inspection based on articulated coordinate measure machine data. *IEEE Sens. J.* **2017**, *17*, 4217–4224. [CrossRef]

35. Rodríguez-González, P.; Rodríguez-Martín, M. Weld Bead Detection Based on 3D Geometric Features and Machine Learning Approaches. *IEEE Access* **2019**, *7*, 14714–14727. [CrossRef]

36. Höhle, J.; Höhle, M. Accuracy assessment of digital elevation models by means of robust statistical method. *ISPRS J. Photogramm. Remote Sens.* **2009**, *64*, 398–406. [CrossRef]

37. Hasan, A.; Pilesjö, P.; Persson, A. The use of LIDAR as a data source for digital elevation models–a study of the relationship between the accuracy of digital elevation models and topographical attributes in northern peatlands. *Hydrol. Earth Syst. Sci. Discuss.* **2011**, *8*, 5497–5522. [CrossRef]

38. Rodríguez-González, P.; Garcia-Gago, J.; Gomez-Lahoz, J.; González-Aguilera, D. Confronting Passive and Active Sensors with Non-Gaussian Statistics. *Sensors* **2014**, *14*, 13759–13777. [CrossRef]

39. Herrero-Huerta, M.; Lindenbergh, R.; Rodríguez-González, P. Automatic tree parameter extraction by a Mobile LiDAR System in an urban context. *PLoS ONE* **2018**, *13*, e0196004. [CrossRef] [PubMed]

Capítulo 4

Mantenimiento de plantas fotovoltaicas mediante fotogrametría

Capítulo 4

Mantenimiento de plantas fotovoltaicas mediante fotogrametría

En este capítulo se incluye el artículo *"SunMap: Towards Unattended Maintenance of Photovoltaic Plants Using Drone Photogrammetry"* publicado en la revista *Drones* en febrero de 2023.

4.1. Resumen

Las energías renovables están experimentado un crecimiento constante en los últimos años, debido a las necesidades de cumplimiento de los requisitos del Protocolo de Kioto y los acuerdos internacionales posteriores, pero también a la presión debida a una mayor concienciación de la ciudadanía en la lucha contra el cambio climático. En el caso concreto de las plantas fotovoltaicas, el crecimiento masivo de las mismas, tanto en número como en tamaño, ha motivado la necesidad del desarrollo de nuevos enfoques para su inspección y monitorización.

La solución presentada en este artículo, materializada en el *software* SunMap (descrito en el apéndice B.5), se basa en el uso de imágenes visibles y termográficas capturadas con drones para realizar las inspecciones periódicas de forma desatendida, mediante un tratamiento fotogramétrico riguroso de las imágenes y la detección automática de las patologías conocidas como puntos calientes (*hotspots*). Este tipo de patología consiste en un aumento de temperatura en un punto de un panel y se produce cuando una o varias células fotovoltaicas presentan una corriente de cortocircuito mucho menor que el resto de las células del módulo, lo que provoca una pérdida de potencia entre un 2 y un 20 %.

Existen bastantes precedentes en el uso de termografía para la detección de patologías en paneles solares, si bien estas soluciones existentes presentan un enfoque

semiautomático que requieren de una importante interacción del usuario. En Sun-Map se realiza una automatización del proceso de detección de puntos calientes. La herramienta parte de un tratamiento fotogramétrico riguroso de las imágenes RGB y termográficas que garantiza la georreferencia precisa de los productos cartográficos generados.

La corrección de temperaturas en las imágenes consiste en una corrección de distancia respecto del centro de proyección, la corrección del ángulo de incidencia para la obtención de la emisividad, la corrección de reflexión y la corrección atmosférica.

La detección de puntos calientes se basa en la estimación de gradientes de temperatura, en lugar de trabajar con las temperaturas absolutas, empleando estimadores robustos y trabajando a dos niveles distintos, para todo el conjunto de imágenes y para las imágenes correspondientes a un panel determinado. La búsqueda de puntos calientes emplea las mejores imágenes (en función de criterios geométricos) para cada panel, lo cual permite robustecer el proceso ya que para que un punto caliente detectado se considere como valido debe aparecer en un mínimo de 3 imágenes. Igualmente, se debe cumplir la condición de que la temperatura relativa supere un umbral respecto a los píxeles vecinos.

Article

SunMap: Towards Unattended Maintenance of Photovoltaic Plants Using Drone Photogrammetry

David Hernández-López [1], Esteban Ruíz de Oña [2], Miguel A. Moreno [1] and Diego González-Aguilera [2,*]

1   Institute for Regional Development, University of Castilla la Mancha, Campus Universitario s/n, 02071 Albacete, Spain
2   Department of Cartographic and Land Engineering, Higher Polytechnic School of Avila, University of Salamanca, Hornos Caleros 50, 05003 Avila, Spain
*   Correspondence: daguilera@usal.es; Tel.: +34-920-353-500

Abstract: Global awareness of environmental issues has boosted interest in renewable energy resources, among which solar energy is one of the most attractive renewable sources. The massive growth of PV plants, both in number and size, has motivated the development of new approaches for their inspection and monitoring. In this paper, a rigorous drone photogrammetry approach using optical Red, Green and Blue (RGB) and Infrared Thermography (IRT) images is applied to detect one of the most common faults (hot spots) in photovoltaic (PV) plants. The latest advances in photogrammetry and computer vision (i.e., Structure from Motion (SfM) and multiview stereo (MVS)), together with advanced and robust analysis of IRT images, are the main elements of the proposed methodology. We developed an in-house software application, SunMap, that allows automatic, accurate, and reliable detection of hot spots on PV panels. Along with the identification and geolocation of malfunctioning PV panels, SunMap provides high-quality cartographic products by means of 3D models and true orthophotos that provide additional support for maintenance operations. Validation of SunMap was performed in two different PV plants located in Spain, generating positive results in the detection and geolocation of anomalies with an error incidence lower than 15% as validated by the manufacturer's standard electrical tests.

Keywords: photovoltaic plants; unattended maintenance; photogrammetry; thermography; drones; hot spots; software development

1. Introduction

1.1. Motivation

Conventional electricity grids are based on management principles and technologies developed for a centralized generation system. This involves the large-scale generation of electricity at centralized facilities using a distribution network optimized for supply reliability. These classical network solutions, however, fail to meet growing demand, end users' expectations, and the need for data security and reliability, among other requirements. Due to the requirements of the Kyoto Protocol and subsequent international agreements (Paris COP21, Glasgow COP26), which focused on reducing greenhouse gas emissions, the transition to renewable energies based on decentralized energy systems and the implementation of energy efficiency are mandatory [1]. To this end, management tools at all levels must change towards more intelligent systems that incorporate automatic exploitation of increasingly abundant information and new operation and maintenance models based on renewable energies and are adapted to new technological elements that are available at lower cost.

With the proliferation of drones [2] and artificial intelligence [3], as well as with the development of sensors combined with image processing capabilities [4], the range of possibilities for driving this transformation towards the intelligent inspection and management of renewable energy generation plants (e.g., solar, wind, hydroelectric, etc.) is

broad. These critical infrastructures require periodic inspection to ensure their effective and efficient operation, but these facilities are sometimes difficult to access, and thus inspection can be dangerous for the operator. Therefore, unattended maintenance through the use of robotic techniques (i.e., drones) and non-invasive sensors (e.g., cameras, LiDAR, etc.) is most cost-effective [5]. To this end, recent years have seen the development of an official standard (IEC TS 62446-3) for the testing, documentation, and maintenance of PV modules and plants using drones and infrared thermography [6]. In the case of photovoltaic (PV) plants, adequate inspection of PV installations requires the acquisition of different types of data, from geometric data that allow a dimensional analysis of the facility and its assets (e.g., the distance between PV panels and vegetation, the height of vegetation, etc.), to radiometric data (i.e., multispectral imagery) that allow advanced analysis of the images for the automatic identification of faults in PV panels. This inspection is enhanced by the use of multiple spectral bands, mainly near, medium and thermal infrared, since they allow the identification of faults that are not perceived visually, such as defects in non-operative cells, discoloration, oxidation/corrosion, etc. [7]. Nevertheless, integrated interpretation of all the data acquired during the inspection requires the precise detection of each fault, as well as the identification and quantification of the type and severity of the fault. Therefore, it is clear that the development of tools that allow monitoring, diagnosing, and even forecasting these faults in PV plants is necessary in order to improve efficiency during their complete lifecycle, and these tools will provide important economic and ecological benefits [8].

Advancing the automation of faults in PV plants entails a series of difficulties [9]: (i) the automatic extraction and semantic recognition of the PV panels and their elements based on imagery (i.e., arrays, panels, modules and cells); (ii) the incidence of false positives due to detection of the same fault in different images; (iii) the incidence of false positives outside the PV panels; (iv) problems associated with reflections at the edges of PV panels; and (v) the precise geolocation of faults in the PV panels.

1.2. Literature Review

Although there are several approaches in the scientific community to dealing with PV faults based on imagery [10,11], most of them are semi-automatic or time-consuming, so their monitoring and management still require manual user interaction. According to [10,11] and their reviews, although there are many algorithms and hardware tools available, the remote and online monitoring of PV plants is still at a low technology-readiness level (i.e., prototyping stage). This suggests the need for development of cutting-edge intelligent systems that can overcome the current challenges. The key seems to be related to the exploitation of multi-modal imagery (e.g., optical RGB, IRT, ultraviolet fluorescence (UVF) imaging, etc.) and aerial drones that can enhance the detection and classification of faults in PV panels. Of course, intelligent and automatic approaches for interpreting these images remain crucial. In [12], the authors test and use different types of aerial platforms combined with visible and IRT cameras for detecting faults in PV panels, but they do not provide any automatic approach for its detection. In [13], the authors perform an exhaustive thermographic analysis of three different types of faults in PV panels, but all the tests are carried out in the laboratory. In [14], the authors advance an automatic solution for detecting some faults in PV panels, but the thermographic analysis of images is not rigorous, and they do not provide automatic extraction of geometries. In an attempt to advance the vectorization of PV faults, [15] presents advances in an automatic solution for detecting some faults in PV panels through image processing and Canny edge detection. However, the thermographic analysis of images is performed in the laboratory. More recently, [16] develops a method to recognize hot spots in photovoltaic modules using IRT images and an image processing technique based on the Otsu thresholding method. The average accuracy in hot spot detection is very high, but they provide only the initial experiments of an ongoing research project. Although other authors [17] deal with image analysis for detection PV panels and their structure, they do not generate cartographic products to provide a 3D analysis of the PV plants. In [18], the authors analyse IRT images

using the Laplace operator, but again all the analyses are performed in an experimental setup. More recent approaches have been centered around the structure and management of the information of PV plants using Geographical Information Systems (GIS). In [19], the authors provide structured and rigorous information for a PV plant, and in particular, define a conceptual model based on a relational database for the intelligent management of PV plants; however, automatic routines for the extraction of elements and the detection of faults are not included in this approach. Using the same GIS background applied to the management and computation of PV potential, [20] develops a WebGIS tool for the automatic computation of PV potential on rooftops. While these are important advances in the field, automated analysis of images for tasks such as the extraction of roof intersections is still to be developed.

Other recent approaches deal with artificial intelligence [21,22], but require data preparation and augmentation together with model training. In [22], the authors propose a new intelligent PV panel monitoring and fault diagnosis technique using a neural network and a classifier in combination. Unfortunately, they do not adapt a method for use with drones. It is clear that the use of aerial drones based on optical RGB and IRT images constitutes the most efficient way to detect faults, and thus minimize operation and maintenance costs in PV plants [8]. These approaches require rigorous photogrammetric image analysis and thermographic procedures in order to guarantee accurate and timely responses during the detection of faults in PV plants.

To this end, SunMap is presented in this paper based on a series of developments with a similar thread, "from imagery to smart 3D models", that have been applied successfully in other fields (e.g., industry 4.0 and remote sensing) [23,24]. SunMap provides rigorous photogrammetric and thermographic treatment of images acquired from aerial drones based on the generation of high-quality cartographic products and expert reports containing the precise geolocation of hot spots. The automatic and reliable detection of hot spots in PV panels is based on two conditions: (i) the presence of a hot spot in at least three thermographic images; and (ii) the existence of a thermographic gradient above 10 °C with respect to the hot spot's neighbours.

SunMap presents the following advantages compared to the similar approaches described above: (i) a rigorous and automatic photogrammetric processing exploiting multiview geometry; (ii) the generation of high-quality cartographic products that integrate visible and thermographic information; (iii) the automatic detection of PV arrays and PV panels based on advanced imagery analysis; (iv) rigorous correction and analysis of thermographic images; (v) robust statistical detection of hot spots integrated with the generation of expert reports based on the official standard IEC TS 62446-3 [6].

This manuscript is structured as follows: Section 2 describes the methodology developed and encoded within the SunMap software; Section 3 validates the software using two different PV plants as pilot cases; and a final section is devoted to outlining conclusions and future research.

2. Methodology

Figure 1 outlines the process codified in the SunMap tool for the detection of hot spots in PV plants using drone photogrammetry. A hot spot fault is a heating effect that exists when at least one PV cell presents a short-circuited current that is much lower than the rest of the cells in the module. This pathology happens when the PV cell is totally or partially fractured or electrically mismatched, resulting in power loss of 2–20% [25]. In Figure 1, the pipeline starts with data acquisition from aerial drones using RGB and IRT images. A photogrammetric and computer vision approach is then applied to perform self-calibration and orientation of the images with the Structure from Motion (SfM) technique and to generate a dense point cloud based on the multiview stereo (MVS) technique. Different cartographic products in 2D (true orthophoto) and 3D (digital terrain and surface models, DTM/DSM) are then obtained to support the detection of hot spots. In particular, a robust analysis of the IRT images is performed to detect hot spots. As a result, the end user can

assess the current state of the PV plant regarding hot spots and obtain an expert report with the geolocation of these pathologies on the true orthoimage. Auxiliary PV plant data (e.g., plans, technical specifications of PV panels, etc.) can be added to complete the expert report.
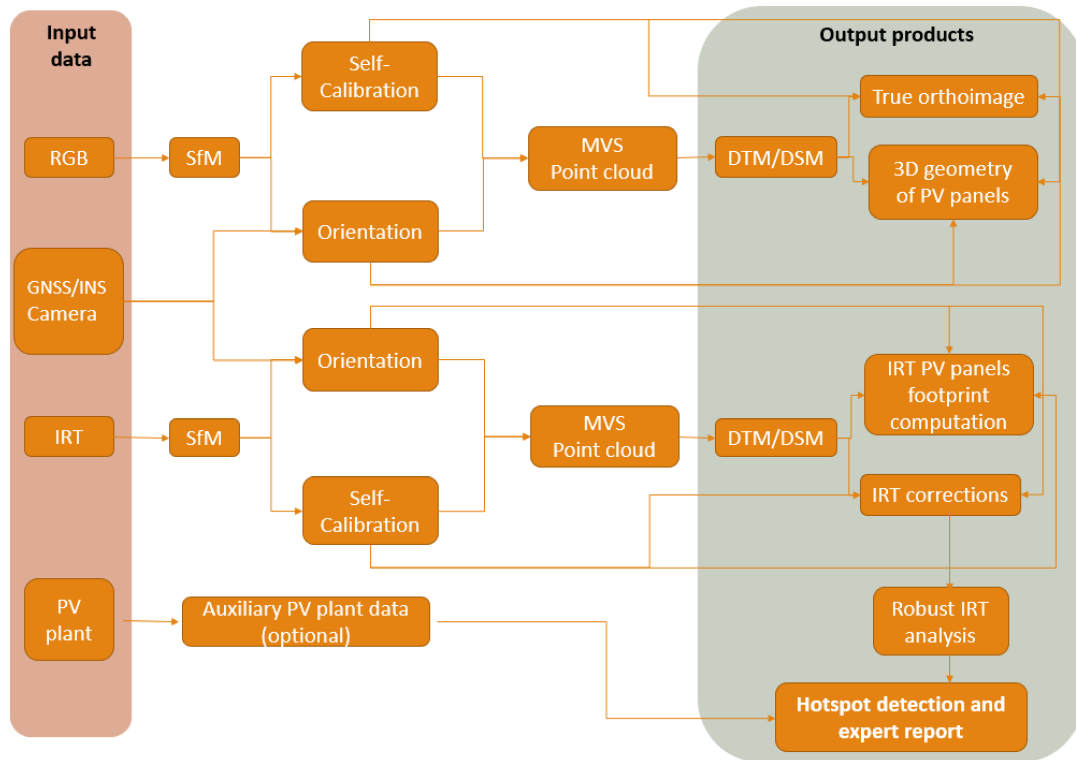
Figure 1. Workflow scheme of the method developed and encoded in SunMap. SfM refers to Structure from Motion for providing self-calibration and orientation of images. MVS refers to the multiview stereo technique for generating dense point clouds. DTM and DSM refer to digital terrain and surface models, respectively.

2.1. Photogrammetric Processing of Visible and Thermographic Images

An automatic photogrammetric pipeline was implemented considering the following input data: (i) images acquired from an aerial drone with an optical Red, Green and Blue (RGB) camera and an infrared thermographic (IRT) camera, capable of acquiring RGB and IRT images simultaneously or acquiring RGB and IRT images in separate flights; and (ii) the positions and orientations of images coming from the global navigation satellite system (GNSS) and the inertial navigation unit (IMU), in a CVS or TXT file. Note that GNSS positions should be provided with real-time kinematic (RTK) or Post Processed Kinematics (PPK) methods [26] so that direct orientation of the RGB and IRT images can be obtained. In this case, the fieldwork of measuring ground control points with GNSS or other topographic methods is not needed, greatly reducing data acquisition and processing costs.

The photogrammetric pipeline is integrated with a routine developed by the authors [4] based on the Structure from Motion (SfM) technique, providing a means of determining the orientation and relative positions of the cameras, and in turn performing self-calibration of the cameras (RGB and IRT). The photogrammetric approach allows for the generation of a dense point cloud using the multiview stereo (MVS) technique [27].

The first photogrammetric step comprises extraction and matching of points of interest. For the extraction, the SIFT (Scale-Invariant Feature Transform) [28] detector/descriptor algorithm is used, more specifically the SiftGPU library, which is an implementation of the SIFT algorithm for CUDA-compatible systems [29]. For matching, the FLANN technique (Fast Library for Approximate Nearest Neighbors) is used with a robust matching strategy [30]. This robust correspondence strategy consists of performing a series of tests to filter out erroneous correspondences. Specifically, the ratio test, the crossed matching, and the geometric tests are used together with determination of the fundamental, homography, and essential matrices by means of an adjustment with a Random Sample Consensus (RANSAC) algorithm [31].

Image-based 3D reconstruction is then performed incrementally through an iterative process consisting of relative image orientation, triangulation, and bundle adjustment [32].

Finally, the relative photogrammetric exterior orientations are transformed into an official coordinate reference system (CRS). In this study we use the official CRS in Spain, integrating the following CRSs: EPSG: 25830, datum ETRS89 and coordinate system UTM zone 30; and EPSG:5782, datum Alicante and orthometric heights.

2.2. Cartographic Products Generation

Once the photogrammetry corresponding to the two cameras (RGB and IRT) is solved, the generation of cartographic products is performed in the form of digital terrain models (DTM), digital surface models (DSM), and true orthoimages, which are processed using a DSM instead of a DTM, which yields a vertical view of the PV plant, eliminating panel tilting and allowing a view of nearly any point on the ground. The DSM is used to remove relief displacement of the PV panels from the acquired images. These true orthoimages are used as input for assessing the presence of possible faults (i.e., hot spots) in the PV panels.

The first step is to separate the terrain from the panels to ensure better quality in DSM generation. For this, a terrain-extraction algorithm based on the Cloud Simulation Filter (CSF) is applied [33]. By applying this algorithm, a point cloud with the terrain and another point cloud with the panels are obtained. Using the inverse distance interpolation method based on nearest-neighbour search [34], DTMs are generated for both the terrain and the panels and later merged to generate the DSM. The reason for separating the DTMs and then merging in a DSM is that the different classes corresponding with PV panels and terrain can have different *Z* coordinates for the same *X,Y* coordinates, allowing orthorectification of the terrain and the PV panels and generation of the true orthoimage.

The second step is the generation of the true orthoimage (Figure 2) based on the previous DSM, which contains the height of the PV panels and thus allows precise geolocation of the hot spots. More specifically, the process of generating true orthoimages consists of the following steps: (i) definition of the flight path; (ii) determination of hidden areas in the images through the Z-buffer algorithm using the DSM [35]; (iii) correction of image distortion using the inner camera parameters from the self-calibration; (iv) orthoimage generation; and (v) completion of the hidden areas.

The final step is to generate a final true orthoimage mosaic corresponding to the whole PV plant. The photogrammetric process of ortho-projection basically consists of generating an orthogonal projection, thus representing three-dimensional objects (terrain and PV panels) in two dimensions without the perspective of the original image, which is a central projection. This process is achieved by a two-dimensional transformation between the original image and the corrected image (orthoimage), which is already georeferenced in the projection plane. To carry out the processing of the orthoimage, the inverse method [36] is used. In this case, an image with known internal and external orientation is needed, as well as the DSM of the PV plant. Subsequently, the size of the orthoimage (resolution) is defined according to the size of the pixel in ground units.
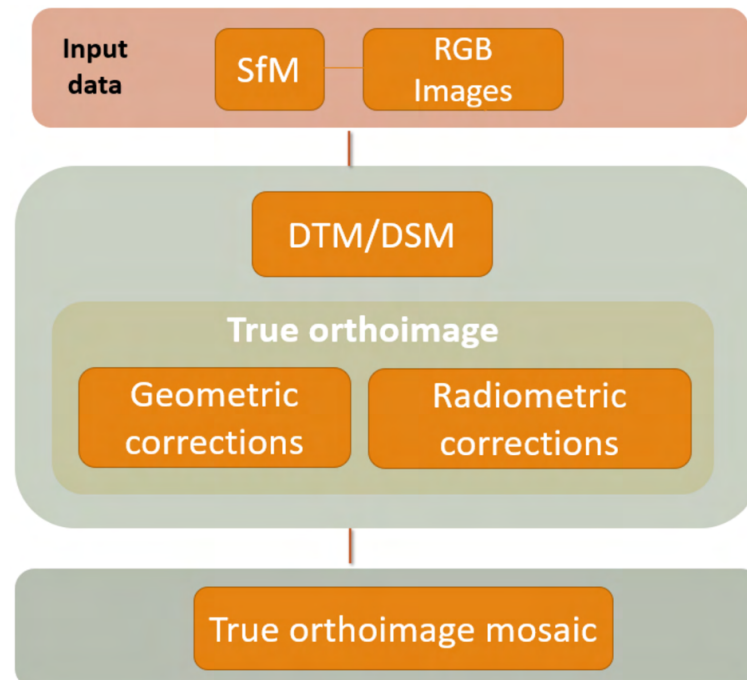
Figure 2. True orthoimage scheme developed and encoded in SunMap.

2.3. Extraction and Detection of the 3D Geometry of PV Panels

It should be noted that the inputs of this image analysis approach are the DSM and the true orthoimage generated from the photogrammetric process, since they enclose the metric properties and the adequate geometric resolution to apply the process with quality, and thus provide a better geolocation of the hot spots.

Prior to extraction and detection of the 3D geometry of the PV panels, a conceptual model based on the geometry and semantics of the PV plant needs to be defined (Figure 3). To this end, a coarse-to-fine approach is used for the extraction and detection of the 3D geometry of PV panels, so that starting from the extraction of PV arrays, the detection of PV panels, PV modules, and even PV cells can be obtained. The term "array" is used to refer to a set of PV panels arranged in rows and columns. In turn, each of these PV panels is made up of modules, which are each made up of an array of PV cells, also distributed in rows and columns.

The definition of the geometry and semantics of the PV plant, as well as the area of interest, is specified in a set of files in shapefile format that are created automatically through the development of algorithms supported by image analysis techniques (i.e., filtering) and feature extraction (i.e., contours and lines). This procedure is performed as follows: (i) first, filtering of the orthoimage is performed to remove noise, followed by a search for contours applying different thresholding of the images [37]; (ii) second, the contours obtained are simplified using the Douglas–Peucker line simplification algorithm [38]; and (iii) very small contours are eliminated, and contours with four vertices and whose angles are close to 90° are retained. For all contours, the median of their area is calculated and the panels that are not within the tolerance sought are eliminated. Finally, to determine the contours of the rows of panels, (iv) the modules are clustered using a density-based spatial clustering algorithm (DBSCAN) [39].
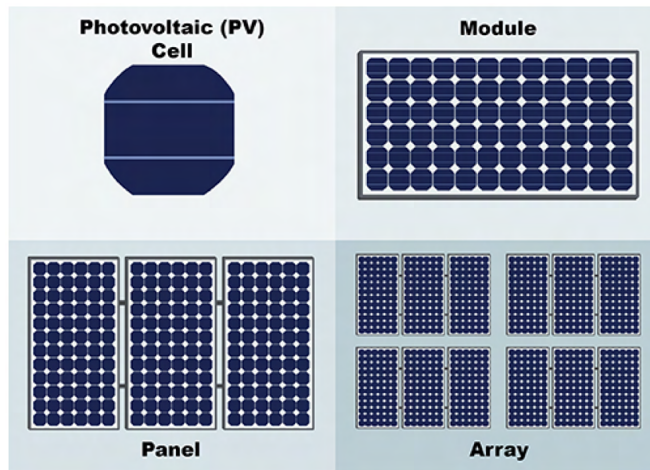
Figure 3. Schema of the different levels of discretization of the PV panels under study.

2.4. Correction of Thermographic Images

Good analysis of IRT images entails understanding the physics behind the IRT images and correcting the IRT images obtained. Information about the weather, the atmosphere, the object analysed (i.e., PV panels) and its environment is essential.

Before proceeding to calculate temperature statistics and to detect hot spots, it is necessary to apply a series of corrections to the thermographic images. This process is fully automatic and is based on the application of the following corrections: (i) distance correction, which contains the distance for each visible pixel from the center of projection of the camera to the point over the panel; (ii) incidence angle correction for obtaining emissivity, computed using the angle formed by the line of observation with the normal to the 3D surface of the PV panel for each visible pixel; (iii) reflection correction, which is based on isolating the areas of the PV arrays that may have problems caused by reflections from other panel arrays (Figure 4); and (iv) atmospheric correction, which includes correction for temperature and relative humidity of the study area.
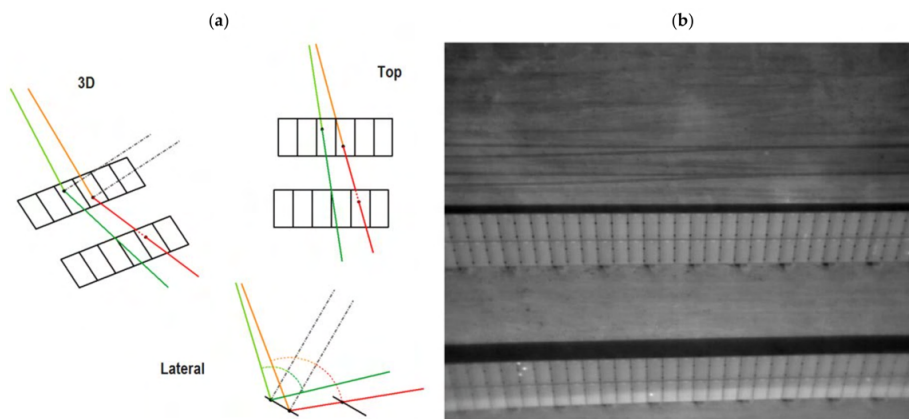
Figure 4. Reflection correction in thermal imagery: (**a**) 3D ray reflection computation and its possible intersection with other PV panels; (**b**) detected and isolated areas affected by reflections in IRT images. In green colour a reflected 3D ray without intersection with a PV panel. In red colour a reflected 3D ray with intersection with a PV panel.

A reflected 3D ray without intersection with a PV panel **is shown in green**. A reflected 3D ray with intersection with a PV panel is shown in red.

To carry out the atmospheric correction, it is necessary to know the values of temperature (°C) and relative humidity (%) at the time of acquisition [40]. Two options are contemplated in SunMap: (i) only an estimation of an average value is available for the entire drone flight, or (ii) these values can be provided from a meteorological station close to the facilities of the PV plant.

The final atmospheric correction of the thermographic images is synthesized using the following equation (Equation (1)) [6]:

$$T_{obj} = \sqrt[4]{\frac{W_{tot} - (1 - \varepsilon) \cdot \tau \cdot \sigma \cdot T_{refl}^4 - (1 - \tau) \cdot \sigma \cdot T_{atm}^4}{\varepsilon \cdot \tau \cdot \sigma}} \tag{1}$$

where the total radiation (W_{tot}) received by the IRT camera comprises the emission of the object, $\varepsilon \cdot \tau \cdot W_{obj}$, the emission of the surroundings reflected by the object, $(1 - \varepsilon) \cdot \tau \cdot W_{refl}$, and the emission of the atmosphere, $(1 - \tau) \cdot W_{atm}$.

Although there are accurate methodologies for calculating the operating temperature of photovoltaic modules [41], the proper expression depends on the specific mounting geometry. Equation (2) allows for the estimation of the temperature of the PV module from basic data such as ambient temperature, irradiance, and specific parameters of the module such as the Nominal Operating Cell Temperature (NOCT) [6]:

$$T_c = T_a + \left(\frac{G_T}{G_{NOCT}}\right)(T_{NOCT} - T_{a-NOCT}) \tag{2}$$

where Tc is the operating temperature of PV module, G_T is the irradiance, G_{NOCT} is the irradiance at NOCT conditions (800 W/m²), T_{NOCT} is the operating temperature of the PV module at NOCT conditions (45 °C for the analysed module), and T_{a-NOCT} is the ambient temperature at NOCT conditions (20 °C).

2.5. Statistical Analysis of Temperatures

Reliable hot spot detection requires an exhaustive statistical analysis. Therefore, despite applying calibrations to the acquired images and taking into account the corresponding corrections in the previous section, the detection of hot spots is applied based on the estimation of temperature gradients, not their absolute values. To do this, robust statistics (i.e., median and biweight midvariance (*BWMV*)) [42] are applied (Equations (3)–(5)), supported by statistical samples at two different levels: (i) the array level, assessing all the thermographic images that correspond to the PV array; and (ii) the panel level, analysing all the thermographic images that correspond to a given PV panel. Note that the photogrammetric process has been fully solved with both visible and thermographic images, making it possible to unambiguously identify the PV panels and PV arrays in the thermographic images. Again, this process is completely automatic, and the results are outlined in the expert report.

$$BWMV = \frac{n \sum_{i=1}^{n} a_i (x_i - m)^2 (1 - U_i^2)^4}{\left(\sum_{i=1}^{n} a_i (1 - U_i^2)(1 - 5U_i^2)\right)^2} \tag{3}$$

$$U_i = \frac{\mu_i - m}{9MAD} \tag{4}$$

where m is the median, n is the number of points, U is a parameter from Equation (4), μ is the mean and *MAD* is the median absolute deviation, being

$$MAD = median\left(\left|Dif_i - m_{Dif}\right|\right) \tag{5}$$

where *Dif* denotes the temperature gradients and m_{Dif} is the median of the gradients in temperatures. Finally, the value of the parameter *a* (Equation (3)) can be 0 or 1 depending on the *U* value. If $-1 \leq U \leq 1$, $a = 1$, otherwise $a = 0$.

2.6. Hot Spot Detection and Expert Report Generation

Finally, hot spot detection requires an automatic iterative process based on the analysis of panels extracted as described in Section 2.3 and the footprint of the IRT flight (Figure 5). Starting with the PV panel contour coordinates, a search is performed for those thermographic images with less perspective or that are more vertical in relation to the PV panel. As a result, more than one thermographic image can be used for hot spot detection, and thus robust detection can be provided through the calculation of the different temperature gradients (Section 2.5). A hot spot is considered valid if it fulfils at least two conditions: (i) it appears in three thermographic images; and (ii) it exists at a gradient with respect to its neighbours above a threshold, for example, 10 °C [43].
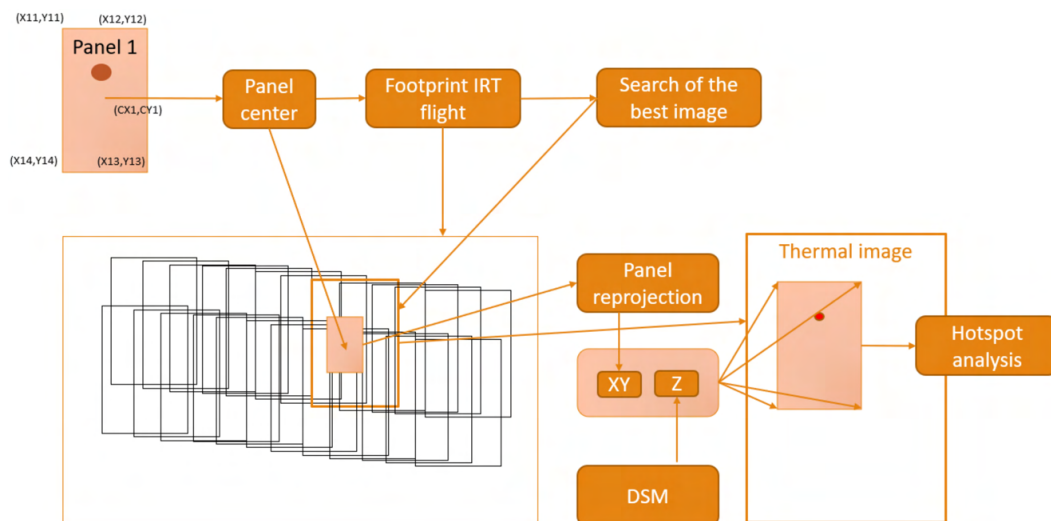
Figure 5. Automatic and iterative hot spot detection process developed in SunMap.

The geolocation of the hot spot in an official CRS is obtained through the photogrammetric resolution of the process detailed in Section 2.1, together with the generation of the expert report.

3. Case Studies

Validation of the SunMap tool was carried out in two PV plants located in the west and east of Spain, in Caceres and Albacete, respectively (Figure 6). Both locations have many hours of sunshine per year (>3000 h), making them ideal locations for this type of renewable energy infrastructure. The PV plant in Caceres (Figure 7a) has a surface of 12.5 ha and contains 156 PV arrays, with power generation of 2.9 MW. The PV plant located in Albacete (Figure 7c) has a surface of 9 ha and contains 77 PV arrays, with power generation of 3 MW. These two cases were selected based on the interest of two different companies in checking and validating the possibilities of the tool for the automatic inspection of PV plants.

Figure 6. Location of the PV plants included in the present research.

(**a**)

(**b**)

(**c**)

(**d**)
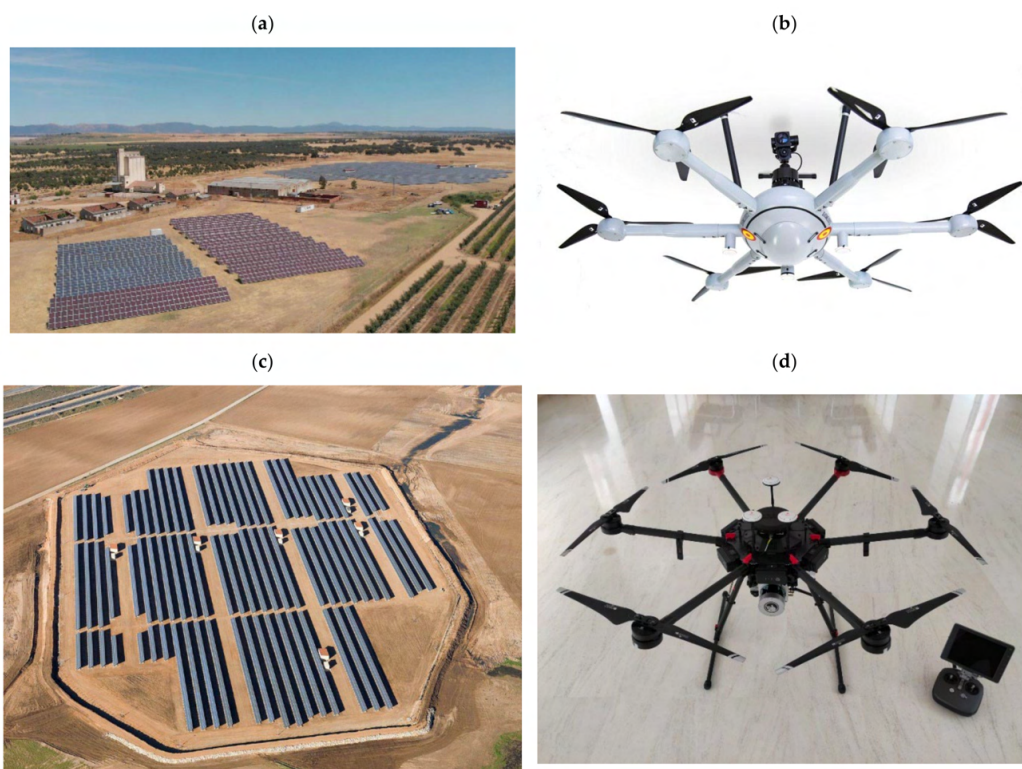
Figure 7. Aerial images acquired from drones of the PV plants used as pilot cases for the validation of the SunMap tool. (**a**) PV plant in Caceres, with an extension of 12.5 ha, 156 PV arrays and power generation of 2.9 MW. (**b**) Aerial drone platform and sensors used in the PV plant at Caceres. (**c**) PV plant located in Albacete with a surface of 9 ha, 77 PV arrays and power generation of 3 MW. (**d**) Aerial drone platform and sensors used in the PV plant at Albacete.

Another important aspect for the validation of the SunMap tool is the use of different types of drones and sensors in each case study (Figure 7b,d). The following table (Table 1) outlines the technical details of the different drone platforms and sensors used.

Table 1. Technical features of the drones and sensors used in the pilot cases.

Drone Platform	Camera Sensors		GNSS/INS Sensors	
	RGB	**IRT**	**GNSS/RTK**	**INS**
RGB–Phantom 4 Thermal–DJI Matrice 600	FC6310R, Resolution: 5472 × 3648 pixels Focal length: 8.8 mm	Flir Duo Pro R Resolution: 640 × 512 pixels Focal length: 13 mm	GPS: L1/L2; GLONASS: L1/L2; Vertical 2.5 cm Horizontal 2 cm	APX-15 RMS ERROR INS: Roll: 0.02 Deg Pitch: 0.02 Deg Heading: 0.15 Deg
Condor	Sony ILCE-6000 Resolution: 6000 × 4000 pixels Focal length: 16 mm	Workswell Wiris Resolution: 640 × 512 pixels Focal length: 13 mm	GPS: L1/L2; GLONASS: L1/L2; BeiDou: B1/B2; Galileo E1/E5a Vertical 1.5 cm Horizontal 1 cm	RMS ERROR INS: Roll: 0.02 Deg Pitch: 0.02 Deg Heading: 0.15 Deg

For the imagery acquisition, different photogrammetric flights were planned and executed using a tool, Mflip, developed by the authors [44]. Special attention was focused on the different characteristics of the RGB and IRT cameras (i.e., resolution, field of view, etc.) so that the PV plants could be recorded with a single flight using both sensors simultaneously.

Regarding navigation, both flights were executed using GNSS/INS hardware and integrated navigation technology, so that the exterior orientation parameters of aerial imagery could be used as initial approximations in the photogrammetric process. This georeferencing method, which is called direct georeferencing, has gained increasing attention in the photogrammetry community because it does not require measuring ground control points, allowing unattended maintenance of PV plants.

4. Results

In this section, the different results obtained at two different PV plants are described and analysed in order to validate the in-house software.

4.1. Photogrammetric Processing of Visible and Thermographic Images

At the PV plant at Caceres, a single flight was executed with a flight height of 30 m. A total of 25 strips were made in the W-E direction and a total of 1524 visible images and 1149 thermographic images were acquired. The ground sample distance (GSD) was 1 cm for the visible images and 5.7 cm for the thermographic images.

At the PV plant at Albacete, two separate flights were executed with a flight height of 70 m and 25 m for RGB and IRT, respectively. As a result, a total of 236 visible images and 5313 thermographic images were acquired. The GSD was 2 cm for the visible images and 3 cm for the thermographic images. These GSDs were considered valid for the detection of hot spots according to the specifications provided by the manufacturer and the size of the PV cells.

All the images, together with the navigation data, constituted the input data for the photogrammetric process in SunMap following the pipeline outlined in Figure 1. As a result, the extraction and matching of features (Figure 8a) was applied successfully in both visible and thermographic images using SIFTGPU [29], and image-based 3D reconstruction was performed incrementally through an iterative process consisting of relative image orientation, triangulation, and bundle adjustment [32] (Figure 8b).

(**a**)
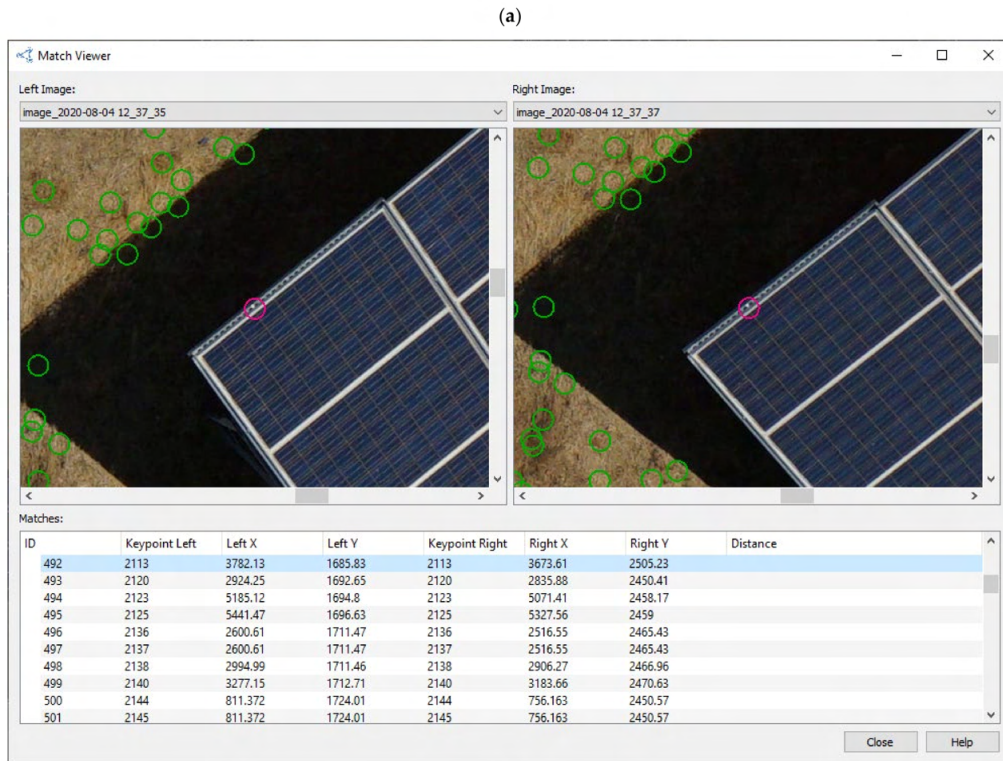
(**b**)
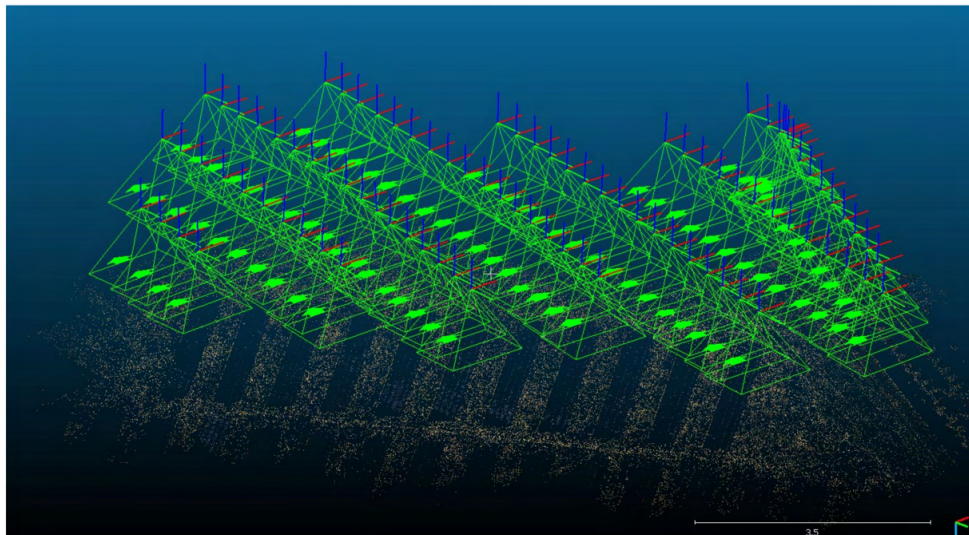
Figure 8. Photogrammetric processing in SunMap: (**a**) extraction of features based on SIFTGPU. The green circles represent the extracted points in the different images. The red circle represents the selected and matched point; (**b**) bundle adjustment imagery orientation based on collinearity condition and including camera self-calibration.

Regarding the self-calibration of cameras, the Fraser model [45] was applied to estimate two-radial-lens distortion ($k1$, $k2$) and two-decentering-lens distortion ($p1$, $p2$) parameters together with the focal length (f) and the principal point displacement (cx, cy). The following table (Table 2) outlines the inner calibration parameters for the different cameras used.

Table 2. Self-calibration of RGB and IRT cameras in the different case studies.

Location of PV Plants	RGB	IRT
PV plant, Albacete	f: 3549.6891 cx: −13.4458 cy: 12.6957 $k1$: −0.25872317 $k2$: 0.11303087 $p1$: −0.00101272 $p2$: −0.00031058	f: 792.1776 cx: 10.1731 cy: 4.4445 $k1$: 0.31691682 $k2$: −0.03630885 $p1$: −0.00292202 $p2$: −0.00170231
PV plant, Caceres	f: 3952.0199 cx: 2944.9719 cy: 1915.3403 $k1$: 0.05358915 $k2$: 0.03855508 $p1$: 0.00617445 $p2$: 0.00389557	f: 496.8117 cx: 326.6674 cy: 261.1664 $k1$: −0.30101814 $k2$: 0.137739510 $p1$: −0.00177455 $p2$: −0.00001426

4.2. Generation of Cartographic Products

The generation of cartographic products was focused on the generation of three-dimensional dense point clouds using the multiple view stereo strategy, followed by the generation of digital terrain and surface models (DTM/DSM) in raster format. Finally, the true orthoimages were generated with an average GSD of 1 cm as a final cartographic product for the geolocation of the hot spots.

For the Albacete PV plant, the dense point cloud obtained contained a total of 410 million points, which were later optimized to a point cloud of 5.2 million points in order to generate both the DTM and the DSM with a GSD of 3.5 cm.

For the Caceres PV plant, the dense point cloud obtained yielded a total of 45 million points, which were later optimized in a point cloud of 18.8 million in order to generate the DTM and the DSM with a GSD of 10 cm. Figure 9 outlines the different cartographic products obtained. These GSDs for the DSMs can be considered valid considering the size of a PV cell.

(**a**)   (**b**)

(**c**)   (**d**)

Figure 9. *Cont.*

(c)

(d)

(e)

(f)
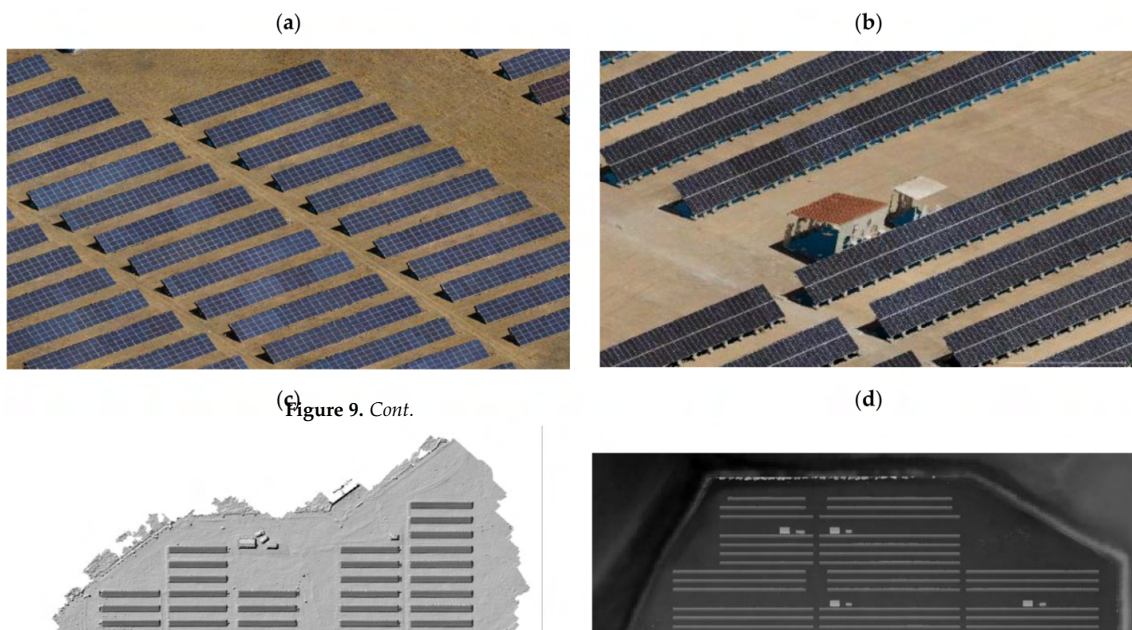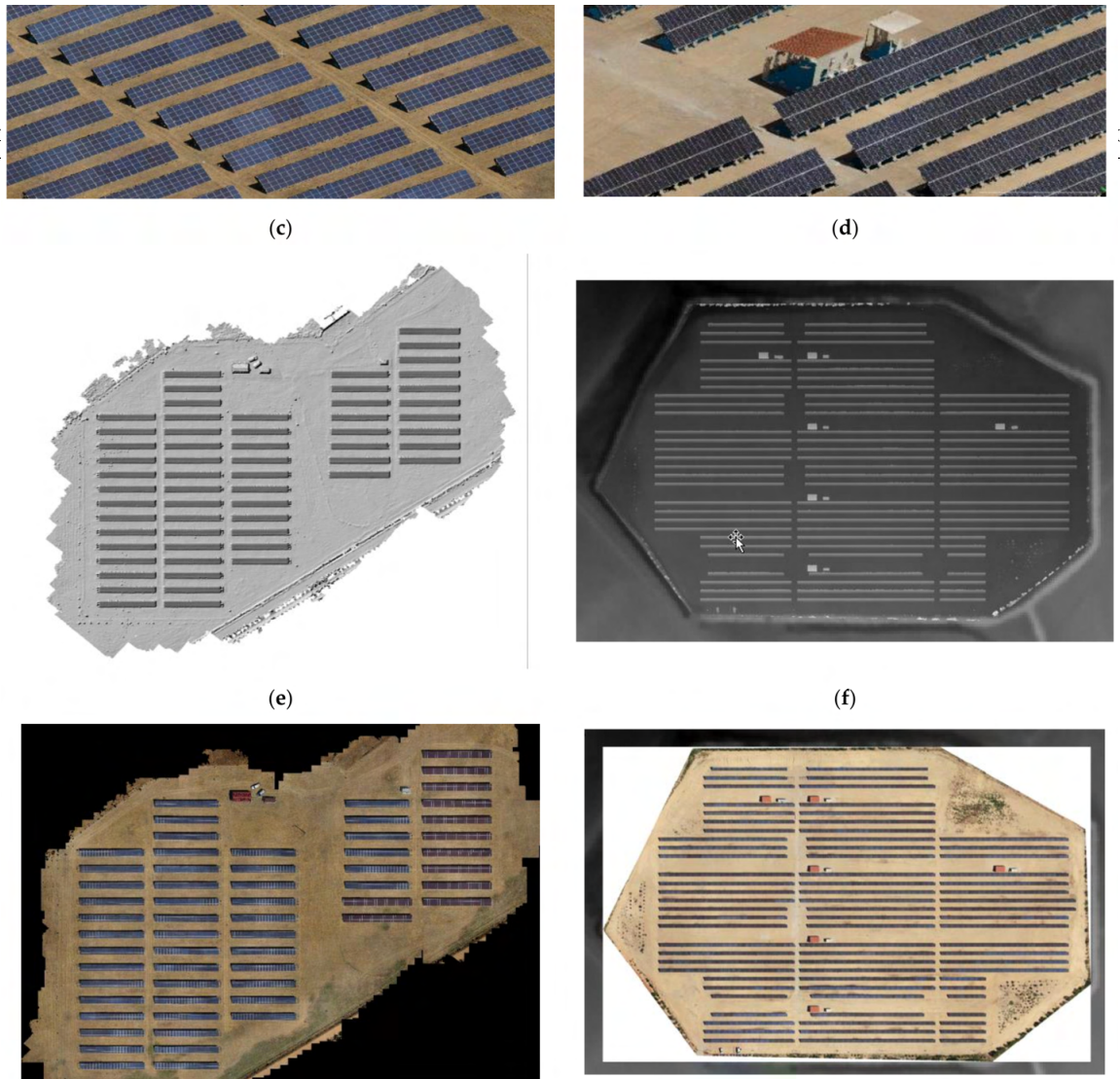
Figure 9. Cartographic products resulting from SunMap: 3D point clouds obtained in the PV plants of Caceres (**a**) and Albacete (**b**). DSM in vector format obtained at the Caceres PV plant (**c**). DSM in raster format obtained at the Albacete PV plant (**d**). True orthoimages from visible images generated at the PV plants at Caceres (**e**) and Albacete (**f**).

4.3. Extraction and Detection of PV Panels

The extraction and detection of PV panels was performed following a coarse-to-fine approach applying different advanced linear feature extraction operators and using the true orthoimages as input data, since they have good resolution and are georeferenced in metric coordinates. The results of the discretization process for the PV panels were carried out at three levels (Figure 10): (i) array level (in green), including the entire linear structure composed of a series of rows and columns of panels; (ii) panel level (in red), where the different panels were grouped by rows or columns; and (iii) module level (in yellow), where the different modules that compose the PV panels were discretized.

(a)

(b)
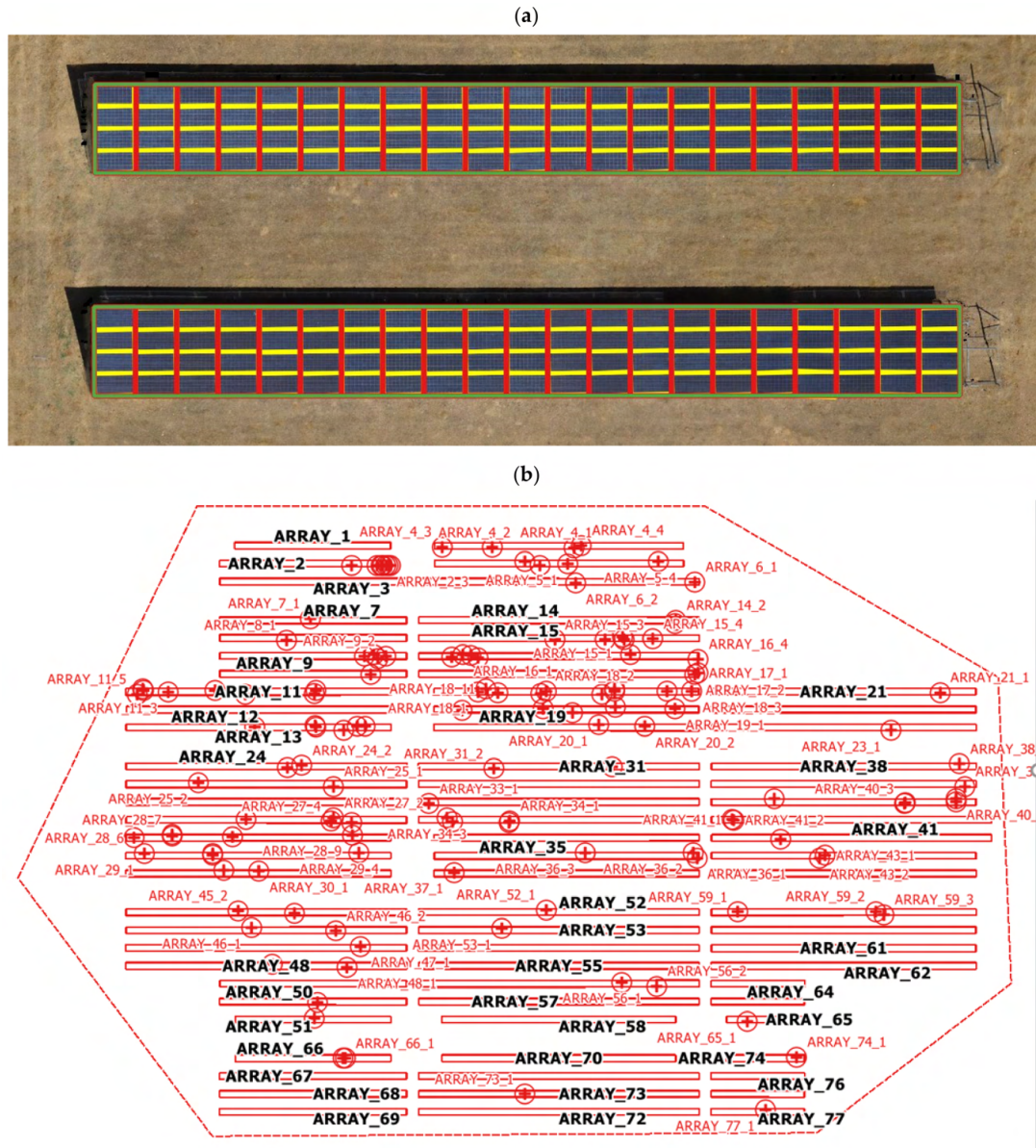
Figure 10. (**a**) Extraction and detection of PV panels using SunMap and following hierarchical discretization: detection of PV arrays in green, detection of PV panels in red, and detection of PV modules in yellow; (**b**) Structured information of the PV panels in vector format corresponding to PV arrays resulting from the automatic extraction and detection process.

As a result of this process, a geospatial database was generated in shapefile format that contains the hierarchical structure of the arrays, panels, and modules extracted and which is also used to precisely geolocate the hot spots in the expert report.

4.4. Hot Spot Detection and Report Generation

Finally, the hot spot detection was computed for both PV plants in UTM coordinates, including semantic information regarding array-panel identification and robust statistical information related to the temperature increment (10 °C) and affected area (m²). One of the main advantages of the SunMap tool is the capability to apply different corrections to the thermographic images (i.e., distance, angle, reflection and atmospheric), together with providing a robust statistical analysis of hot spots. As a result, a new table (Table 3) has been created including statistical information alongside the geometry of the set of pixels corresponding to a hot spot. All this information is included in the final expert report following the structure outlined in Figure 11.

Table 3. Geolocation of hot spots in UTM coordinates and identification of the array and panel affected.

Location of PV Plants	Hot Spot Coordinates	Semantic Information	$\Delta T_{\mu\varepsilon\delta\iota\alpha\nu}$	$\Delta T_{B\Omega M\varsigma}$	$\Delta T_{\mu\iota\nu}$	$\Delta T_{\mu\alpha\xi}$	Area
	(X, Y, UTM)	(Array/Panel)	(°C)	(°C)	(°C)	(°C)	(m²)
PV plant, Albacete	H1: (608693.292, 4298641.314)	Array_2_Panel_6	14.8	0.2	14.6	15.2	0.0006
	H2: (608686.307, 4298603.146)	Array_9_Panel_1	15.7	2.4	10.1	30.3	0.1514
	H3: (608593.379, 4298588.754)	Array_11_Panel_4	12.1	1.5	10	16.3	0.0343
	H4: (608722.99, 4298602.731)	Array_16_Panel_6	12.9	2	10	15.4	0.0184
	H5: (608816.908, 4298616.944)	Array_14_Panel_1	14	2.6	10.1	20.7	0.0963
	H6: (608804.4, 4298573.71)	Array_20_Panel_2	15.2	0.6	14.2	15.9	0.0099
	H7: (608762.854, 4298588.594)	Array_18_Panel_5	14.7	3.3	10.4	23.2	0.0596
	H8: (608684.113, 4298520.685)	Array_29_Panel_4	14.1	2.2	10.1	20.9	0.0426
	H9: (608636.663, 4298534.604)	Array_27_Panel_1	13	2	10.1	17.5	0.02
	H10: (608681.254, 4298528.101)	Array_28_Panel_9	12.5	2.1	10.5	15.4	0.0092
	H11: (608913.738, 4298541.88)	Array_42_Panel_1	13.4	2.6	10.1	20.9	0.0879
	H12: (608665.377, 4298451.152)	Array_51_Panel_1	12.5	0.2	11.8	13.5	0.0022
	H13: (608677.44, 4298434.384)	Array_66_Panel_2	11.6	0.9	10	14	0.0343
PV plant, Caceres	H1: (271960.445, 4338451.632)	Array_2_Panel_2	14.6	0.1	14.4	15	0.0986
	H2: (271961.776, 4338450.219)	Array_2_Panel_6	14.8	3.3	10.8	18.3	0.011
	H3: (271987.440, 4338413.552)	Array_11_Panel_3	14.1	2.7	10	22	0.8326
	H4: (271967.000, 4338424.524)	Array_11_Panel_5	14	2.2	10.3	23.1	0.0983
	H5: (271965.387, 4338422.592)	Array_12_Panel_6	14.5	2.5	10.4	20.3	0.0381
	H6: (271919.947, 4338350.703)	Array_16_Panel_3	12.7	0.2	12.1	13.9	0.0185
	H7: (271923.550, 4338333.465)	Array_18_Panel_3	13.3	1.6	10	19.4	0.1876
	H8: (272004.211, 4338386.299)	Array_26_Panel_5	13.9	2.2	10	22.3	0.0946
	H9: (271956.918, 4338359.317)	Array_28_Panel_9	14.3	2.4	10.3	21.7	0.0116
	H10: (271988.745, 4338342.373)	Array_30_Panel_6	14.2	3	10.1	21	0.1218
	H11: (271941.599, 4338307.870)	Array_31_Panel_5	10.6	0.1	10.4	10.7	0.0016
	H12: (271933.203, 4338305.567)	Array_31_Panel_6	13.9	2.2	10	20.9	0.0518
	H13: (271922.018, 4338306.404)	Array_31_Panel_7	11.8	1.9	10	15.8	0.0216
	H14: (271975.008 4338333.946)	Array_34_Panel_7	14.5	3.6	10.6	20.8	0.048
	H15: (272079.122, 4338433.789)	Array_38_Panel_7	12.7	0.3	12.4	13	0.2917
	H16: (271961.229, 4338315.750)	Array_51_Panel_10	12.9	0	12.8	12.9	0.002

Figure 11. *Cont.*
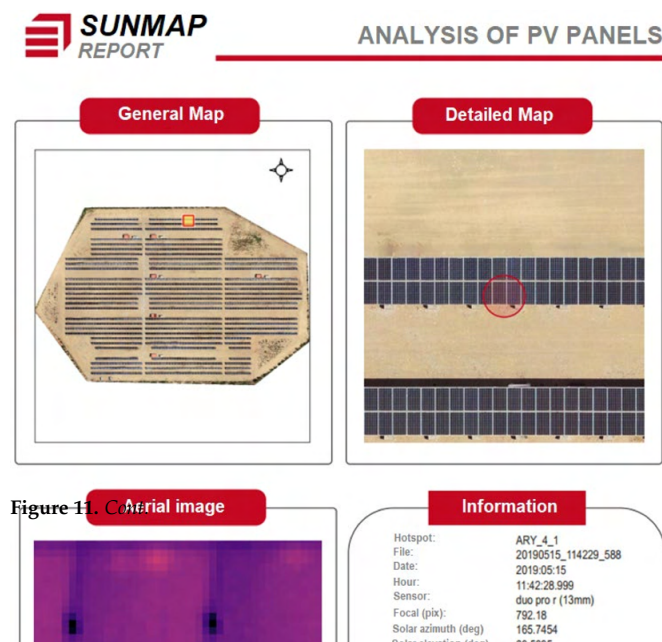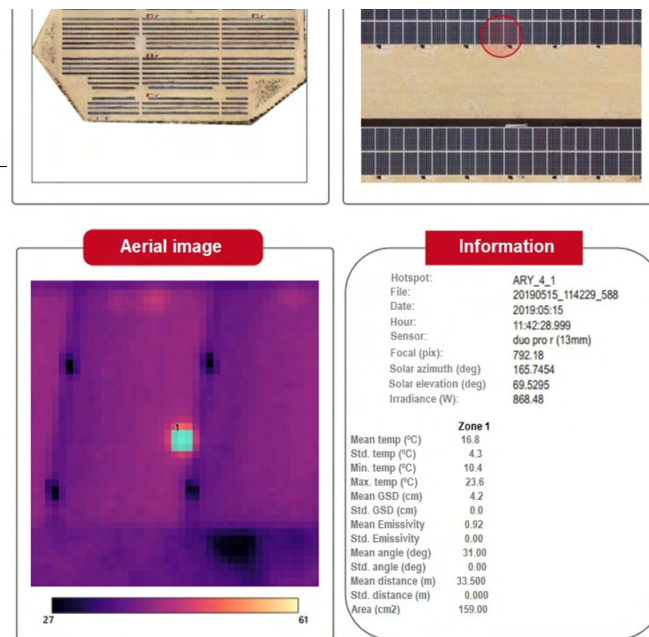
Figure 11. Example of an expert report produced by the SunMap tool to support maintenance operations in PV plants.

5. Discussion

In this section, we discuss the core aspects of this article: (1) drone acquisition; (2) photogrammetric processing; and (3) hot spot detection.

Regarding drone acquisition, multirotor and multimodal imagery (i.e., RGB and IRT) are key starting points to which particular attention should be paid. In particular, a flight planning mission is essential for guaranteeing automation of inspection, especially considering the different technical features of RGB and IRT cameras in terms of resolution, field of view, etc. In those cases where a simultaneous acquisition flight is not possible, two different flights will be required. Our flight-planning software [44] allows dealing with all these specifications, providing successful integration of RGB and IRT cameras.

Drone photogrammetry has successfully proven its efficiency and reliability in PV plant inspection. Drone photogrammetry supported by SfM and MVS is autonomous and saves time and cost; however, real-time processing is not possible, requiring postprocessing of the multimodal dataset acquired. Although different projects have implemented aerial drones for image acquisition, the majority did not take advantage of the full benefits of modern photogrammetry and computer vision workflow. In particular, the images acquired in other approaches were not orthorectified based on true orthoprojection. This prevents making accurate measurements, which simplify quantitative assessment of defective regions. These true orthoimages can be also integrated into a GIS, enabling spatial analysis operations and establishing a regular database for the inspected PV plant.

Regarding hot spot detection, although different works have tested artificial intelligence approaches, they require creating a complete benchmark, which is always a significant drawback. To this end, a hybrid and a coarse-to-fine method seems to be an efficient method for accurately and reliably detecting hot spot faults. RGB and IRT images complement each other, so a robust analysis can be performed to extract the different elements and detect false hot spots. Different projects have addressed the automatic extraction of modules, cells and defects through image processing pipelines, but noise reduction in IRT images is often a problem for applying further processing operations such as segmentation, edge extraction, and hot spot detection. In this regard, we considered a rigorous correction of IRT images based on distance, reflection, atmosphere and incident angle. Last but not least, a robust statistical analysis was used for the detection of hot spots in IRT images. Thresholds were selected based on statistical assumptions regarding the temperature distribution, as well as additional assumptions related to the correction of reflection from other PV modules.

6. Conclusions

This study presents a rigorous method for detecting hot spots in PV plants using an in-house software application, SunMap, which been proposed and validated. SunMap is a novel tool based on drone photogrammetry that is able to automatically detect and geolocate hot spot faults in PV plants. Moreover, the tool enables the generation of high-detailed cartographic products by means of 3D models and true orthoimages, which complement the maintenance and inspection operations required for this type of critical infrastructure. The tool was successfully validated in two different PV plants to provide accurate and reliable checking of hot spot faults.

In summary, the principal conclusions based on the results obtained with the SunMap tool are:

- A rigorous photogrammetric approach able to deal with RGB and IRT images is provided.
- 3D dense models and true orthoimages are generated automatically with high quality and metric properties.
- Automatic extraction and database coding of the structural information regarding the PV panels is integrated into the software, guaranteeing subpixel precision.
- Important thermographic corrections and robust statistical analysis are encoded within the software, providing rigorous thermographic treatment of images.
- The hot spot detection is reliable and accurate, and is reinforced with an expert report which integrates all the information required for maintenance operations.

In terms of future perspectives, the classification of pathologies according to IEC TS 62446-3, including Deep Learning techniques using geometric and radiometric information as input data, will be considered as next steps.

References

1. Oskouei, M.Z.; Seker, A.A.; Tunçel, S.; Demirba¸s, E.; Gözel, T.; Hocaoğlu, M.H.; Abapour, M.; Mohammadi-Ivatloo, B. A Critical Review on the Impacts of Energy Storage Systems and Demand-Side Management Strategies in the Economic Operation of Renewable-Based Distribution Network. *Sustainability* **2022**, *14*, 2110. [CrossRef]
2. Gonzalez-Aguilera, D.; Rodriguez-Gonzalvez, P. Drones—An Open Access Journal. *Drones* **2017**, *1*, 1. [CrossRef]
3. Montes, G.A.; Goertzel, B. Distributed, decentralized, and democratized artificial intelligence. *Technol. Forecast. Soc. Chang.* **2019**, *141*, 354–358. [CrossRef]
4. González-Aguilera, D.; López-Fernández, L.; Rodríguez-Gonzálvez, P.; Hernández-López, D.; Guerrero, D.; Remondino, F.; Menna, F.; Nocerino, E.; Toschi, I.; Ballabeni, A.; et al. GRAPHOS—Open-Source Software for Photogrammetric Applications. *Photogramm. Rec.* **2018**, *33*, 11–29. [CrossRef]
5. Fernández-Hernandez, J.; González-Aguilera, D.; Rodríguez-Gonzálvez, P.; Mancera-Taboada, J. Image-based modelling from unmanned aerial vehicle (UAV) photogrammetry: An effective, low-cost tool for archaeological applications. *Archaeometry* **2015**, *57*, 128–145. [CrossRef]
6. IEC TS 62446-3, Thecnical Specification: Photovoltaic (PV) Systems—Requirements for Testing, Documentation and Maintenance—Part 3: Photovoltaic Modules and Plants—Outdoor Infrared Thermography, Según la Edition 1.0 2017-06. Available online: https://webstore.iec.ch/publication/28628 (accessed on 30 December 2022).
7. Grimaccia, F.; Leva, S.; Dolara, A.; Achaea, M. Survey on PV Modules' Common Faults after an O&M Flight Extensive Campaign over Different Plants in Italy. *IEEE J. Photovolt.* **2017**, *7*, 810–816.

8. Salient, S.; Chouder, A.; Guerriero, P.; Pavan, A.M.; Mellit, A.; Moeini, R.; Tricoli, P. Monitoring, diagnosis, and power forecasting for photovoltaic fields: A review. *Int. J. Photoenergy* **2017**, *2017*, 1356851.

9. Tsanakas, J.A.; Ha, L.; Buerhop, C. Faults and infrared thermographic diagnosis in operating c-Si photovoltaic modules: A review of research and future challenges. Renew. Sustain. *Energy Rev.* **2016**, *62*, 695–709. [CrossRef]

10. Høiaas, I.; Grujic, K.; Imenes, A.G.; Burud, I.; Olsen, E.; Belbachir, N. Inspection and Condition Monitoring of Large-Scale Photovoltaic Power Plants: A Review of Imaging Technologies. *Renew. Sustain. Energy Rev.* **2022**, *161*, 112353. [CrossRef]

11. Meribout, M.; Kumar Tiwari, V.; Pablo Peña Herrera, J.; Baobaid, A.N.M.A. Solar Panel Inspection Techniques and Prospects. *Measurement* **2023**, *209*, 112466. [CrossRef]

12. Bellezza Quarter, P.; Grimaccia, F.; Leva, S.; Mussetta, M.; Aghaei, M. Light Unmanned Aerial Vehicles (UAVs) for cooperative inspection of PV plants. *IEEE J. Photovolt.* **2014**, *4*, 1107–1113.

13. Hu, Y.; Cao, W.; Ma, H.; Finney, S.J.; Li, D. Identifying PV Module Mismatch Faults by a Thermography-Based Temperature Distribution Analysis. *IEEE Trans. Device Mater. Reliab.* **2014**, *14*, 951–960. [CrossRef]

14. López-Fernández, L.; Lagüela, S.; Fernández, J.; González-Aguilera, D. Automatic Evaluation of Photovoltaic Power Stations from High-Density RGB-T 3D Point Clouds. *Remote Sens.* **2017**, *9*, 631. [CrossRef]

15. Tsanakas, J.A.; Chrysostomou, D.; Botsaris, P.N.; Gasteratos, A. Fault diagnosis of photovoltaic modules through image processing and Canny edge detection on field thermographic measurements. *Int. J. Sustain. Energy* **2015**, *34*, 351–372. [CrossRef]

16. Afifah, A.N.N.; Indrabayu; Suyuti, A.; Syafaruddin. Hotspot detection in photovoltaic module using Otsu thresholding method. In Proceedings of the IEEE International Conference on Communication, Networks and Satellite (Comnetsat), Batam, Indonesia, 17–18 December 2020; pp. 408–412.

17. Aghaei, M.; Grimaccia, F.; Gonano, C.A.; Leva, S. Innovative automated control system for PV fields inspection and remote control. *IEEE Trans. Ind. Electron.* **2015**, *62*, 7287–7296. [CrossRef]

18. Henry, C.; Poudel, S.; Lee, S.-W.; Jeong, H. Automatic Detection System of Deteriorated PV Modules Using Drone with Thermal Camera. *Appl. Sci.* **2020**, *10*, 3802. [CrossRef]

19. Piccinini, F.; Pierdicca, R.; Malinverni, E.S. A Relational Conceptual Model in GIS for the Management of Photovoltaic Systems. *Energies* **2020**, *13*, 2860. [CrossRef]

20. Sánchez-Aparicio, M.; Martín-Jiménez, J.; Del Pozo, S.; González-González, E.; Lagüela, S. Ener3DMap-SolarWeb roofs: A geospatial web-based platform to compute photovoltaic potential. *Renew. Sustain. Energy Rev.* **2021**, *135*, 110203. [CrossRef]

21. Yahya, Z.; Imane, S.; Hicham, H.; Ghassane, A.; Safia, E.B.I. Applied imagery pattern recognition for photovoltaic modules' inspection: A review on methods, challenges and future development. *Sustain. Energy Technol. Assess.* **2022**, *52*, 102071. [CrossRef]

22. Wang, X.; Yang, W.; Qin, B.; Wei, K.; Ma, Y.; Zhang, D. Intelligent monitoring of photovoltaic panels based on infrared detection. *Energy Rep.* **2022**, *8*, 5005–5015. [CrossRef]

23. Oña, E.R.D.; Rodríguez-Martin, M.; Rodríguez-Gonzálvez, P.; Mora, R.; González-Aguilera, D. WELDMAP: A Photogrammetric Suite Applied to the Inspection of Welds. *Appl. Sci.* **2022**, *12*, 2553. [CrossRef]

24. Oña, E.R.D.; Sánchez-Aparicio, M.; Del Pozo, S.; González-Aguilera, D. INSPECTORMAP: A Spatial Data Infrastructure Applied to the Maintenance of Solar Plants Using Free Satellite Imagery. *Appl. Sci.* **2022**, *12*, 70.

25. Moser, D.; Del Buono, M.; Bresciani, W.; Veronese, E.; Jahn, U.; Herz, M.; Janknecht, E.; Ndrio, E.; De Brabandere, K.; Richter, M. Technical risks in PV projects development and PV plant operation D1.1. D2.1. *Solar Bankability Project* **2016**, *1*, 1–139.

26. Cledat, E.; Jospin, L.V.; Cucci, D.A.; Skaloud, J. Mapping quality prediction for RTK/PPK-equipped micro-drones operating in complex natural environment. *ISPRS J. Photogramm. Remote Sens.* **2020**, *167*, 24–38. [CrossRef]

27. Furukawa, Y.; Hernández, C. *Multi-View Stereo: A Tutorial, Foundations and Trends®in Computer Graphics and Vision*; Now Publishers Inc.: Hanover, MA, USA, 2015; Volume 9, pp. 1–148.

28. Lowe, D.G. Distinctive image features from scale-invariant keypoints. *Int. J. Comput. Vis.* **2004**, *60*, 91–110. [CrossRef]

29. Wu, C. A GPU Implementation of Scale Invariant Feature Transform (SIFT). Available online: https://github.com/pitzer/SiftGPU (accessed on 12 April 2022).

30. Muja, M.; Lowe, D.G. Fast approximate nearest neighbors with automatic algorithm configuration. *VISAPP* **2009**, *2*, 2.

31. Fischler, M.A.; Bolles, R.C. Random sample consensus: A paradigm for model fitting with applications to image analysis and automated cartography. *Commun. ACM* **1981**, *24*, 381–395. [CrossRef]

32. Schönberger, J.L.; Frahm, J. Structure-from-Motion Revisited. In Proceedings of the IEEE Conference on Computer Vision and Pattern Recognition, Las Vegas, NV, USA, 27–30 June 2016; pp. 4104–4113.

33. Zhang, W.; Qi, J.; Wan, P.; Wang, H.; Xie, D.; Wang, X.; Yan, G. An Easy-to-Use Airborne LiDAR Data Filtering Method Based on Cloth Simulation. *Remote Sens.* **2016**, *8*, 501. [CrossRef]

34. Łukaszyk, S. A new concept of probability metric and its applications in approximation of scattered data sets. *Comput. Mech.* **2004**, *33*, 299–304. [CrossRef]

35. Gharibi, H.; Habib, A. True Orthophoto Generation from Aerial Frame Images and LiDAR Data: An Update. *Remote Sens.* **2018**, *10*, 581. [CrossRef]

36. Kraus, K. *Photogrammetry*; Ferd. Dummler's Verlag: Bonn, Germany, 1993; Volume 1, Fundamentals and standard processes; Volume 2, Advanced methods and applications.

37. Kudelka, M.; Horak, Z.; Voženílek, V.; Snasel, V. Orthophoto feature extraction and clustering. *Neural Netw. World* **2012**, *22*, 103–121. [CrossRef]

38. Visvalingam, M.; Whyatt, J.D. The Douglas-Peucker Algorithm for Line Simplification: Re-evaluation through Visualization. *Comput. Graph. Forum.* **2007**, *9*, 213–225. [CrossRef]
39. Martin, E.; Kriegel, H.-P.; Sander, J.; Xu, X. A density-based algorithm for discovering clusters in large spatial databases with noise. In Proceedings of the Second International Conference on Knowledge Discovery and Data Mining, Portland, OR, USA, 2–4 August 1996; pp. 226–231.
40. Tran, Q.H.; Han, D.; Kang, C.; Haldar, A.; Huh, J. Effects of Ambient Temperature and Relative Humidity on Subsurface Defect Detection in Concrete Structures by Active Thermal Imaging. *Sensors* **2017**, *17*, 1718. [CrossRef]
41. Ferreira, R.A.; Pottie, D.L.; Dias, L.H.; Cardoso Filho, B.J.; Porto, M.P. A Directional-Spectral Approach to Estimate Temperature of Outdoor PV Panels. *Sol. Energy* **2019**, *183*, 782–790. Available online: https://www.sciencedirect.com/science/article/pii/S0038092X19302786 (accessed on 7 February 2023). [CrossRef]
42. Rodríguez-Gonzálvez, P.; Garcia-Gago, J.; Gomez-Lahoz, J.; González-Aguilera, D. Confronting Passive and Active Sensors with Non-Gaussian Statistics. *Sensors* **2014**, *14*, 13759–13777. [CrossRef]
43. Kamran, A.; Khan, N.; Wajahat, A.; Hassan, A.; Khan, Y.; Yang, Y.; Shahrukh, A. Hotspot diagnosis for solar photovoltaic modules using a Naive Bayes classifier. *Sol. Energy* **2019**, *190*, 34–43.
44. Hernandez-Lopez, D.; Felipe-Garcia, B.; Gonzalez-Aguilera, D.; Arias-Perez, B. An automatic approach to UAV flight planning and control for photogrammetric applications. *Photogramm. Eng. Remote Sens.* **2013**, *79*, 87–98. [CrossRef]
45. Fraser, C.S. Digital camera self-calibration. *ISPRS J. Photogramm. Remote Sens.* **1997**, *52*, 149–159. [CrossRef]

Capítulo 5

Mantenimiento de plantas fotovoltaicas con teledetección

Capítulo 5

Mantenimiento de plantas fotovoltaicas con teledetección

En este capítulo se incluye el artículo *"INSPECTORMAP: A Spatial Data Infrastructure Applied to the Maintenance of Solar Plants Using Free Satellite Imagery"* publicado en la revista *Remote Sensing* en diciembre de 2021.

5.1. Resumen

En este cuarto artículo se planteó el objetivo de automatizar la detección de vegetación inusual y cuerpos de agua en las proximidades de plantas fotovoltaicas, con el fin de prevenir cualquier impacto negativo en su funcionamiento. En este contexto, el mantenimiento predictivo cobra especial relevancia ya que estas instalaciones son fundamentales para la generación de energía limpia y suelen ubicarse en áreas alejadas de entornos urbanos, a menudo abarcando grandes extensiones. Esta situación dificulta la realización de labores de mantenimiento convencionales y hace que se requiera de una monitorización continua. En este caso la teledetección se presenta como una técnica geomática adecuada para cumplir con este objetivo.

La monitorización de la presencia de masas de agua y superficies vegetales anómalas en el entorno de las plantas fotovoltaicas hace que se necesite disponer de imágenes satelitales actualizadas frecuentemente. Debido a esto, se han utilizado imágenes Landsat-8 (con una resolución temporal de 16 días) y Sentinel-2 (con una resolución temporal de 5 días) para lograr una gran cobertura temporal. Para manejar la gran cantidad de información que hay que gestionar se ha desarrollado un *script* en Python que permite consultar los productos disponibles en las plataformas de descargas de imágenes satélite, descargar de forma automática esa información, calcular automáticamente los índices espectrales usados para el seguimiento del estado de las instalaciones y publicar los resultados.

Para los estudios de vegetación en general, el índice de vegetación de diferencia normalizada (NDVI) es el más utilizado. Dicho índice, permite estimar la cantidad, calidad y crecimiento de la vegetación, gracias a la cantidad de radiación reflejada por esta en las bandas roja e infrarrojo cercano (NIR). Se define según la fórmula 5.1:

$$NDVI = \frac{NIR - ROJO}{NIR + ROJO} \tag{5.1}$$

Los valores que puede tomar están comprendidos entre -1 y 1, donde los valores más próximos a cero indican que no existe apenas vegetación, mientras que los valores próximos a 1 indican que la zona presenta vegetación abundante y vigorosa.

Con respecto a la identificación de masas de agua se ha usado el índice diferencial de agua normalizado (NDWI) según el método de McFeeters que emplea las bandas verde e infrarrojo cercano, como se refleja en la ecuación 5.2:

$$NDWI = \frac{VERDE - NIR}{VERDE + NIR} \tag{5.2}$$

Este índice permite maximizar la reflectancia del agua cuando se trabaja con longitudes de onda verdes, minimizando la reflectancia NIR del agua y maximizando la reflectancia NIR de la vegetación. Con ello es posible delimitar correctamente las masas de agua, así como analizar el grado de humedad de la vegetación. Al igual que el NDVI, los valores que puede llegar a tomar este índice se encuentran comprendidos entre -1 y 1, donde valores mayores a 0 indican cuerpos de agua o áreas con presencia de humedad.

Para facilitar el acceso y análisis de la información se desarrolló INSPECTOR-MAP, una IDE cuya arquitectura y características se describen en detalle en el apéndice B.6. En la parte del servidor se empleó Geoserver y para la parte cliente se desarrolló un visor con el *framework* Laravel usando los lenguajes PHP y JavaScript.

Para comprobar el correcto funcionamiento de la IDE INSPECTORMAP y corroborar su utilidad, se analizaron seis plantas fotovoltaicas ubicadas en España, con diferentes dimensiones y tipologías de terrenos en las parcelas colindantes (pastizales, cultivos y arbolado). En cuanto al estudio de la vegetación se abordó mediante el mapeo del vigor de la vegetación en un instante de tiempo dado, concluyendo que un valor del índice NDVI superior a 0,70 es indicativo de que la vegetación tiene un vigor suficientemente alto y por tanto serán necesarias tareas de mantenimiento para eliminarlo. A su vez se analizó la evolución de la vegetación a lo largo del tiempo mediante la creación de gráficas de índice NDVI. Estas gráficas permiten observar el comportamiento de la vegetación a lo largo del tiempo y planificar las posibles tareas de mantenimiento.

Se concluye que la herramienta INSPECTORMAP, gracias a las herramientas de monitorización de la presencia anómala de vegetación y cuerpos de agua,

permite llevar a cabo un mantenimiento de instalaciones solares fotovoltaicas tanto de pequeña como gran envergadura sin necesidad de realizar periódicamente inspecciones *in situ*.

Technical Note

INSPECTORMAP: A Spatial Data Infrastructure Applied to the Maintenance of Solar Plants Using Free Satellite Imagery

Esteban Ruiz de Oña, María Sánchez-Aparicio [ID], Susana Del Pozo [ID] and Diego González-Aguilera *[ID]

Department of Cartographic and Land Engineering, Higher Polytechnic School of Ávila, University of Salamanca, Hornos Caleros 50, 05003 Ávila, Spain; estebanrdo@usal.es (E.R.d.O.); mar_sanchez1410@usal.es (M.S.-A.); s.p.aguilera@usal.es (S.D.P.)
* Correspondence: daguilera@usal.es; Tel.: +34-920-353-500 (ext. 3820)

Abstract: Photovoltaic solar plants are one of the main facilities away from urban centers for the generation of clean energy. Since its appropriate maintenance ensures its suitable operation, optimizing their maintenance tasks in a preventive way is key. This article presents a spatial data infrastructure called INSPECTORMAP that, based on the analysis of free satellite images within the optical spectrum, can detect unusual vegetation and bodies of water in the vicinity of photovoltaic plants that can affect their correct operation. Thanks to the implementation of a monitoring and alert system, it is possible to know and map the status of the photovoltaic plant in terms of unusual coverages appearing, both natural and artificial, at any moment. Thus, maintenance workers would travel to the solar plant to carry out their maintenance tasks in this regard only when the system detects a risk.

1. Introduction

In the last decades, there has been an increase in world energy consumption motivated by population growth [1]. The data collected by The Global Energy Statistical Yearbook [2] indicate an average annual energy consumption growth of 2% during the 2000–2018 period. The annual forecast from the International Energy Agency (IEA) indicates that this trend will continue to increase. According to the 2019 IEA report [3], by the year 2040 there, will be an increase in global energy demand of 24% due to the increase in the world population and the improvement of living standards of the newly industrialized and developing nations. Within energy consumption, electricity has grown the most. Based on data collected by the IEA in 2018, the total world electricity consumption is 24,738.9 TWh [4]. Current world energy policies are focused on increasing renewable resources for energy generation to combat climate change and its impacts [5]. To date, only 27% of all electrical energy comes from renewable energy sources [2]. Given the significant cost reduction associated with renewable energy generation technologies, wind and sun are currently the main renewable energy sources used for large-scale electricity generation [6,7].

In recent years, photovoltaic solar plants have experienced significant growth, largely motivated by the greater accessibility to solar resources throughout the world geography. This type of facilities can reach high powers, so they require large surface areas for their suitable installation. Bhadla Solar Park, located in India, is the largest solar park in the world occupying 57 km^2 with a total electrical capacity of 2245 MW [8]. Above 2000 MW, there are only the Huanghe hydroelectric park in Hainan (China) [9,10], as well as the Pavagada photovoltaic solar park located in India [11,12].

Since these facilities cover large surfaces, their maintenance plays a key role for their correct operation and efficiency [13]. In this sense, remote sensing is a very useful technique. In recent years, many researchers have made use of drones to acquire thermal images of photovoltaic plants, mainly to know the status of the solar panels [14,15]. Li et al.

showed how the application of artificial intelligence networks allows for automating this process [16]. Another important aspect regarding the maintenance of photovoltaic installations is the conditions of their surroundings. The earth's surface is subject to continuous changes of both natural and artificial origin. Regarding the changes caused naturally, the presence of small or large masses of vegetation or the accumulation of water in the vicinity of these facilities can negatively affect their proper operation. These are changes that require continuous monitoring. Although drones allow capturing images with high spatial resolution, they turn out to be an expensive alternative due to the need for an expert pilot and frequent flights. In addition, these devices have other weaknesses: (i) impossibility of flying with extreme weather conditions such as strong winds, large episodes of rain, or high temperatures; (ii) limitation when flying large areas due to the autonomy of their batteries; (iii) the need to have an expert drone flight operator who oversees planning and executing the flight, which increases costs. As an alternative to this robotic technology, there are earth observation satellites capable of monitoring the surroundings of photovoltaic facilities over time. Currently, large space agencies such as NASA (National Aeronautics and Space Administration) and ESA (European Space Agency) have different Earth observation missions that capture images of the Earth's surface [17]. These are images that not only stand out for their free nature but also for their temporal and spectral resolution. This type of satellite captures images every few days, within several regions of the electromagnetic spectrum, which allows the detection of different elements of the Earth's surface by means of different spectral indices [18].

To efficiently manage this information, given its type and quantity, systems with a great capacity both to process and display satellite images, as well as to store them, are required. Although common Geographic Information System (GIS) tools are of great help in this regard, the use of a spatial data infrastructure (SDI) is a great alternative [19]. These are easy-to-use web tools that allow to automate the download, storage, and processing of data without the need for a computer with a large graphic and storage capacity, since everything is done through the cloud. Likewise, the latest advances in the Open Data Cube (ODC) standards [20,21] allow the integration and fusion of different satellite platforms and missions, improving and enhancing the analysis of different satellite products together.

Based on the above, this article shows how, thanks to the development of an SDI that feeds on free satellite images from the main world space agencies and under the ODC standard, the presence of water masses and the growth of vegetation in solar plants can be detected. After this introductory section, Section 2 presents the materials and methods used for the correct development of the application. Section 3 shows the experimental results, and finally, Section 4 will show the most significant conclusions of the study.

2. Materials and Methods

The SDI tool developed for the detection of water masses and vegetation changes in the vicinity of photovoltaic solar plants is based on Landat-8 and Sentinel-2 satellite images, as well as their integration according to a Local Nested Grid (LNG) [21].

2.1. Satellite Images to Monitor Earth Surface

To continuously monitor the phenomena and changes that occur on the Earth's surface, space agencies have satellites in orbit that carry different sensors on board to acquire data in this regard. Regarding the physical-mathematical model that underlies the acquisition of satellite images, it should be noted that it encompasses the conjunction of several phases, considering the Earth/atmosphere interaction of radiation and the internal physical behavior of the sensors. Sentinel-2 and Landat-8 images used in this paper are Level-2 products so that they are calibrated images with reflectance values at the bottom of the atmosphere [22,23]. Specifically, NASA and the United States Geological Survey (USGS), since 1972, has launched different Earth observation satellites under the name Landsat. Although Landsat-9 is the last satellite put into orbit (on 27 September 2021), Landsat-8 is the last to offer its products to date. Landsat-9 will start offering its products in early 2022.

Of the two instruments that Landsat-8 has on board, the OLI (Operational Land Imager) sensor captures images in different parts of the optical spectrum (Table 1) with a 16-day temporal resolution and a 12-bit radiometric resolution. Once Landsat-9 data begin to be offered, the temporal resolution offered by this constellation of satellites will be 8 days instead of 16 days.

Table 1. Main characteristics of the Landsat-8 OLI sensor.

Bands	Wavelength Range (μm)	Spatial Resolution (m)
B1—Coastal aerosol	0.43–0.45	30
B2—Blue	0.45–0.51	30
B3—Green	0.53–0.59	30
B4—Red	0.64–0.67	30
B5—NIR	0.85–0.88	30
B6—SWIR 1	1.57–1.65	30
B7—SWIR 2	2.11–2.29	30
B8—Panchromatic	0.50–0.68	15
B9—Cirrus	1.36–1.38	30

In recent years, the European Space Agency (ESA) has become a reference space agency thanks to the Copernicus earth observation program, in which satellite data are the main source of information. With a total of six families of satellites, under the name Sentinel, ESA is able to monitor different important parameters to improve the environmental management. Specifically, the constellation Sentinel-2 (2A and 2B), thanks to its MSI sensor, captures data within the optical spectrum (Table 2) with a 5-day temporal and a 12-bit radiometric resolution.

Table 2. Main characteristics of the Sentinel-2 MSI sensor.

Bands	Wavelength Range (μm)	Spatial Resolution (m)
B1—Coastal aerosol	0.43–0.45	60
B2—Blue	0.45–0.52	10
B3—Green	0.54–0.57	10
B4—Red	0.65–0.68	10
B5—Red Edge 1	0.68–0.71	20
B6—Red Edge 2	0.73–0.74	20
B7—Red Edge 3	0.77–0.79	20
B8—NIR 1	0.78–0.90	10
B8A—NIR 2	0.85–0.87	20
B9—Water Vapor	0.93–0.95	60
B10—Cirrus	1.36–1.39	60
B11—SWIR 1	1.56–1.65	20
B12—SWIR 2	2.10–2.28	20

Regarding the physical-mathematical model that underlies the acquisition of satellite images, it should be noted that it encompasses the conjunction of several phases, considering the Earth/atmosphere interaction of radiation and the internal physical behavior of the sensors. Sentinel-2 and Landat-8 images used in this paper are Level-2 products so that they are calibrated images with reflectance values at the bottom of atmosphere [22,23].

Both NASA and ESA have their own online platforms for downloading data captured by the corresponding satellite instrument. Due to the need for up-to-date images to carry out suitable monitoring of the appearance of water bodies or anomalous vegetation surfaces in the plant surroundings, a continuous download of data is required. This results in a large amount of information to be managed. For this reason, a Python script has been developed so that it allows: (i) reporting the available Landast-8 and Sentinel-2 Level-2 products along the photovoltaic plants by a proper query [24,25] to the downloading platforms, (ii) the automatic download of such information, (iii) the registration of the downloaded

products in the system catalog, (iv) the automatic calculation of various spectral indexes for monitoring the status of the photovoltaic plants, (v) the registration of these spectral indexes in the system catalog, and finally (vi) the publication of the spectral indexes in the SDI viewer through a map server. Likewise, the integration of Landsat-8 and Sentinel-2 images has been carried out according to an LNG developed by the authors [20].

There is a great variety of spectral indices that are applicable to different areas of knowledge such as agriculture, hydrology, and forestry, among others [26–28]. For studies on vegetation in general, the Normalized Difference Vegetation Index (NDVI) is the most widely used since it allows estimating the quantity, quality, and growth of vegetation, thanks to the amount of radiation reflected by vegetation in the red and near infrared electromagnetic spectrum (Equation (1)) [29].

$$NDVI = \frac{(NIR - Red)}{(NIR + Red)},$$ (1)

representing *NIR* and *Red* the surface reflectance values at the near infrared and red bands, respectively.

This index takes values between -1 and 1, where values close to zero indicate absence of vegetation or existence of dead vegetation, while values close to 1 indicate the existence of abundant and vigorous vegetation.

Regarding identifying water masses, the Normalized Differential Water Index (NDWI) is the most widely used spectral index [30]. Within the *NDWI*, there are different variants, although the most widely used, defined by the "McFeeters Method", considers the green and the near infrared bands (Equation (2)) [31].

$$NDWI = \frac{(Green - NIR)}{(Green + NIR)},$$ (2)

representing *Green* and *NIR* the surface reflectance values at the green and near infrared bands respectively.

The *NDWI* is a variant of the *NDVI*, in which the equation reverses the order of the *NIR*, and the red band is replaced by the green one. This relationship makes it possible to maximize the reflectance of the water when working with green wavelengths, minimizing the *NIR* reflectance of the water and maximizing the *NIR* reflectance of the vegetation. With this, it is possible to correctly delimit the water masses, as well as to analyze the degree of humidity of the vegetation. Such as the *NDVI*, the values that *NDWI* can take are between -1 and 1, where values greater than 0 indicate bodies of water or areas with the presence of moisture.

Finally, it should be mentioned that satellite images may contain inaccuracies, mainly due to the resolution limitation of the capture sensors. While this type of uncertainty can be minimized using fuzzy image pre-processors [32], in this case, it is admissible since the target is the detection of significant changes in vegetation and bodies of water.

2.2. Spatial Data Infrastructure

Any SDI is made up of data, metadata, processes to transform and query the data, and standardized web services for interacting between them. These software components are distributed according to a client-server architecture model (Figure 1). Specifically, the SDI INSPECTORMAP is developed under the language of Php and JavaScript using "Laravel" as a framework.

Behind the server-side of INSPECTORMAP (Back End, Figure 1) there is a Python script that, in combination with a PostgreSQL database, allows characterizing the areas to be studied as well as downloading and processing on a GeoServer the corresponding set of Landsat-8 and Sentinel-2 images. Furthermore, this script integrates an LNG [20] to ensure a more efficient integration of both data sets. From the downloaded images, the script automatically calculates the NDVI and NDWI spectral indices to analyze the presence of

vegetation and water bodies, as explained in the previous section. The result is stored on the server and consumed as Web Map Services (WMSs) to map the affected areas with different color scales and, as Web Feature Services (WFSs), to quantify the affected areas in m^2.
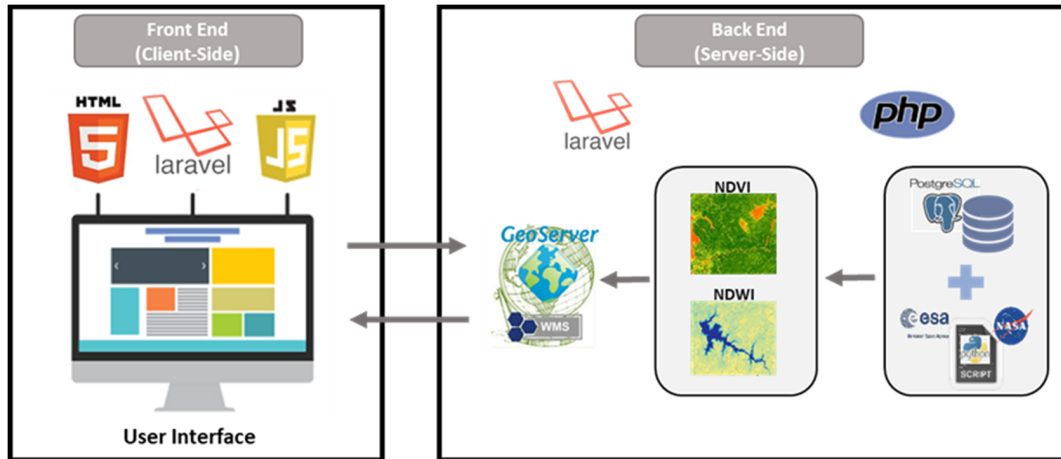
Figure 1. Workflow behind INSPECTORMAP, the Spatial Data Infrastructure proposed for the maintenance of photovoltaic plants.

The graphical interface of INSPECTORMAP (Front End, Figure 1) shows the results obtained in the server-side. It is a graphical interface that is mainly composed of three elements (Figure 2): (i) a geospatial information manager, (ii) a calendar, and (iii) a results viewer.
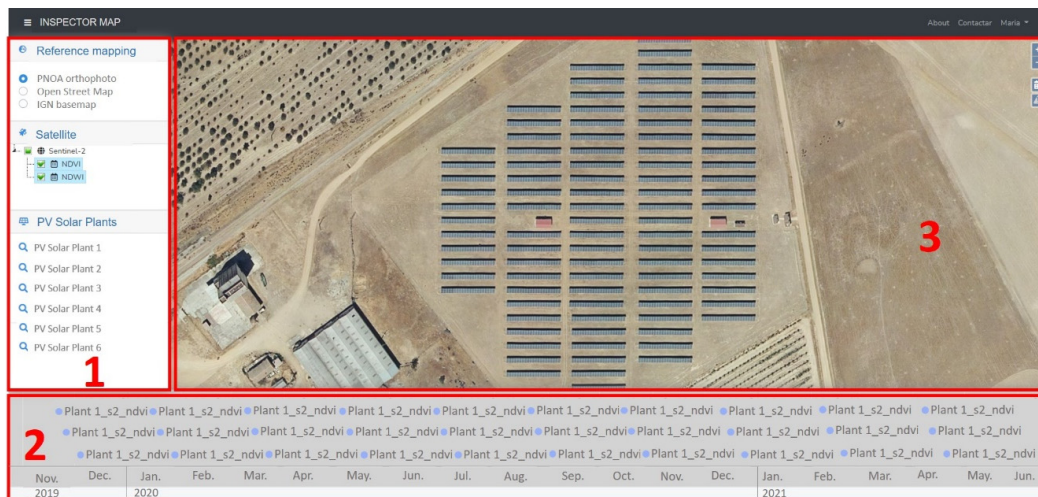
Figure 2. Graphic interface of the SDI INSPECTORMAP developed for the monitoring of photovoltaic plants.

2.2.1. Geospatial Information Manager

Given the large amount of geospatial information INSPECTORMAP manages, its interface allows, through the menu on the left, the user to select the type of reference base layer, the spectral index image, and the photovoltaic plant that he or she wishes to view (Figure 3). From among the reference base layers, the user can choose between: ortophotos from PNOA (Plan Nacional de Ortofotografía Aérea in Spanish, National Plan for Aerial

Orthophotography in English) [33], Open Street Map products [34], or a base map of the National Geographic Institute [35]. For a quick location of the study areas, the tool offers a list of all monitored photovoltaic plants in such a way that the user can supervise each one with just one click.
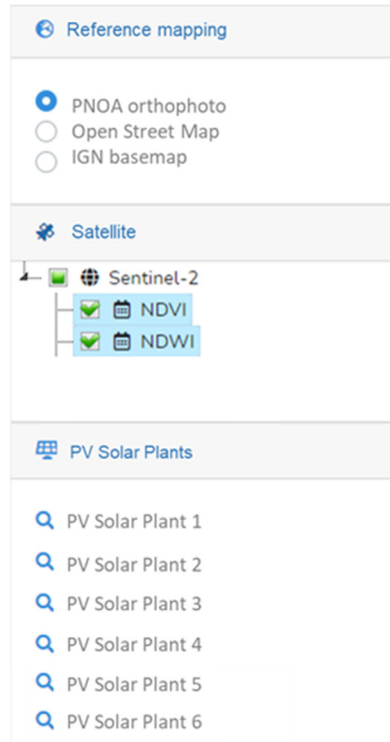
Figure 3. Geospatial information manager in detail.

2.2.2. Calendar

At the bottom of the interface, in the form of a calendar, the user can view the dates for which the spectral index images are available for the pre-selected photovoltaic plant (Figure 4). Furthermore, by clicking on each date, the product is automatically displayed in the results viewer.

Figure 4. Calendar of the available satellite products.

2.2.3. Results Viewer

Located in the central part of the graphical interface is the results viewer. This space is destined to display both the reference base layers and the spectral index images of the pre-selected photovoltaic plant. Thanks to this visualization, the user can qualitatively check the state of the vegetation and the existence of bodies of water in the vicinity of the

photovoltaic plant for a specific date, as well as (2) quantify the possible risk derived from their existence (Figure 5). The NDVI and NDWI images are represented in a color scale bar to aid in the interpretation of the associated risk.
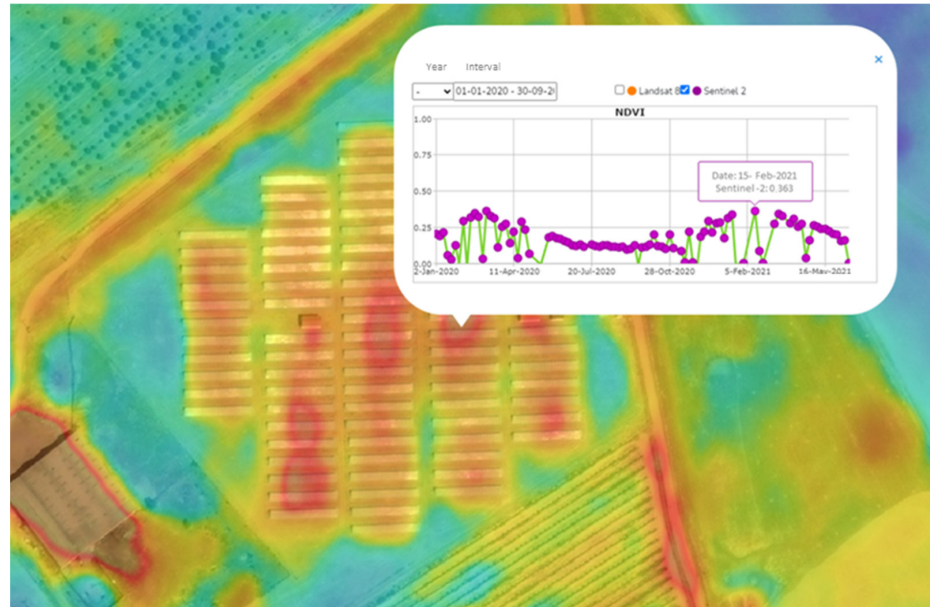
Figure 5. NDVI image display example of a photovoltaic solar plant for a given specific moment and the corresponding graph showing the NDVI variation over time for the selected pixel.

Thanks to an alert system implemented, the user can quickly detect if any of the photovoltaic plants included in the system have an atypical growth of vegetation or water surface in the vicinity by visualizing the affected areas as well as quantifying their surface in m^2 (Figure 6). In addition, this system allows for generating a report in pdf format with the most relevant information on the risk detected and the suggestions for the maintenance operator (Figure 7).
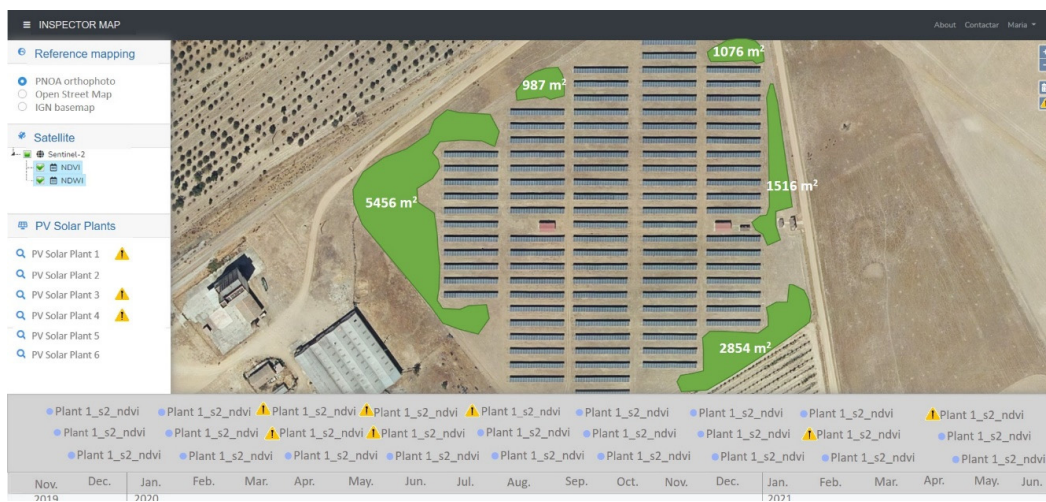
Figure 6. Visualization of results after activating the alert system in one of the photovoltaic solar plants included in the system.

Figure 7. Standard report generated by the SDI INSPECTORMAP when the alert system is activated.

3. Experimental Results

Since the maintenance of photovoltaic solar plants does not require the daily presence of an operator, in many cases, these facilities are neglected, operating in a non-optimal way. In this sense, INSPECTORMAP allows for detecting risks that may negatively affect the operation of the photovoltaic installation, which allows for optimizing the movements of maintenance workers. Thus, the operator in charge of checking the state of the solar plant surroundings will only appear before a real risk due to the growth of vegetation or the presence of water masses. The presence of large bodies of water or high levels of humidity in the soil can negatively affect the foundations of the facilities. In addition, the presence of water bodies can make accessibility to the plant difficult. This problem also occurs due to the existence of large vegetation in the vicinity. However, the presence of vegetation not only affects the accessibility, but also the performance of the installation itself. Large vegetation creates shadows on the solar panels, preventing solar radiation from striking the photovoltaic panels. In addition, the presence of vegetation is an attraction for animals and insects, which increases the presence of excrement on the solar panels, reducing their performance.

To verify the correct operation of the SDI INSPECTORMAP and to corroborate its usefulness, six photovoltaic plants located in Spain subjected to different conditions have been analyzed (Figure 8).

3.1. Study Cases

The first plant analyzed (Figure 8a) is a photovoltaic plant located in an area categorized as grassland, where the solar panels are grouped in two areas separated by a building occupying an area of 62,808 m^2. The adjacent plots are lands with the presence of trees.

The second plant (Figure 8b) has an area of 13,254 m^2. It is a photovoltaic plant that is characterized by the proximity between their solar panels. Regarding the vegetation, the adjoining plots are characterized by being grasslands.

Regarding the third photovoltaic plant (Figure 8c), it occupies an area of 29,271 m^2, in which there are areas with great spacing between groups of panels. From the vegetation

point of view, the area where the solar panels are installed is a grass area, while the plots adjacent to the installation are arable plots.

Figure 8. Photovoltaic plants analyzed with INSPECTORMAP to validate the tool performance: (**a**) plant 1, (**b**) plant 2, (**c**) plant 3, (**d**) plant 4, (**e**) plant 5, and (**f**) plant 6.

The fourth photovoltaic plant (Figure 8d) is the one with the largest surface area (155,204 m^2). Unlike the rest of the solar plants, this one is in an irrigated arable plot.

For its part, the fifth photovoltaic plant (Figure 8e) occupies an area of 11,753 m^2 and it is located on an arable plot. The vegetation surrounding the plant is characterized by wooded and arable areas.

Finally, the sixth photovoltaic plant analyzed (Figure 8f) occupies an area of 5303 m^2 and it is characterized by being located on a plot of grass. The adjoining parcel on the left has a wooded area with tall trees, while the adjoining parcel on the right corresponds with an arable land.

3.2. Results and Discussion

This section shows the results produced by the SDI INSPECTORMAP, which allow for the interpretation of the possible existing risks by a non-expert user. The user would be able to identify, through two ways, those areas where vegetation can be a problem for the operation of the solar installation: by means of (1) mapping the vigor of the vegetation at a given instant of time and the computation of the plant surface that would require to be eliminated, or through (2) the multitemporal analysis of the vegetation activity. Both ways are based on the calculation of the NDVI. In addition, and thanks to the NDWI map, it will allow to detect bodies of water that could affect the performance of the installations.

3.2.1. Mapping the Vigor of Vegetation at a Given Instant of Time

On the one hand, the tool displays, for a chosen date, the NDVI map the colors closer to brown indicate the absence of vegetation while the blue colors indicate the existence of vegetation with great vigor. Figure 9 shows the NDVI maps of the six plants analyzed during the month of May.

As previously stated, the six photovoltaic plants have in common that they are surrounded by grass. The maximum vigor of naturally grown grass (not watered) usually occurs between the months of April and May in the northern hemisphere. As a generic criterion, when the NDVI exceeds 0.70 [19], it is considered that the vegetation has sufficiently high vigor. Thus, for this specific application, this will be indicative of the need for maintenance tasks to eliminate it. In all cases (Figure 9), there is a percentage of vegetation that should be removed. It should be noted that, in plant 6, unlike the rest of the solar plants, the area where the solar panels are installed has a bluish-green hue while in the rest of the solar plants it has a reddish hue. This is not due to the presence of vegetation between panels, but to their great separation and the presence of vegetation with a notable vigor in the surroundings.

According to the alert system implemented, plants 1, 3, 4, and 6 are the ones with the largest area of vegetation to be removed: 54,418 m^2, 4486 m^2, 27,293 m^2, and 5100 m^2, respectively (Figure 10). For these cases, the NDVI value of the areas in need of maintenance have a mean value greater than 0.70; specifically, 0.76, 0.73, 0. 79, and 0.81, respectively.

3.2.2. Multitemporal Analysis of the Vegetation Activity

The NDVI graphs are the other option with which the INSPECTORMAP tool allows to know the evolution of the vegetation. Unlike static NDVI maps, NDVI graphs allow for knowing the activity and growth of vegetation over a period of time. It is a very interesting alternative to know the behavior of the vegetation over time and plan the possible maintenance tasks. As can be seen in Figure 11, for each of the photovoltaic plants analyzed, a moment of maximum growth and vigor of the vegetation is always appreciated. Depending on the type of plant, this behavior will vary throughout the year. It is worth mentioning that the value of NDVI on cloudy days decreases sharply, hence all the sharp drops in the charts. All those graphs that represent the vegetative activity of the existing grass between the solar panels (Figure 11a,c,e) show a similar behavior, since during the months of June, July, and August there is either no vegetation (Figure 11e) or it is dry (Figure 11a,c). Although Figure 11b shows a totally different behavior, the vegetation on the plot is also grass. On the contrary, in the case of Figure 11d, the behavior of a vegetation characterized by being watered is represented where the NDVI presents a high value due

to the vigor and humidity of the crop. Similarly, the plot to the left of the plant 6 exhibits high NDVI from April to October due to the vigor of the vegetation and its humidity.
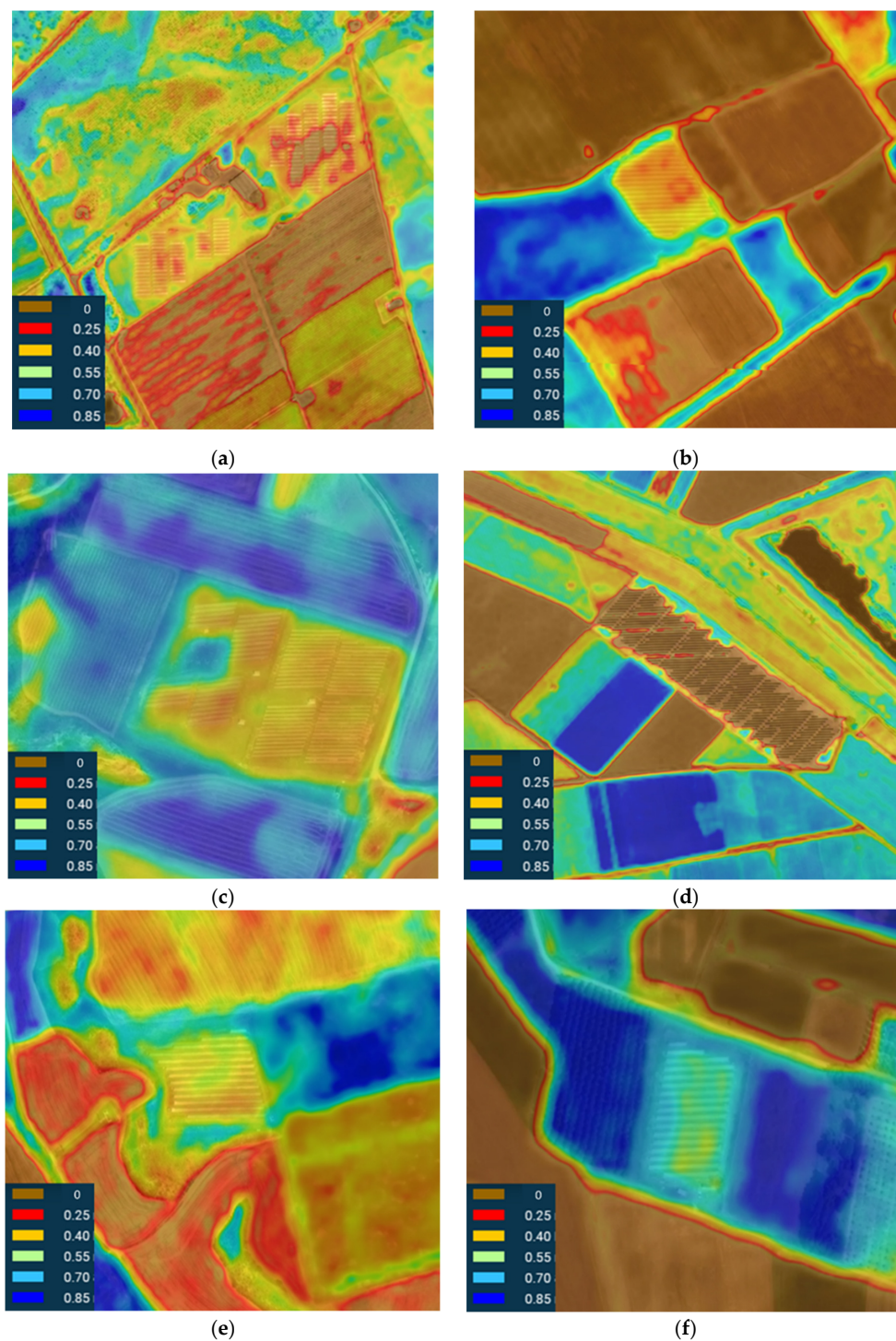
Figure 9. Graphic representation of the state of the vegetation through the NDVI for the different case studies in the month of May: (**a**) plant 1, (**b**) plant 2, (**c**) plant 3, (**d**) plant 4, (**e**) plant 5, and (**f**) plant 6.

Figure 10. Areas detected and quantified by the INSPECTORMAP alert system for the dates that reveal greater vegetal vigor: (**a**) plant 1, (**b**) plant 3, (**c**) plant 4, and (**d**) plant 6.
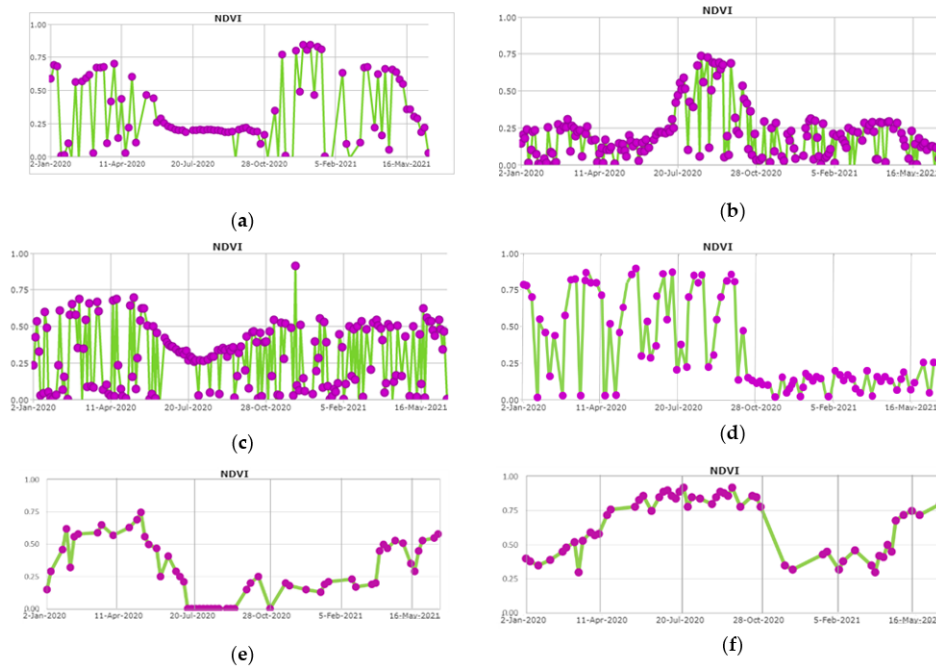
Figure 11. Vegetative activity through time in the vicinity of the photovoltaic plants analyzed by means of multitemporal NDVI graphs: (**a**) of the vegetation between the solar panels, (**b**) of the vegetation present in the adjacent right plot, (**c**) of the area without the presence of solar panels within the installation plot, (**d**) of the vegetation of the lower triangular plot, € of the vegetation surrounding the solar installation, (**f**) of the vegetation of the plot located to the left of the installation.

3.2.3. Mapping the Water Bodies at a Given Instant of Time

Solar installations are generally located in places away from large bodies of water such as rivers, lakes, or reservoirs. Sometimes, they are in areas close to water ponds that do not endanger the installation because they are far enough away (Figure 12).

(**a**) (**b**)
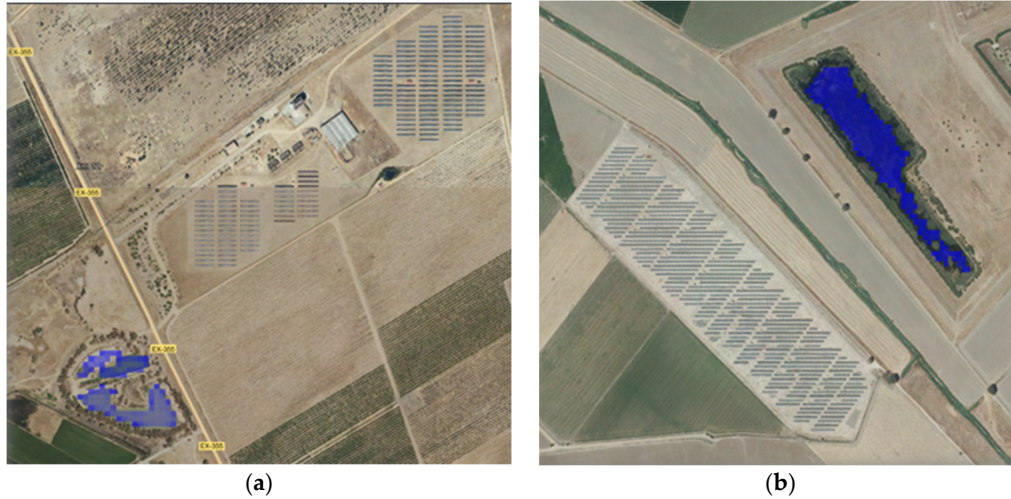
Figure 12. Water ponds detected with the NDWI index in the surroundings of (**a**) plant 1, and (**b**) plant 4.

However, it is becoming more and more frequent to find episodes of heavy rains that can cause the accumulation of water, which could endanger the correct operation of this type of facility. An example of this occurred on plant 1 during a heavy rain episode during October 2020. The alert system detected a body of water with an area of 2134 m^2 that not only limited the accessibility to the plant but could have put the installation in risk (Figure 13).
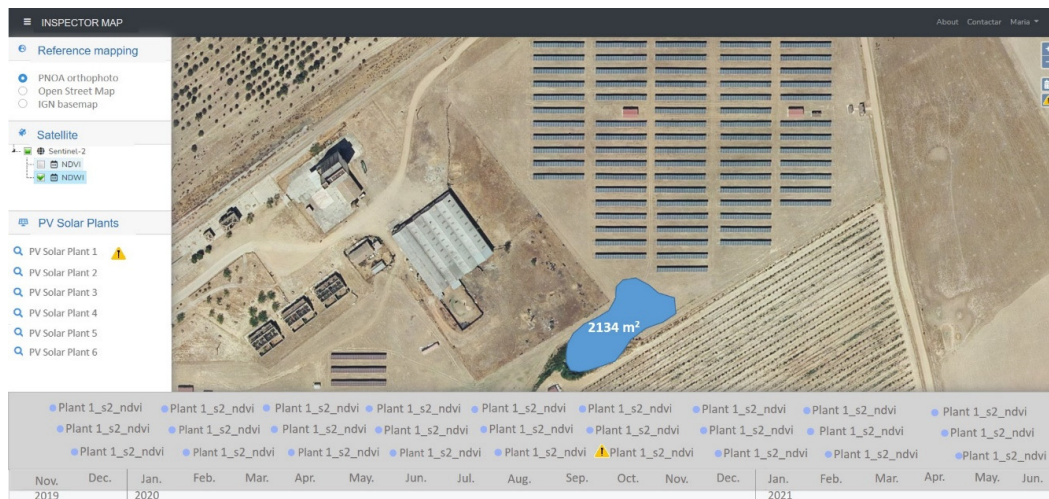
Figure 13. Body of water detected on plant 1 by the INSPECTORMAP alert system during an episode of heavy rain.

Although the NDWI is the most widely used spectral index for the detection of water masses, many authors are working on the development of new spectral indices. An example

of this is [36], who developed an *SWI* index for the detection of water masses using different spectral bands of Sentinel-2 (Equation (3)).

$$SWI = \frac{Rededge\,1 - SWIR\,1}{Rededge\,1 + SWIR\,1}, \tag{3}$$

While in the case of NDWI all the pixels are part of the water body, in the case of *SWI* there are "false positive" pixels (Figure 14c). When quantifying the area affected by the water body using the NDWI on plant 4, it is obtained that with a 10-m resolution image the value is 31,166 m^2 and with a 20-m resolution the value drops to 27,171 m^2. The area affected by water when applying the *SWI* index almost doubles, obtaining a value of 43,154 m^2.

(a)   (b)

(c)
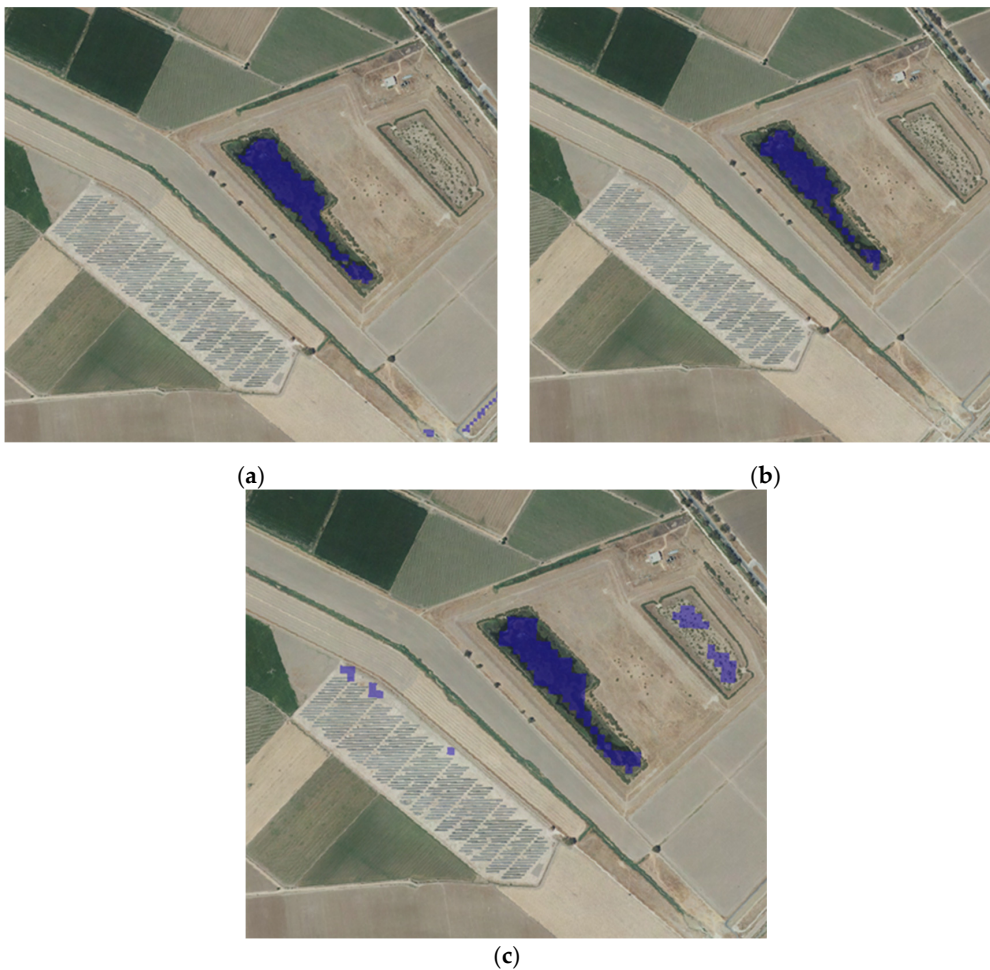
Figure 14. Bodies of water detected in the vicinity of plant 4 for a specific instant of time based on: (**a**) the NDWI with a 10-m spatial resolution, (**b**) the NDWI with a 20-m spatial resolution, and (**c**) the SWI with a 20-m spatial resolution.

4. Conclusions

The maintenance of photovoltaic solar plants plays a key role in terms of their performance and useful life. The INSPECTORMAP tool presented in this article allows for the maintenance of both small and large photovoltaic solar plants without the need for periodic on-site inspections.

Thanks to the revisit period of the satellites, different spectral indices can be calculated periodically and free of charge to detect those areas of the installation that require maintenance due to the presence of water or vegetation. The process of downloading and calculating these indexes is performed automatically thanks to a Python script implemented in the proposed SDI. Likewise, the integration of Landsat-8 and Sentinel-2 data is based on the Open Data Cube standard and the Local Nested Grid tool developed. This integration allows for maximum use of these products in geometric, radiometric, and temporal terms. In this way, the INSPECTORMAP user does not have to perform any calculations; they only have to analyze the results offered by the tool and be aware of the warnings the tool automatically generates when certain thresholds are exceeded.

Although the estimation of spectral indices for the detection of anomalous vegetation and water bodies is very useful, it must be considered that, in some cases, the quantified surfaces are not sufficiently precise. For this reason, the SDI INSPECTORMAP serves as a support tool to aid the maintenance operators to know the vegetation activity and water bodies growth in the surroundings of photovoltaic plants, which can be a potential risk for the operation of these facilities. As has been demonstrated with the estimation of the areas affected by vegetation, in most cases, the tool is very useful to know exactly the location where the operator will proceed to withdrawal.

Although there are several indices for estimating water bodies by satellite images, this contribution confirms that the NDWI index allows for a precise estimation of the affected areas compared to other indices such as the SWI, which tends to overestimate the areas with presence of water. As has been shown, the improved resolution of satellite imagery allows a more precise quantification. This improvement in precision is key for sensitive cases of large floods, in which a highly precise quantification of the affected area is required without involving a large computational expense.

References

1. Bakirtas, T.; Akpolat, A.G. The relationship between energy consumption, urbanization, and economic growth in new emerging-market countries. *Energy* **2018**, *147*, 110–121. [CrossRef]
2. Global Energy Statistical Yearbook. 2021. Available online: https://yearbook.enerdata.net/renewables/renewable-in-electricity-production-share.html (accessed on 8 November 2021).
3. International Energy Agency. Global Energy Review. 2019. Available online: https://www.iea.org/reports/global-energy-review-2019 (accessed on 8 November 2021).
4. International Energy Agency. Data and Statistics. Available online: https://www.iea.org/data-and-statistics?country=WORLD&fuel=Energy%20consumption&indicator=Electricity%20consumption (accessed on 17 November 2021).
5. IRENA. *Global Energy Transformation: A Roadmap to 2050*; International Renewable Energy Agency: Abu Dhabi, United Arab Emirates, 2018.
6. Balasubramanian, K.; Thanikanti, S.B.; Subramaniam, U.; Sudhakar, N.; Sichilalu, S. A novel review on Optimization Techniques used in Wind Farm Modelling. *Renew. Energy Focus* **2020**, *35*, 84–96. [CrossRef]

7.   Honrubia-Escribano, A.; Ramirez, F.J.; Gómez-Lázaro, E.; García-Villaverde, P.M.; Ruiz-Ortega, M.J.; Parra-Requena, G. Influence of solar technology in the economic performance of PV power plants in Europe. A comprehensive analysis. *Renew. Sustain. Energy Rev.* **2018**, *82*, 488–501. [CrossRef]
8.   Mercom India. Available online: https://mercomindia.com/world-largest-solar-park-bhadla/ (accessed on 13 October 2021).
9.   Saur Energy International. Available online: https://www.saurenergy.com/solar-energy-news/huawei-smart-pv-solution-highlights-role-in-worlds-largest-pv-plant (accessed on 13 October 2021).
10.   PV Magazine. Available online: https://pv-magazine-usa.com/2020/10/02/worlds-largest-solar-plant-goes-online-in-china/ (accessed on 13 October 2021).
11.   Nammatumkur. Available online: https://nammatumkur.com/worlds-largest-solar-power-park-at-karnataka-is-fully-operational/ (accessed on 26 October 2021).
12.   Mercom India. Available online: https://mercomindia.com/pavagada-solar-park-operational-december-2019/ (accessed on 25 October 2021).
13.   Hernández-Callejo, L.; Gallardo-Saavedra, S.; Alonso-Gómez, V. A review of photovoltaic systems: Design, operation, and maintenance. *Sol. Energy* **2019**, *188*, 426–440. [CrossRef]
14.   Gallardo-Saavedra, S.; Hernández-Callejo, L.; Duque-Pérez, O. Technological review of the instrumentation used in aerial thermographic inspection of photovoltaic plants. *Renew. Sustain. Energy Rev.* **2018**, *93*, 566–579. [CrossRef]
15.   Catalano, A.P.; Scognamillo, C.; Guerriero, P.; Daliento, S.; d'Alessandro, V. Using EMPHASIS for the Thermography-Based Fault Detection in Photovoltaic Plants. *Energies* **2021**, *14*, 1559. [CrossRef]
16.   Li, B.; Delpha, C.; Diallo, D.; Migan-Dubois, A. Application of Artificial Neural Networks to photovoltaic fault detection and diagnosis: A review. *Renew. Sustain. Energy Rev.* **2021**, *138*, 110512. [CrossRef]
17.   Irons, J.R.; Dwyer, J.L.; Barsi, J.A. The next Landsat satellite: The Landsat data continuity mission. *Remote Sens. Environ.* **2012**, *122*, 11–21. [CrossRef]
18.   Ahmed, K.R.; Akter, S. Analysis of landcover change in southwest Bengal delta due to floods by NDVI, NDWI and K-means cluster with Landsat multi-spectral surface reflectance satellite data. *Remote Sens. Appl. Soc. Environ.* **2017**, *8*, 168–181. [CrossRef]
19.   Piedelobo, L.; Ortega-Terol, D.; Del Pozo, S.; Hernández-López, D.; Ballesteros, R.; Moreno, M.A.; Molina, J.L.; González-Aguilera, D. HidroMap: A new tool for irrigation monitoring and management using free satellite imagery. *ISPRS Int. J. Geo-Inf.* **2018**, *7*, 220. [CrossRef]
20.   Hernández-López, D.; Piedelobo, L.; Moreno, M.A.; Chakhar, A.; Ortega-Terol, D.; González-Aguilera, D. Design of a Local Nested Grid for the Optimal Combined Use of Landsat 8 and Sentinel 2 Data. *Remote Sens.* **2021**, *13*, 1546. [CrossRef]
21.   Open Data Cube. Available online: https://www.opendatacube.org/ (accessed on 2 November 2021).
22.   Main-Knorn, M.; Pflug, B.; Louis, J.; Debaecker, V. Calibration and validation plan for the L2A processor and products of the Sentinel-2 mission. In Proceedings of the International Symposium on Remote Sensing of Environment (ISRSE), Berlin, Germany, 11–15 May 2015; Volume 40, pp. 1249–1255. [CrossRef]
23.   Czapla-Myers, J.; McCorkel, J.; Anderson, N.; Thome, K.; Biggar, S.; Helder, D.; Aaron, D.; Leigh, L.; Mishra, N. The ground-based absolute radiometric calibration of Landsat 8 OLI. *Remote Sens.* **2015**, *7*, 600–626. [CrossRef]
24.   USGS Search and Download Service. Available online: https://ers.cr.usgs.gov (accessed on 27 September 2021).
25.   OpenSearch Protocol. Available online: http://www.opensearch.org/Home (accessed on 14 September 2021).
26.   Martínez-Fernández, J.; González-Zamora, A.; Sánchez, N.; Gumuzzio, A.; Herrero-Jiménez, C.M. Satellite soil moisture for agricultural drought monitoring: Assessment of the SMOS derived Soil Water Deficit Index. *Remote Sens. Environ.* **2016**, *177*, 277–286. [CrossRef]
27.   Ryu, J.H.; Han, K.S.; Hong, S.; Park, N.W.; Lee, Y.W.; Cho, J. Satellite-based evaluation of the post-fire recovery process from the worst forest fire case in South Korea. *Remote Sens.* **2018**, *10*, 918. [CrossRef]
28.   Kaplan, G.; Avdan, U. Object-based water body extraction model using Sentinel-2 satellite imagery. *Eur. J. Remote Sens.* **2017**, *50*, 137–143. [CrossRef]
29.   Carlson, T.N.; Ripley, D.A. On the relation between NDVI, fractional vegetation cover, and leaf area index. *Remote Sens. Environ.* **1997**, *62*, 241–252. [CrossRef]
30.   Xu, H. Modification of normalised difference water index (NDWI) to enhance open water features in remotely sensed imagery. *Int. J. Remote Sens.* **2006**, *27*, 3025–3033. [CrossRef]
31.   McFeeters, S.K. The use of the Normalized Difference Water Index (NDWI) in the delineation of open water features. *Int. J. Remote Sens.* **1996**, *17*, 1425–1432. [CrossRef]
32.   Versaci, M.; Calcagno, S.; Morabito, F.C. Image contrast enhancement by distances among points in fuzzy hyper-cubes. In Proceedings of the International Conference on Computer Analysis of Images and Patterns, Valletta, Malta, 2–4 September 2015; Springer: Cham, Switzerland, 2015; pp. 494–505. [CrossRef]
33.   Arozarena, A.; Villa, G.; Valcárcel, N. The National Aerial Ortophoto Program in Spain (PNOA). In Proceedings of the International Cartographic Conference, La Coruña, Spain, 9–16 July 2005.
34.   Haklay, M.; Weber, P. Openstreetmap: User-generated street maps. *IEEE Pervasive Comput.* **2008**, *7*, 12–18. [CrossRef]
35.   Instituto Geográfico Nacional. Available online: https://www.ign.es/web/cbg-area-cartografia (accessed on 13 October 2021).
36.   Jiang, W.; Ni, Y.; Pang, Z.; He, G.; Fu, J.; Lu, J.; Yang, K.; Long, T.; Lei, T. A new index for identifying water body from SENTINEL-2 satellite remote sensing imagery. *ISPRS Ann. Photogramm. Remote Sens. Spat. Inf. Sci.* **2020**, *3*, 33–38. [CrossRef]

Capítulo 6

Conclusiones

Capítulo 6

Conclusiones

6.1. Conclusiones

En la presente tesis doctoral se planteó el estudio y desarrollo de geotecnologías aplicadas a la industria 4.0, con el objetivo general de demostrar su capacidad de trabajo a diferentes escalasy entornos, así como la automatización de tareas de inspección. Los cuatro artículos científicos que componen esta tesis doctoral han demostrado cómo las distintas geotecnologías empleadas permiten trabajar tanto a escalas grandes, como en el caso de la fotogrametría de rango cercano y el PMMS, como a escalas pequeñas, mediante el uso de teledetección. Otro de los objetivos generales fue explorar diferentes entornos industriales para resaltar la alta adaptabilidad de las geotecnologías. En concreto, se han estudiado parques fotovoltaicos y una sala de máquinas demostrando la versatilidad de las geotecnologías tanto en escenarios interiores como exteriores. Por último, se ha demostrado mediante el desarrollo de diferentes aplicaciones como es posible automatizar las tareas de inspección. En cuanto a los objetivos específicos marcados se detallan a continuación.

El primer objetivo planteado en la presente tesis doctoral fue la creación de una herramienta orientada a la realización del control de calidad externo de soldaduras. La herramienta desarrollada bajo el nombre de WELDMAP integra todo el proceso fotogramétrico, orientado a la obtención de modelos de nubes de puntos 3D de las soldaduras, con algoritmos desarrollados específicamente para realizar el control de calidad sobre las nubes de puntos.

La validación del software WELDMAP, con diferentes tipos de soldaduras, concluyó que el uso de la fotogrametría para generar modelos 3D garantiza una mejor resolución y precisión en comparación con los métodos basados en la inspección visual de las soldaduras utilizando dispositivos manuales. A su vez, los algoritmos de segmentación y clasificación semántica permiten realizar un registro completo de planos y del cordón de soldadura, y los algoritmos de control de calidad permiten la detección de defectología de forma automática.

El segundo objetivo marcado fue la validación de la usabilidad de un sistema de escaneado portátil para la optimización en la toma de datos en las tareas de inspección de instalaciones fluidomecanicas. Los resultados han demostrado que el rendimiento del PMMS se encuentra dentro de las especificaciones técnicas del fabricante, siendo esta suficiente para una gran parte de instalaciones industriales. La desviación en la estimación del diámetro en las tuberías analizadas en términos relativos es mayor para los tubos de menor diámetro y mejor para los tubos de mayor diámetro, manteniéndose siempre en torno a la precisión centimétrica dada por el fabricante de Zeb-Revo. Esta desviación nos da una estimación de las aplicaciones industriales en las cuales puede tener cabida el uso de PMMS. En los planos verticales se encontró un sesgo y se identificaron diferencias en términos de resolución entre los dos dispositivos en la identificación de elementos específicos.

El tercer objetivo fue la detección automática de puntos calientes en paneles fotovoltaicos. La herramienta resultado del estudio llamada SunMap, mediante un tratamiento fotogramétrico riguroso, la aplicación de los algoritmos desarrollados para la extracción automática de la geometría de la planta fotovoltaica, así como de la corrección de las imágenes termográficas y análisis estadísticos, han permitido la detección precisa de puntos calientes. La validación en dos plantas fotovoltaicas diferentes ha demostrado que tanto la geometría de los paneles como las patologías detectadas están correctamente georreferenciadas y esto permite que el informe generado sea una herramienta valiosa para la inspección y mantenimiento de plantas fotovoltaicas.

El cuarto objetivo fue el desarrollo de una IDE para la monitorización de vegetación inusual y cuerpos de agua en el entorno de plantas fotovoltaicas. Mediante el análisis de seis plantas fotovoltaicas ubicadas en distintas zonas de España, sometidas por tanto a diferentes condiciones, se certificó la utilidad de la herramienta INSPECTORMAP para la realización de un mantenimiento sin inspecciones periódicas *in situ*, mediante el uso de imágenes satelitales para calcular índices espectrales mediante los cuales detectar zonas que necesitan mantenimiento. La herramienta permite a los operarios de mantenimiento conocer la actividad vegetal y el crecimiento de masas de agua en el entorno de las plantas fotovoltaicas realizando las tareas de mantenimiento únicamente cuando sea necesario y centrando el mantenimiento en las zonas afectadas. Sin embargo, se debe considerar que en ciertos casos las superficies cuantificadas no son lo suficientemente precisas, especialmente en imágenes de menor resolución. Se ha comprobado como el índice NDWI proporciona una estimación más precisa de las áreas afectadas en comparación con otros índices como el SWI, que tiende a sobrestimar las áreas con presencia de agua.

6.2. Perspectivas futuras

Hay ciertas cuestiones surgidas durante la realización de la tesis doctoral que no pudieron ser abordadas y posiblemente serán objeto de estudio en el futuro. Por otra parte, la rápida aparición de nuevas tecnologías y herramientas hacen posible la mejora de las soluciones planteadas mediante la implementación de nuevos algoritmos o la mejora de los datos capturados mediante la utilización de sensores más avanzados. De esta forma se establecen los siguientes puntos como perspectivas futuras:

- En el caso de las soldaduras se espera poder trabajar con imágenes de otras longitudes de onda y con otros materiales, incorporando técnicas de registro multimodal junto con la aplicación de técnicas de inteligencia artificial para tareas de inspección de calidad que permitan detectar tipos adicionales de defectos. En el caso de *matching* multimodal han aparecido diferentes algoritmos como D2Net[48] o R2D2[49] que permiten la detección y correspondencia de características en condiciones muy desfavorables gracias al uso de *Deep Learning* y que ya han sido incorporados y testeados en la herramienta PhotoMatch[50].

- En la inspección de instalaciones industriales con PMMS, futuros trabajos abordarán la mejora de los procesos de alineación que permita obtener una respuesta al problema del sesgo.

- La detección de patologías en paneles fotovoltaicos se limitó a los puntos calientes pero existen otros tipos de patologías descritos en estándar IEC TS 62446-3[51] como las debidas a suciedad, la rotura del cristal de un módulo o la anomalía de área extendida que habría que detectar. La inclusión de técnicas de *Deep Learning*, utilizando información geométrica y radiométrica como datos de entrada, podrían mejorar la robustez y eficiencia de la detección de patologías y permitir distinguir el tipo concreto.

- En la inspección mediante imágenes satélite de plantas fotovoltaicas, en el caso concreto de las ubicadas en desiertos, las dunas pueden ser un problema que afecte a las instalaciones. El uso de teledetección para generar MDT permitiría ver la evolución a lo largo del tiempo de las dunas y anticipar el mantenimiento en consecuencia. La puesta en orbita de Landsat-9, cuyo sensor OLI 2 (*Operational Land Imager* 2) transmite los datos en 14 bits proporcionando información adicional y útil para objetivos oscuros[52], puede mejorar la detección de masas de agua.

Bibliografía

[1] Ana Cachada y col. «Maintenance 4.0: Intelligent and Predictive Maintenance System Architecture». En: *2018 IEEE 23rd International Conference on Emerging Technologies and Factory Automation (ETFA)*. IEEE, sep. de 2018. DOI: 10.1109/etfa.2018.8502489. URL: https://doi.org/10.1109/etfa.2018.8502489.

[2] R Keith Mobley. *An introduction to predictive maintenance*. Elsevier, 2002.

[3] P. Poor, J. Basl y D. Zenisek. «Predictive Maintenance 4.0 as next evolution step in industrial maintenance development». En: *2019 International Research Conference on Smart Computing and Systems Engineering (SCSE)*. IEEE, mar. de 2019. DOI: 10.23919/scse.2019.8842659. URL: https://doi.org/10.23919/scse.2019.8842659.

[4] Heiner Lasi y col. «Industry 4.0». En: *Business & Information Systems Engineering* 6.4 (jun. de 2014), págs. 239-242. DOI: 10.1007/s12599-014-0334-4. URL: https://doi.org/10.1007/s12599-014-0334-4.

[5] Harry J. Gray. «The New Technologies: An Industrial Revolution». En: *Journal of Business Strategy* 5.2 (mar. de 1984), págs. 83-85. DOI: 10.1108/eb039061. URL: https://doi.org/10.1108/eb039061.

[6] Praveen Kumar Reddy Maddikunta y col. «Industry 5.0: A survey on enabling technologies and potential applications». En: *Journal of Industrial Information Integration* 26 (mar. de 2022), pág. 100257. DOI: 10.1016/j.jii.2021.100257. URL: https://doi.org/10.1016/j.jii.2021.100257.

[7] Jiewu Leng y col. «Industry 5.0: Prospect and retrospect». En: *Journal of Manufacturing Systems* 65 (oct. de 2022), págs. 279-295. DOI: 10.1016/j.jmsy.2022.09.017. URL: https://doi.org/10.1016/j.jmsy.2022.09.017.

[8] Sabine Pfeiffer. «The Vision of "Industrie 4.0" in the Making—a Case of Future Told, Tamed, and Traded». En: *NanoEthics* 11.1 (ene. de 2017), págs. 107-121. DOI: 10.1007/s11569-016-0280-3. URL: https://doi.org/10.1007/s11569-016-0280-3.

[9] Giacomo Büchi, Monica Cugno y Rebecca Castagnoli. «Smart factory performance and Industry 4.0». En: *Technological Forecasting and Social Change* 150 (ene. de 2020), pág. 119790. DOI: 10.1016/j.techfore.2019.119790. URL: https://doi.org/10.1016/j.techfore.2019.119790.

[10] Michael Rüßmann y col. «Industry 4 . 0 : The Future of Productivity and Growth in Manufacturing Industries April 09». En: 2016.

[11] Gizem Erboz. «How To Define Industry 4.0: Main Pillars Of Industry 4.0». En: nov. de 2017.

[12] Cristian Adarve-Gómez y col. «A review of virtual reality videogames for job-training applications». En: *Revista Cintex* 24.1 (2019), págs. 64-70.

[13] Dimitrios Serpanos y Marilyn Wolf. «Industrial Internet of Things». En: *Internet-of-Things (IoT) Systems*. Springer International Publishing, nov. de 2017, págs. 37-54. DOI: 10.1007/978-3-319-69715-4_5. URL: https://doi.org/10.1007/978-3-319-69715-4_5.

[14] Waqas Ahmad y col. «Cyber Security in IoT-Based Cloud Computing: A Comprehensive Survey». En: *Electronics* 11.1 (dic. de 2021), pág. 16. DOI: 10.3390/electronics11010016. URL: https://doi.org/10.3390/electronics11010016.

[15] Ugur M. Dilberoglu y col. «The Role of Additive Manufacturing in the Era of Industry 4.0». En: *Procedia Manufacturing* 11 (2017), págs. 545-554. DOI: 10.1016/j.promfg.2017.07.148. URL: https://doi.org/10.1016/j.promfg.2017.07.148.

[16] David Romero y col. «The operator 4.0: Human cyber-physical systems & adaptive automation towards human-automation symbiosis work systems». En: *Advances in Production Management Systems. Initiatives for a Sustainable World: IFIP WG 5.7 International Conference, APMS 2016, Iguassu Falls, Brazil, September 3-7, 2016, Revised Selected Papers*. Springer. 2016, págs. 677-686.

[17] Álvaro Segura y col. «Visual computing technologies to support the Operator 4.0». En: *Computers & Industrial Engineering* 139 (ene. de 2020), pág. 105550. DOI: 10.1016/j.cie.2018.11.060. URL: https://doi.org/10.1016/j.cie.2018.11.060.

[18] Comité Técnico CEN/TC 319 Mantenimiento. *Mantenimiento. Terminología del mantenimiento*. Inf. téc. UNE, jul. de 2018.

[19] Bernard Dubuisson. *La photogrammétrie des plans topographiques et parcellaires*. Eyrolles, 1969.

[20] Pierre Gagnon. «From surveying to geomatics evaluation of education needs to adapt to a new paradigm (a canadian perspective)». En: *Geomatica* 50.3 (1996), págs. 269-286.

[21] ISO Central Secretary. *Geographic information/Geomatics – Qualification and certification of personnel*. Standard. International Organization for Standardization, nov. de 2004.

[22] M. Ehlers. «Geoinformatics and digital earth initiatives: a German perspective». En: *International Journal of Digital Earth* 1.1 (mar. de 2008), págs. 17-30. DOI: 10.1080/17538940701781975. URL: https://doi.org/10.1080/17538940701781975.

[23] Artur Krawczyk. «Proposal of Redefinition of the Terms Geomatics and Geoinformatics on the Basis of Terminological Postulates». En: *ISPRS International Journal of Geo-Information* 11.11 (nov. de 2022), pág. 557. DOI: 10.3390/ijgi11110557. URL: https://doi.org/10.3390/ijgi11110557.

[24] V. Tournadre, M. Pierrot-Deseilligny y P. H. Faure. «UAV LINEAR PHOTOGRAMMETRY». En: *The International Archives of the Photogrammetry, Remote Sensing and Spatial Information Sciences* XL-3/W3 (ago. de 2015), págs. 327-333. DOI: 10.5194/isprsarchives-xl-3-w3-327-2015. URL: https://doi.org/10.5194/isprsarchives-xl-3-w3-327-2015.

[25] Mike R. James y Stuart Robson. «Mitigating systematic error in topographic models derived from UAV and ground-based image networks». En: *Earth Surface Processes and Landforms* 39.10 (jun. de 2014), págs. 1413-1420. DOI: 10.1002/esp.3609. URL: https://doi.org/10.1002/esp.3609.

[26] Julián Tomaštík y col. «UAV RTK/PPK Method—An Optimal Solution for Mapping Inaccessible Forested Areas?» En: *Remote Sensing* 11.6 (mar. de 2019), pág. 721. DOI: 10.3390/rs11060721. URL: https://doi.org/10.3390/rs11060721.

[27] S. Umeyama. «Least-squares estimation of transformation parameters between two point patterns». En: *IEEE Transactions on Pattern Analysis and Machine Intelligence* 13.4 (abr. de 1991), págs. 376-380. DOI: 10.1109/34.88573. URL: https://doi.org/10.1109/34.88573.

[28] European Commission. *Earth observation: first Copernicus satellite Sentinel 1A*. 2014. URL: https://ec.europa.eu/commission/presscorner/detail/en/MEMO_14_251 (visitado 25-03-2023).

[29] Mostafa Elhashash, Hessah Albanwan y Rongjun Qin. «A Review of Mobile Mapping Systems: From Sensors to Applications». En: *Sensors* 22.11 (jun. de 2022), pág. 4262. DOI: 10.3390/s22114262. URL: https://doi.org/10.3390/s22114262.

[30] ISO Central Secretary. *Geographic information — Web map server interface*. Standard. International Organization for Standardization, dic. de 2005.

[31] ISO Central Secretary. *Geographic information — Services*. Standard. International Organization for Standardization, ene. de 2016.

[32] ISO Central Secretary. *Geographic information — Geography Markup Language (GML) — Part 1: Fundamentals*. Standard. International Organization for Standardization, ene. de 2020.

[33] M. Rodríguez-Martín y col. «Procedure for quality inspection of welds based on macro-photogrammetric three-dimensional reconstruction». En: *Optics & Laser Technology* 73 (oct. de 2015), págs. 54-62. DOI: 10.1016/j.optlastec.2015.04.011. URL: https://doi.org/10.1016/j.optlastec.2015.04.011.

[34] Leena Matikainen y col. «Remote sensing methods for power line corridor surveys». En: *ISPRS Journal of Photogrammetry and Remote Sensing* 119 (sep. de 2016), págs. 10-31. DOI: 10.1016/j.isprsjprs.2016.04.011. URL: https://doi.org/10.1016/j.isprsjprs.2016.04.011.

[35] Vidya Sudevan, Amit Shukla y Hamad Karki. «Current and Future Research Focus on Inspection of Vertical Structures in Oil and Gas Industry». En: *2018 18th International Conference on Control, Automation and Systems (ICCAS)*. 2018, págs. 144-149.

[36] Javad Shahmoradi y col. «A Comprehensive Review of Applications of Drone Technology in the Mining Industry». En: *Drones* 4.3 (jul. de 2020), pág. 34. DOI: 10.3390/drones4030034. URL: https://doi.org/10.3390/drones4030034.

[37] Sungjae Lee y Yosoon Choi. «Reviews of unmanned aerial vehicle (drone) technology trends and its applications in the mining industry». En: *Geosystem Engineering* 19.4 (mar. de 2016), págs. 197-204. DOI: 10.1080/12269328.2016.1162115. URL: https://doi.org/10.1080/12269328.2016.1162115.

[38] Claudia Buerhop y col. «aIR-PV-check: A quality inspection of PV-power plants without operation interruption». En: *2016 IEEE 43rd Photovoltaic Specialists Conference (PVSC)*. IEEE, jun. de 2016. DOI: 10.1109/pvsc.2016.7749909. URL: https://doi.org/10.1109/pvsc.2016.7749909.

[39] Yahya Zefri y col. «Thermal Infrared and Visual Inspection of Photovoltaic Installations by UAV Photogrammetry—Application Case: Morocco». En: *Drones* 2.4 (nov. de 2018), pág. 41. DOI: 10.3390/drones2040041. URL: https://doi.org/10.3390/drones2040041.

[40] Arkadiusz Tyszko, Tomasz Temlin y Stanislaw Oszczak. «GNSS systems in vehicle fleet management». En: *Transport Problems* 2.2 (2007), págs. 11-16.

[41] Niels Joubert, Tyler G. R. Reid y Fergus Noble. «Developments in Modern GNSS and Its Impact on Autonomous Vehicle Architectures». En: *2020 IEEE Intelligent Vehicles Symposium (IV)*. 2020, págs. 2029-2036. DOI: 10.1109/IV47402.2020.9304840.

[42] Veli Ilci y Charles Toth. «High Definition 3D Map Creation Using GNSS/IMU/LiDAR Sensor Integration to Support Autonomous Vehicle Navigation». En: *Sensors* 20.3 (feb. de 2020), pág. 899. DOI: 10.3390/s20030899. URL: https://doi.org/10.3390/s20030899.

[43] Joan-Cristian Padró y col. «Drone-Based Identification of Erosive Processes in Open-Pit Mining Restored Areas». En: *Land* 11.2 (ene. de 2022), pág. 212. DOI: 10.3390/land11020212. URL: https://doi.org/10.3390/land11020212.

[44] Phillip B. McKenna y col. «Remote Sensing of Mine Site Rehabilitation for Ecological Outcomes: A Global Systematic Review». En: *Remote Sensing* 12.21 (oct. de 2020), pág. 3535. DOI: 10.3390/rs12213535. URL: https://doi.org/10.3390/rs12213535.

[45] Jose F Llorens Benito y col. «A remote sensing based approach for the restoration of an open-cast coal mine site in Spain». En: ene. de 2000, págs. 491-496. ISBN: 90-5809-096-5.

[46] Paweł Hawryło y col. «Landscape monitoring of post-industrial areas using LiDAR and GIS technology». En: *Geodesy and Cartography* 64.1 (jun. de 2015), págs. 125-137. DOI: 10.1515/geocart-2015-0010. URL: https://doi.org/10.1515/geocart-2015-0010.

[47] Consejo de Gobierno de la Universidad de Salamanca. *Reglamento de Doctorado de la Universidad de Salamanca*. Inf. téc. Universidad de Salamanca, ene. de 2015.

[48] Mihai Dusmanu y col. *D2-Net: A Trainable CNN for Joint Detection and Description of Local Features*. 2019. DOI: 10.48550/ARXIV.1905.03561. URL: https://arxiv.org/abs/1905.03561.

[49] Jerome Revaud y col. *R2D2: Repeatable and Reliable Detector and Descriptor*. 2019. DOI: 10.48550/ARXIV.1906.06195. URL: https://arxiv.org/abs/1906.06195.

[50] Esteban Ruiz de Oña y col. «PhotoMatch: An Open-Source Tool for Multi-View and Multi-Modal Feature-Based Image Matching». En: *Applied Sciences* 13.9 (abr. de 2023), pág. 5467. DOI: 10.3390/app13095467. URL: https://doi.org/10.3390/app13095467.

[51] IEC. *Photovoltaic (PV) systems - Requirements for testing, documentation and maintenance - Part 3: Photovoltaic modules and plants - Outdoor infrared thermography*. Inf. téc. The International Electrotechnical Commission (IEC), jun. de 2017.

[52] *Landsat 9 Instruments*. Dic. de 2022. URL: https://landsat.gsfc.nasa.gov/satellites/landsat-9/landsat-9-instruments/.

[53] David G. Lowe. «Distinctive Image Features from Scale-Invariant Keypoints». En: *International Journal of Computer Vision* 60.2 (nov. de 2004), págs. 91-110. DOI: 10.1023/b:visi.0000029664.99615.94. URL: https://doi.org/10.1023/b:visi.0000029664.99615.94.

Apéndices

Apéndice A

Indexación y factor de impacto de las publicaciones

Apéndice A

Indexación y factor de impacto de las publicaciones

En este apéndice se incluyen las principales medidas de impacto de las revistas en las cuales se han publicado los artículos científicos de esta Tesis Doctoral. Estas medidas de impacto se han obtenido del *Journal Citation Reports* (JCR), una publicación anual realizada por *Clarivate Analytics* que proporciona una serie de medidas del impacto y calidad de las revistas científicas. Se detallan a continuación las principales métricas.

- ***Journal Impact Factor* (JIF)**: El factor de impacto es una métrica a nivel de revista calculada a partir de los datos indexados en la *Web of Science Core Collection*. El JIF divide las citas recibidas por una revista entre el recuento de sus artículos y/o reseñas publicadas, reflejando el impacto de las citas del contenido reciente de la revista.

- ***Journal Citation Indicator* (JCI)**: media del *Category Normalized Citation Impact* (CNCI) de los elementos citables (artículos y revisiones) publicados por una revista en los últimos tres años. El JCI medio de una categoría es 1.

- **Citas totales**: Número total de veces que una revista ha sido citada por todas las revistas incluidas en la base de datos JCR.

- **Distribución de citas**: La Distribución de citas muestra la frecuencia con la que los artículos publicados en el año o los dos años anteriores fueron citados en el año de datos del JCR.

- ***Eigenfactor Score***: Refleja la densidad de la red de citas en torno a la revista utilizando 5 años de contenidos citados por el Año en curso. Considera tanto el número de citas como la fuente de esas citas, de modo que las fuentes muy citadas influirán en la red más que las fuentes menos citadas. El cálculo del factor propio no incluye las autocitas de la revista.

- **Normalized Eigenfactor**: *Eigenfactor Score* Score normalizado.

- **Article influence score**: Normaliza la puntuación del factor propio en función del tamaño acumulado de la revista citada en los cinco años anteriores. La puntuación media de la influencia de cada artículo es de 1. Una puntuación superior a 1 indica que cada artículo de la revista tiene una influencia superior a la media.

- **Factor de impacto quinquenal**: Media de veces que los artículos de la revista publicados en los últimos cinco años han sido citados en el año JCR. Se calcula dividiendo el número de citas en el año JCR por el número total de artículos publicados en los cinco años anteriores.

- **Índice de inmediatez**: Número de citas de la revista en el año en curso que hacen referencia a contenidos de ese mismo año.

A.1.   Applied Sciences

Applied Sciences es una revista científica quincenal de acceso abierto revisada por pares que cubre todos los aspectos de la física aplicada, la química aplicada, la biología aplicada y las ciencias de la ingeniería, el medio ambiente y la tierra. Fue creada en 2011 y es publicada por MDPI.

En *Applied Sciences* se han publicado los artículos *"WELDMAP: A Photogrammetric Suite Applied to the Inspection of Welds"* y *ÏNSPECTORMAP: A Spatial Data Infrastructure Applied to the Maintenance of Solar Plants Using Free Satellite Imagery"*.

Revista	Applied Sciences
Editorial	MDPI
EISSN	2076-3417
Factor de impacto (2021)	2.838
Ranking	39/92
Cuartil	Q2

Tabla A.1: Principales medidas de impacto para Applied Sciences
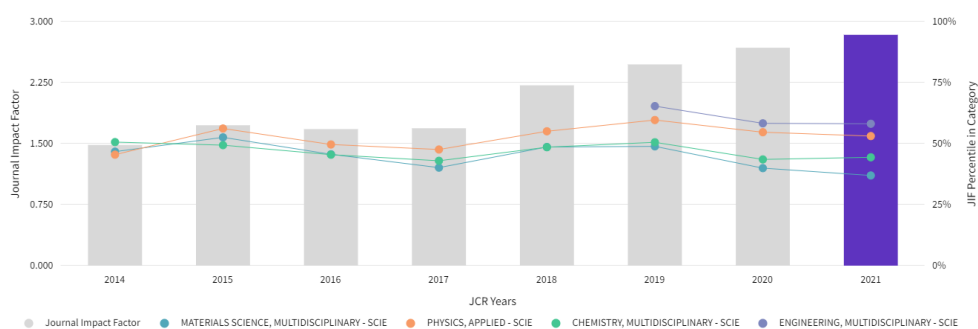
Figura A.1: **Journal Impact Factor (JIF)**: 2.838
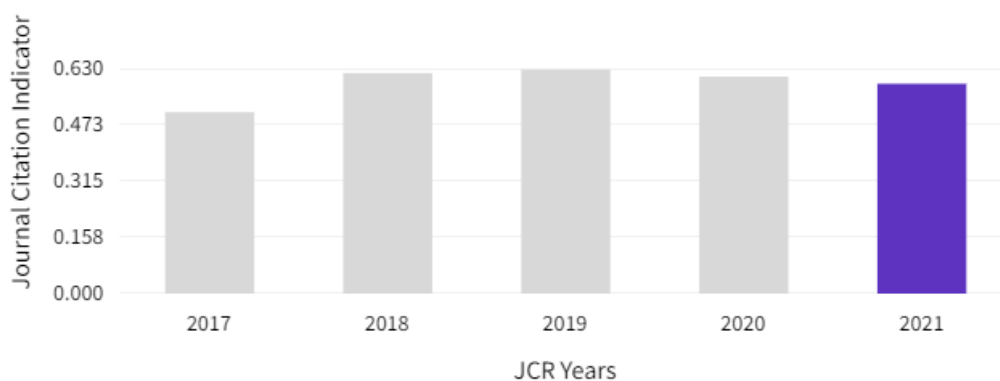

Figura A.2: **Journal Citation Indicator (JCI)**: 0.59
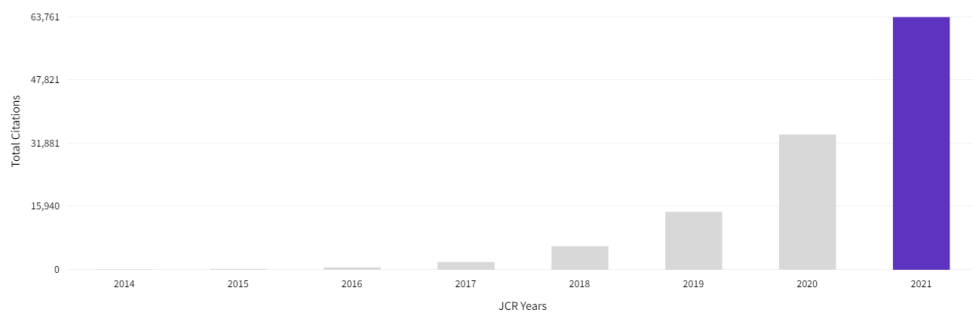

Figura A.3: **Total Citations**: 63761
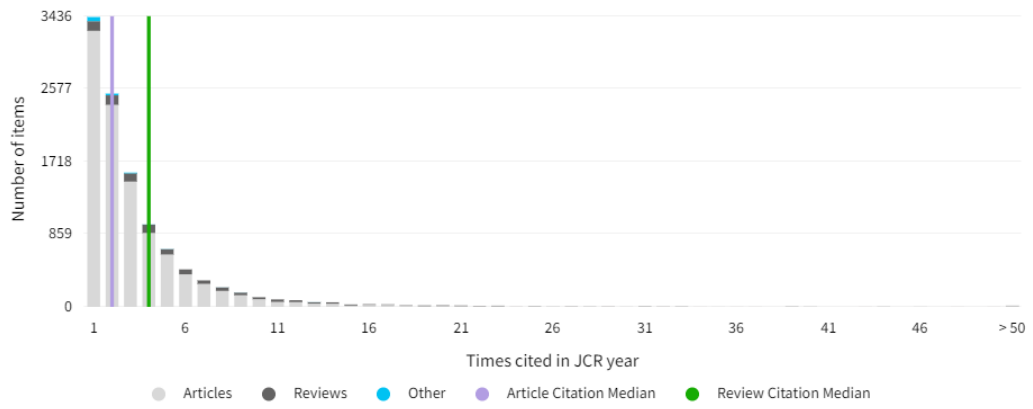
Figura A.4: **Citation Distribution**
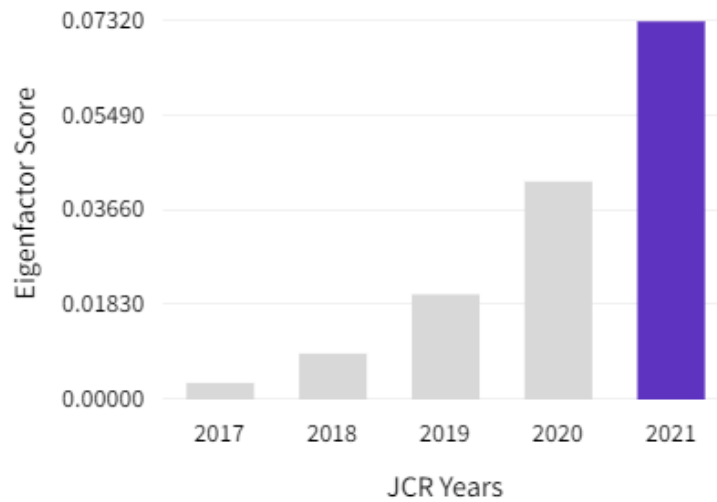
Figura A.5: **Eigenfactor score**: 0.07320
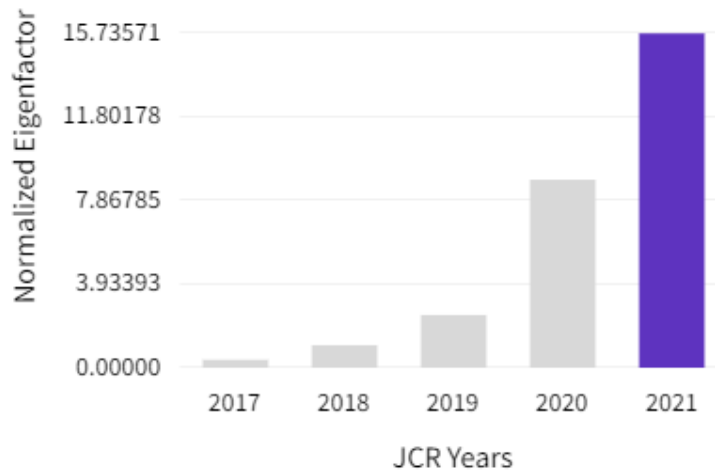
Figura A.6: **Normalized Eigenfactor**: 15.73571
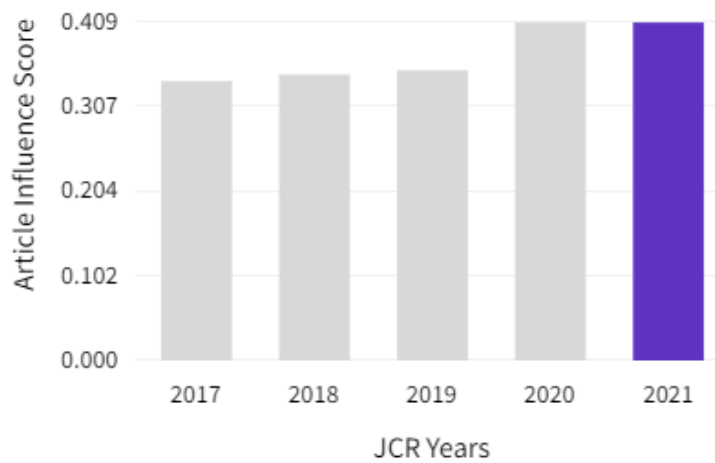
Figura A.7: **Article influence score**: 0.409
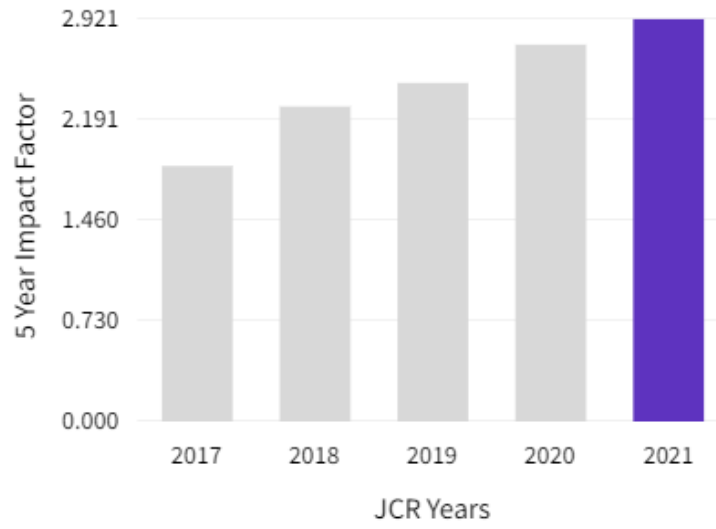
Figura A.8: **5 year Impact Factor**: 2.921
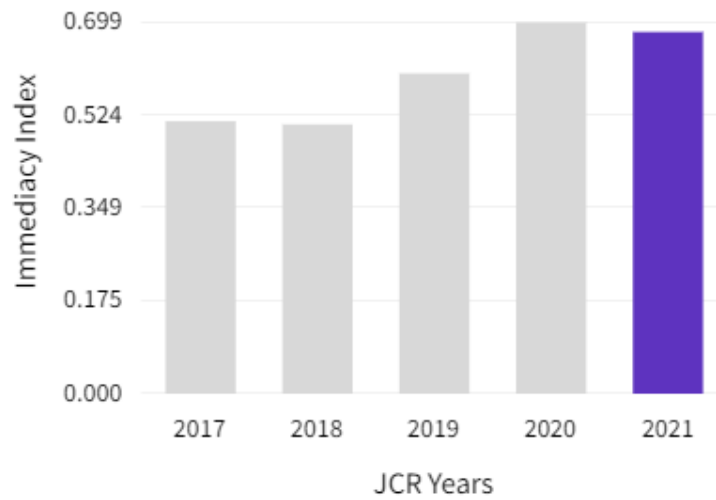
Figura A.9: **Immediacy Index**: 0.681

A.2.   Remote Sensing

Remote Sensing es una revista académica bimensual de acceso abierto revisada por pares que se centra en la investigación relativa a la teledetección y otras disciplinas de la geografía. Fue creada en 2009 y es publicada por MDPI.

En *Remote Sensing* se ha publicado el artículo "*Validation of Portable Mobile Mapping System for Inspection Tasks in Thermal and Fluid–Mechanical Facilities*".

Revista	Remote Sensing
Editorial	MDPI
EISSN	2072-4292
Factor de impacto (2021)	5.349
Ranking	11/34
Cuartil	Q2

Tabla A.2: Principales medidas de impacto para Remote Sensing
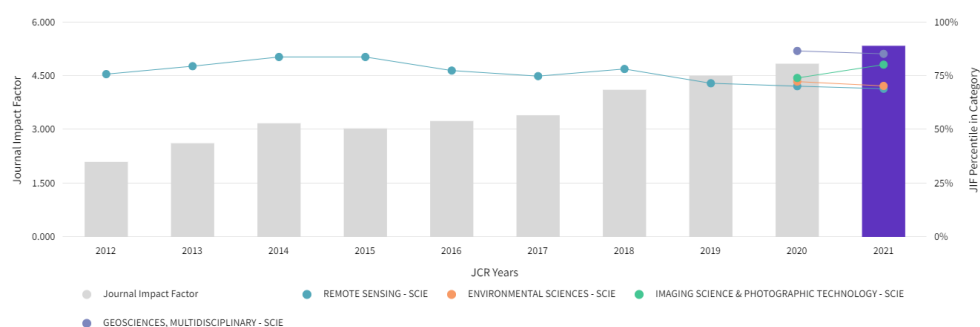
Figura A.10: **Journal Impact Factor (JIF)**: 5.349
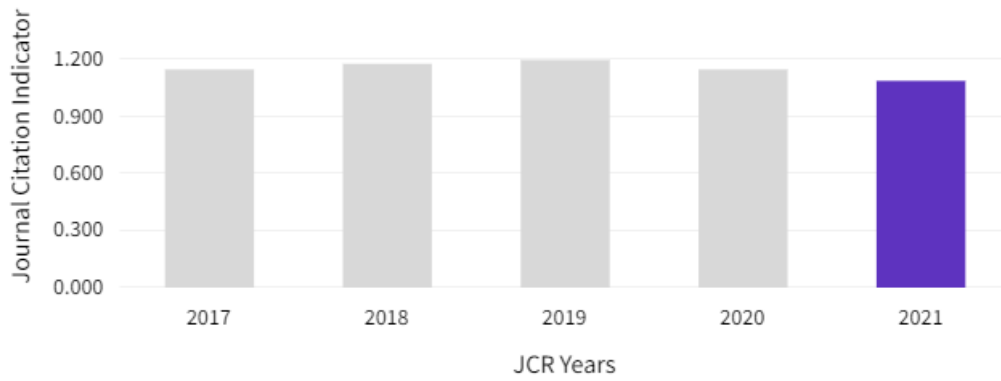
Figura A.11: **Journal Citation Indicator (JCI)**: 1.09
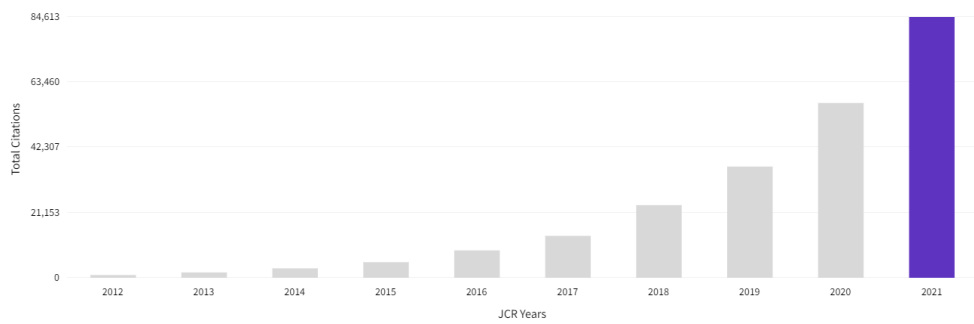
Figura A.12: **Total Citations**: 84613
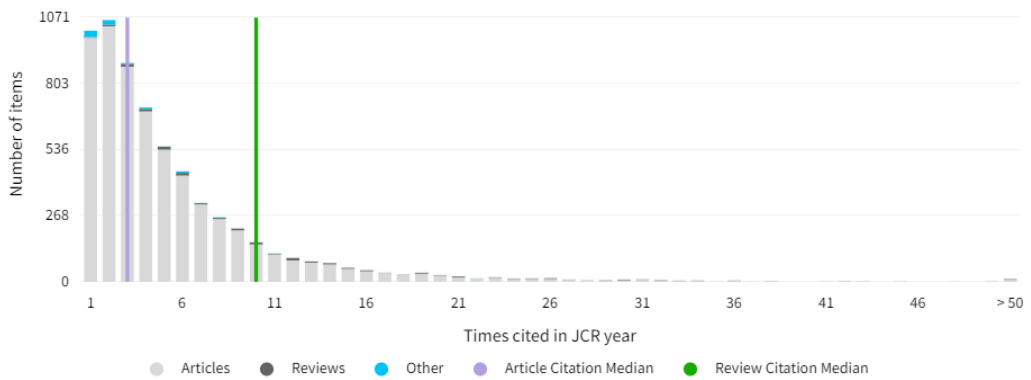
Figura A.13: **Citation Distribution**
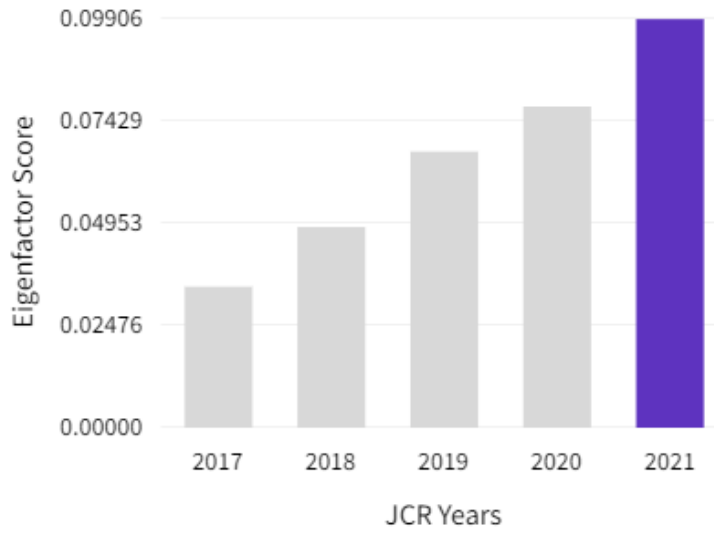
Figura A.14: **Eigenfactor score**: 0.09906
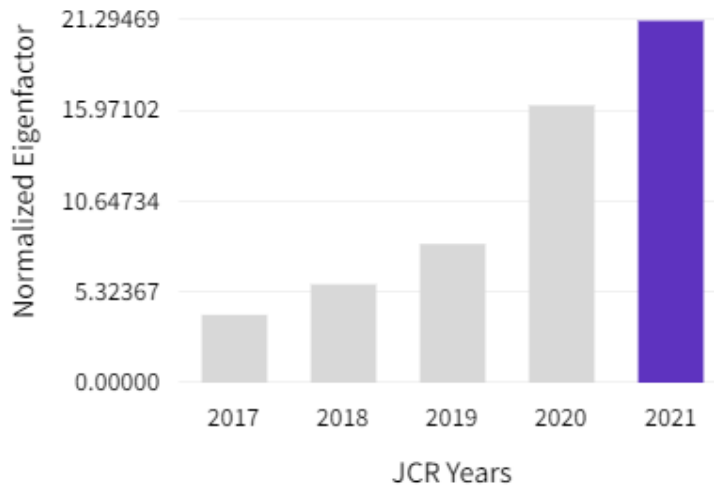
Figura A.15: **Normalized Eigenfactor**: 21.29469
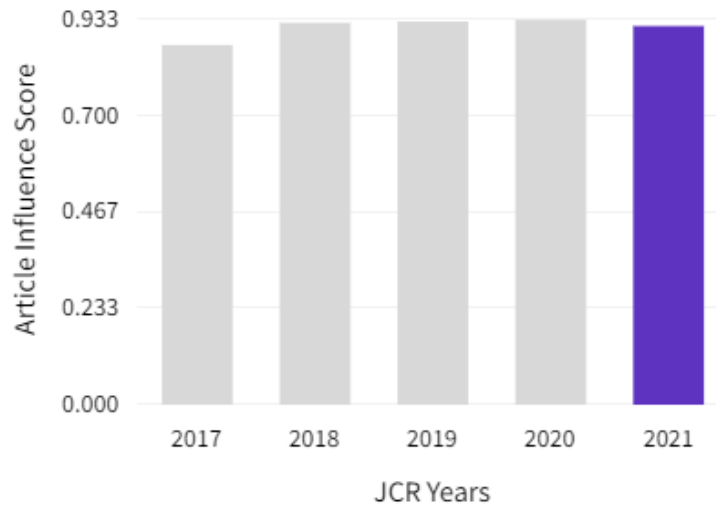
Figura A.16: **Article influence score**: 0.918
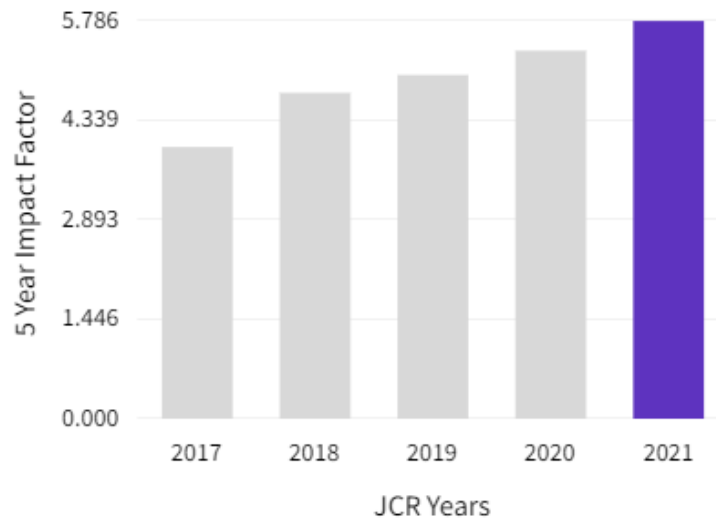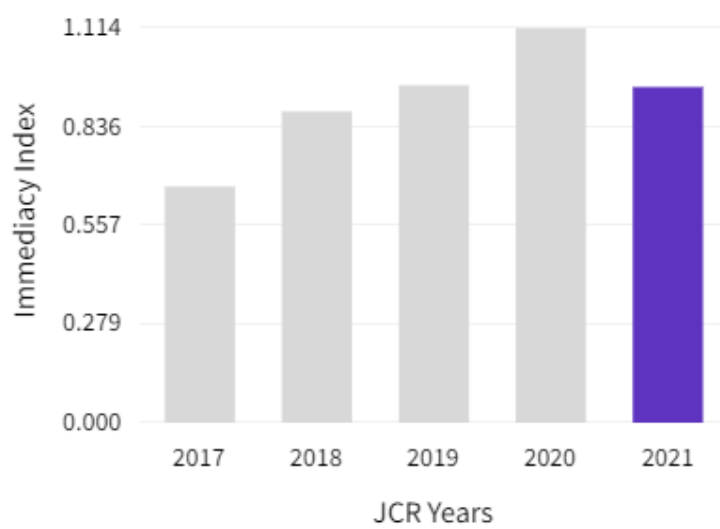

Figura A.17: **5 year Impact Factor**: 5.786

Figura A.18: **Immediacy Index**: 0.948

A.3.   Drones

Drones es una revista internacional de acceso abierto, revisada por pares y publicada mensualmente en línea por MDPI. La revista se centra en el diseño y las aplicaciones de los drones, incluidos los vehículos aéreos no tripulados (UAV), los sistemas de aeronaves no tripuladas (UAS) y los sistemas de aeronaves pilotadas por control remoto (RPAS), etc.

En *Drones* se ha publicado el artículo *"SunMap: Towards Unattended Maintenance of Photovoltaic Plants Using Drone Photogrammetry"*.

Revista	Drones
Editorial	MDPI
EISSN	2504-446X
Factor de impacto (2021)	5.532
Ranking	10/34
Cuartil	Q2

Tabla A.3: Principales medidas de impacto para Drones
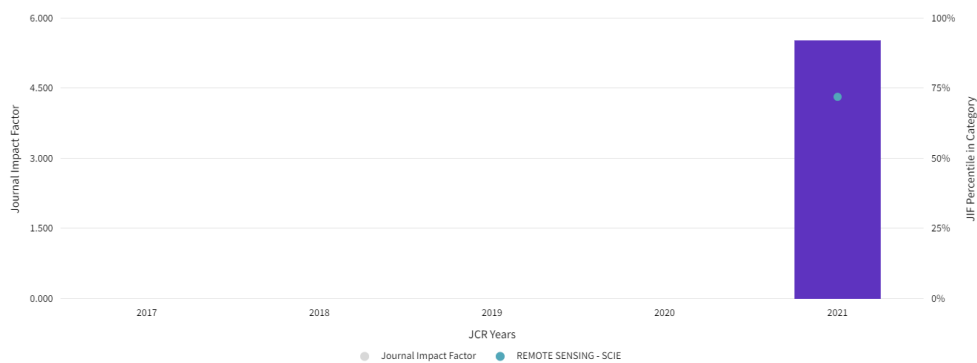
Figura A.19: **Journal Impact Factor (JIF)**: 5.532
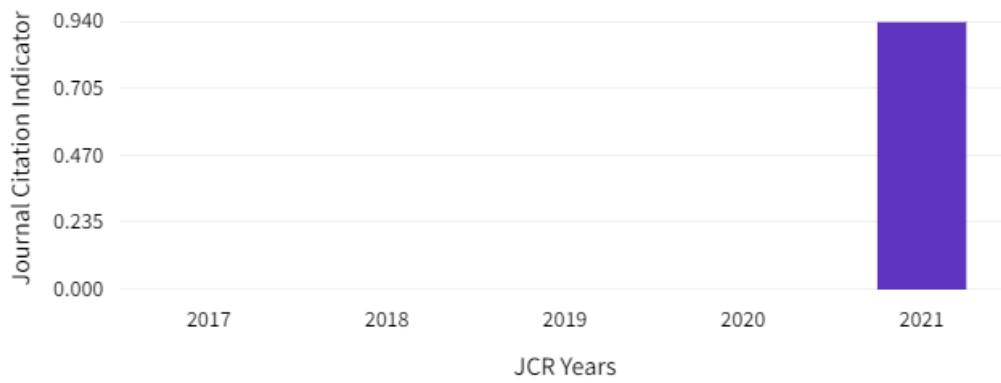
Figura A.20: **Journal Citation Indicator (JCI)**: 0.94

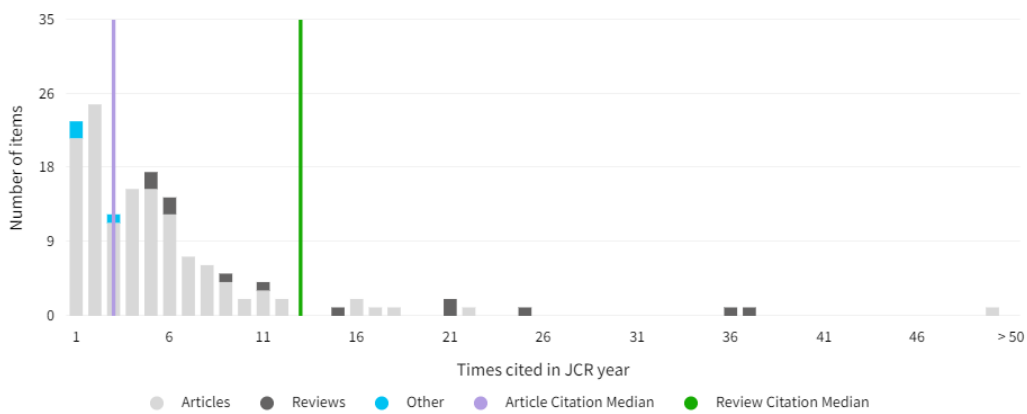Figura A.21: **Total Citations**: 1268
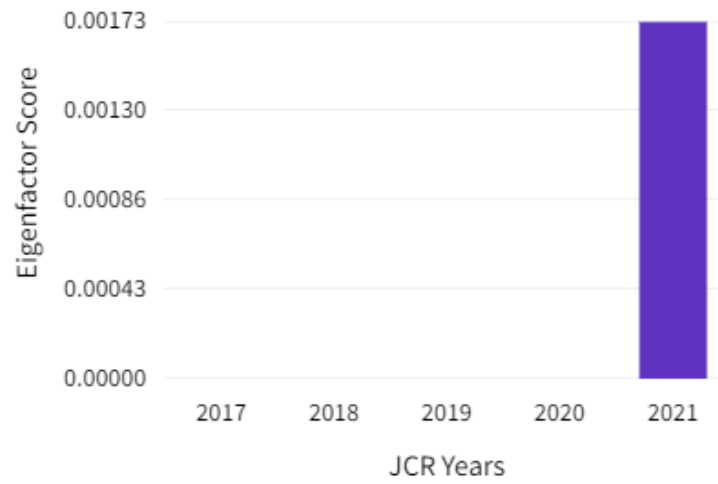

Figura A.22: **Citation Distribution**

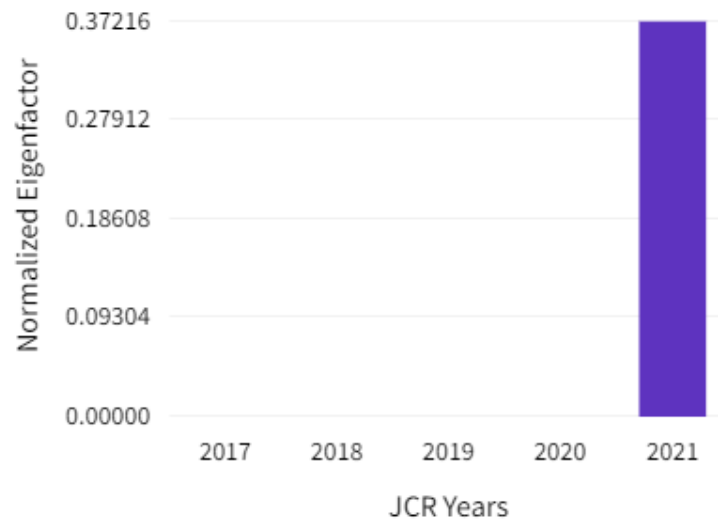Figura A.23: **Eigenfactor score**: 0.00173

Figura A.24: **Normalized Eigenfactor**: 0.37216

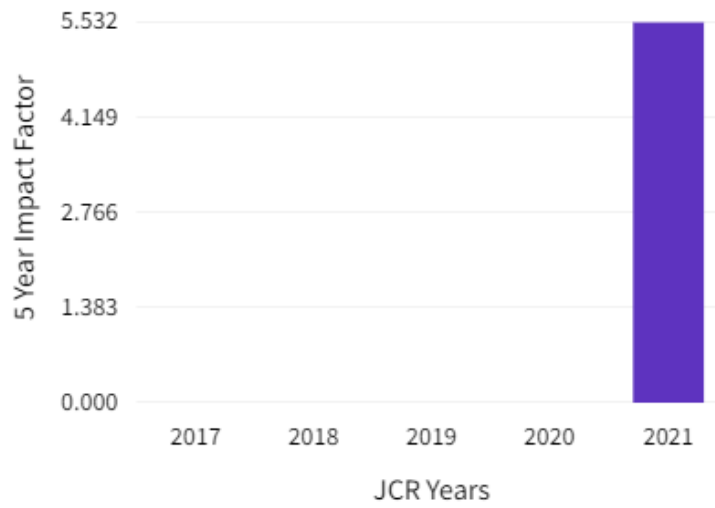Figura A.25: **Article influence score**: 0.890

Figura A.26: **5 year Impact Factor**: 5.532

Figura A.27: **Immediacy Index**: 0.897

Apéndice B

Software

Apéndice B

Software

B.1. TidopLib

TidopLib es una librería escrita en C++ moderno, distribuida bajo licencia de software libre *GNU Lesser General Public License v3.0* (LGPL 3.0), que se emplea como base en el resto de desarrollos de esta tesis doctoral.

TidopLib consta de los siguientes módulos:

- **Core**: Módulo principal de la librería que contiene utilidades para la gestión de la consola, *parseo* de comandos, gestión de mensajes, concurrencia, etc.

- **FeatMatch:**: Incluye algoritmos de detección y extracción de características, *matching* y utilidades de lectura y escritura.

- **Geom**: Módulo que engloba entidades geométricas, algoritmos para calcular la intersección, el ángulo o la distancia entre entidades y transformaciones geométricas (afín, rotación, escalado, proyectiva, etc).

- **Graph**: Módulo que incluye entidades gráficas usadas en la lectura y escritura de formatos vectoriales, conversiones entre modelos de color y algoritmos de trazado de líneas.

- **Math**: Módulo de álgebra y estadística. Incluye operaciones con matrices y vectores, resolución de sistemas de ecuaciones lineales y diferentes sistemas de rotación, como matrices de rotación y cuaterniones, así como la transformación entre ellos.

- **Vect**: Módulo de lectura y escritura de formatos vectoriales (DWG, DXF, ShapeFile, etc.).

- **Img**: Módulo de lectura y escritura de los formatos ráster más habituales.

- **ImgProcess**: Contiene varios algoritmos para el filtrado de imágenes, operaciones morfológicas, transformación del modo de color, etc.

B.1.1. Dependencias

La librería se construye con CMake e incluye las siguientes dependencias:

- Boost: Las bibliotecas Boost C++ son una colección de bibliotecas modernas, multiplataforma, basadas en el estándar C++. El código fuente se publica bajo la licencia *Boost Software License*, que permite a cualquiera utilizar, modificar y distribuir las bibliotecas de forma gratuita.

- OpenCV(*Open Source Computer Vision Library*): Biblioteca de código abierto que incluye multitud de algoritmos de visión por ordenador.

- CUDA (*Compute Unified Device Architecture*): Plataforma de cálculo paralelo que cuenta con una API (interfaz de programación de aplicaciones) que permite utilizar las GPU (unidad de procesamiento gráfico) compatibles para el procesamiento de propósito general.

- Gdal (*Geospatial Data Abstraction Library*): es Biblioteca de software publicada bajo la licencia X/MIT por la *Open Source Geospatial Foundation*. Entre sus utilidades esta la lectura y escritura de formatos de datos geoespaciales ráster y vectoriales, y la transformación entre sistemas de coordenadas.

La librería está disponible para la descarga en el repositorio:

https://github.com/TIDOP-USAL/tidoplib.git

B.2. GRAPHOS 2

GRAPHOS (*InteGRAted PHOtogrammetric Suite*) B.1 es un software foto-gramétrico para reconstrucción 3D distribuido bajo licencia LGPL 3.0 y desarrollado en el lenguaje de programación C++ empleando el *framework* de desarrollo Qt. La ultima versión del *software* es la 2.0, la cual se encuentra disponible para la descarga en el siguiente enlace:
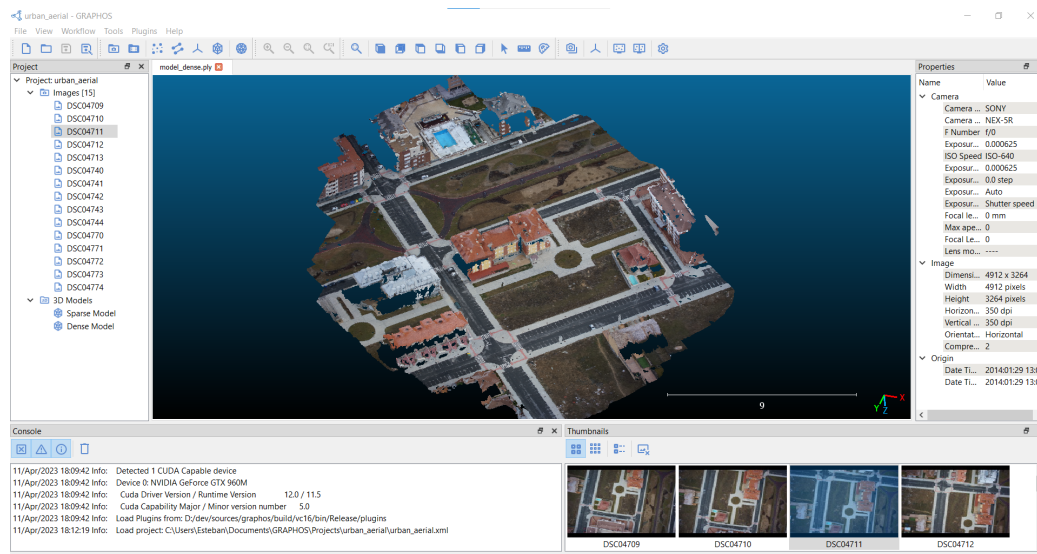
https://github.com/TIDOP-USAL/graphos/releases

Figura B.1: GRAPHOS 2

B.2.1. Arquitectura del software

El software se ha implementado mediante componentes independientes para asegurar la reutilización del código y minimizar las dependencias. Cada componente es una librería independiente que se estructura siguiendo la arquitectura modelo vista presentador (MVP) adaptada a las peculiaridades del *framework* Qt. El patrón MVP de forma general está compuesto por:

- Un presentador, que es el responsable de toda la lógica de presentación, ocupándose este de la interacción con la vista y con el modelo.

- La vista, que representa la interfaz gráfica del programa y la interacción del usuario con la misma.

- El modelo, que es donde se centra toda la lógica de negocio de la aplicación. Se ocupa de las operaciones de lectura y escritura, del acceso a datos y de los cálculos o realización de tareas con los mismos.

En este caso, dada las características del *framework* de desarrollo Qt, se ha hecho alguna modificación al patrón MVP más habitual, en el que la vista mantiene una instancia del presentador. En este caso el Presentador recibe mediante inyección de dependencias las instancias de la vista y del modelo. Esto es posible debido a que la gestión de eventos en Qt se realiza mediante *signals* y*slots* con lo cual la comunicación de eventos de la vista al presentador se hace de esta forma y se consiguen eliminar las dependencias de la Vista respecto del presentador.

El presentador recibe las señales de la vista y responde a las mismas, solicitando datos, la realización de tareas u operaciones al modelo. Con las respuestas del modelo, el presentador se ocupa de formatear correctamente los datos para actualizar la vista.

GRAPHOS incluye las librerías base *Graphos::Core* y *Graphos::Widget*, la interfaz principal de la aplicación y los siguientes componentes:

- **Graphos::CreateProject**: Creación de un nuevo proyecto.

- **Graphos::OpenProject**: Carga un proyecto existente.

- **Graphos::RecentProjects**: Permite abrir los últimos proyectos añadidos.

- **Graphos::SaveProject**: Guarda un proyecto.

- **Graphos::SaveProjectAs**: Guarda un proyecto con otro nombre o en otra ubicación.

- **Graphos::CloseProject**: Cierra el proyecto actual.

- **Graphos::ImageLoad**: Carga de imágenes en el proyecto.

- **Graphos::VideoLoad**: Carga un vídeo y permite la extracción de fotogramas del mismo para su procesamiento como imágenes.

- **Graphos::FeatExtract**: Extracción de características.

- **Graphos::FeatMatch**: Correspondencia de características.

- **Graphos::Orientation**: Orientación y autocalibración.

- **Graphos::Dense**: Generación de un modelo denso de nube de puntos.

- **Graphos::Mesh**: Generación de un mallado.

- **Graphos::Cameras**: Información sobre las cámaras (marca, modelo, tamaño del sensor) y parámetros de distorsión calculados. Permite la importación y exportación de la calibración de la cámara. Graphos::ImportCameras: Importación de las posiciones de las cámaras.

- **Graphos::Georeference**: Georreferenciación mediante puntos de control.

- **Graphos::Undistort**: Exportación de las imágenes corregidas de distorsión.

- **Graphos::Dtm**: Generación de un MDT o MDS.

- **Graphos::Orthophoto**: Mosaico de ortofotos.

- **Graphos::FeatViewer**: Visor de características extraídas en las imágenes.

- **Graphos::MatchViewer**: Visor de correspondencias de características entre pares de imágenes.

- **Graphos::Settings**: Configuración de la aplicación.

- **Graphos::Properties**: Propiedades de las imágenes (EXIF).

- **Graphos::About**: Información acerca de GRAPHOS y sus dependencias.

B.2.2. Dependencias

El software depende de las siguientes librerías y herramientas:

- **TidopLib**.

- **Qt**.

- **Colmap**: Librería SfM.

- **OpenMVS** (*Multi-View Stereo*): Librería para la reconstrucción estereoscópica multivista empleada en GRAPHOS como principal método de densificación.

- ***Patch-based Multi-view Stereo Software* (PMVS 2)**: Otro software MVS empleado como método alternativo de densificación.

- ***Shading-aware Multi-view Stereo* (SMVS)**: Software MVS empleado como método alternativo de densificación.

- ***Poisson Surface Reconstruction***: Librería que implementa el algoritmo de *Poisson* para la reconstrucción de superficies. Se emplea para la generación del mallado del modelo.

B.3. PhotoMatch

PhotoMatch es una herramienta para el testeo de diferentes algoritmos de mejora del contraste, extracción de características y estrategias de *matching* con conjuntos de datos multi-vista y multi-modales. Es un software libre de código abierto distribuido bajo licencia LGPL 3.0 y desarrollado en el lenguaje de programación C++ empleando el *framework* de desarrollo Qt. Se encuentra disponible para la descarga en el siguiente enlace:
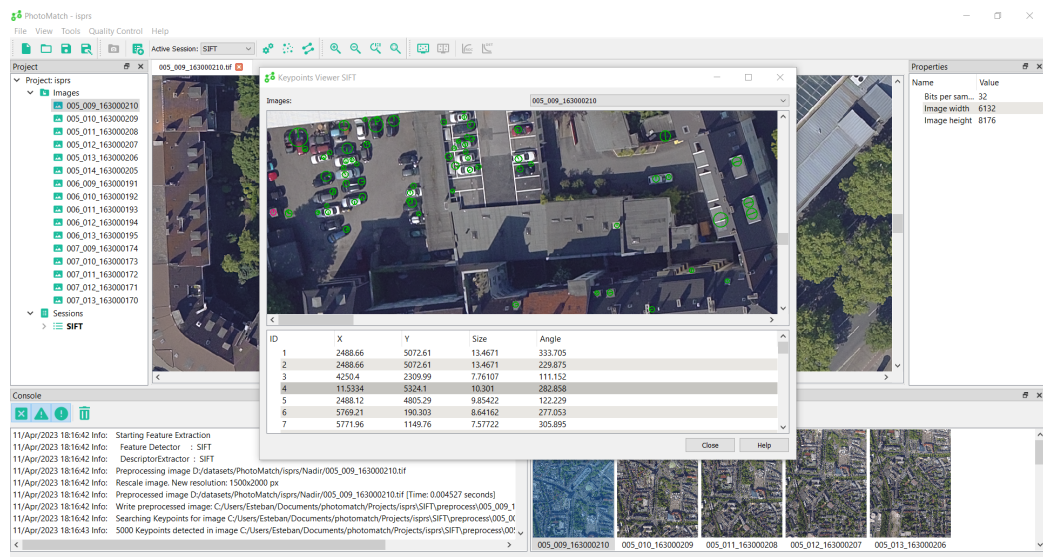
https://github.com/TIDOP-USAL/photomatch/releases

Figura B.2: PhotoMatch

B.3.1. Arquitectura del software

PhotoMatch sigue el mismo modelo basado en componentes siguiendo la arquitectura MVP tal y como se ha descrito para el software GRAPHOS.

B.3.2. Dependencias

El software depende de las siguientes librerías y herramientas:

- **TidopLib**.

- **Qt**.

- **pixkit**: Incluye diversos métodos de realce del contraste en imágenes.

- **OpenCV**.

B.4. WELDMAP

Software desarrollado en el artículo *"WELDMAP: A Photogrammetric Suite Applied to the Inspection of Welds"*. WELDMAP es un software de escritorio B.3, combinación de varios desarrollos previos incluyendo módulos de GRAPHOS y PhotoMatch, que permite la gestión de proyectos de inspección de soldaduras.
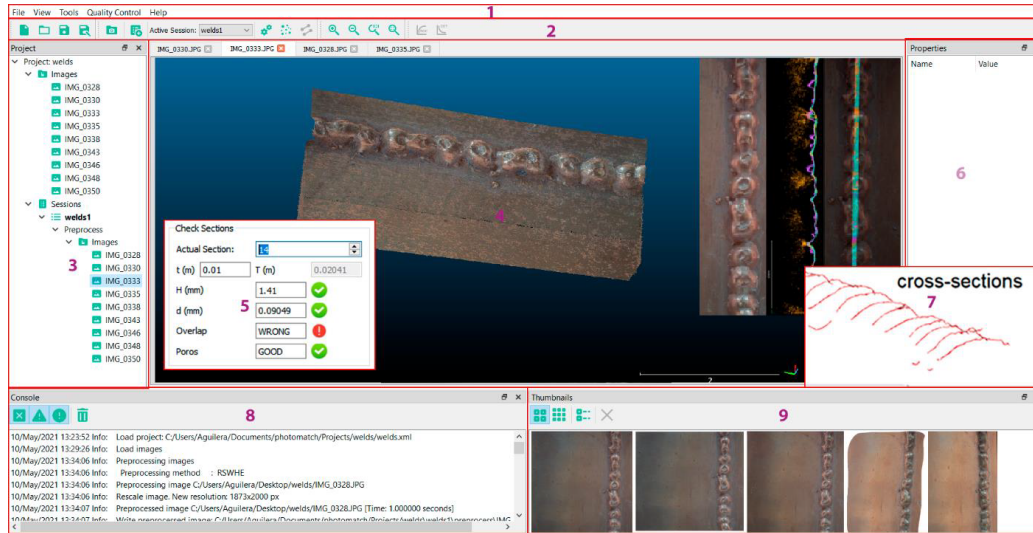

Figura B.3: WELDMAP

WELDMAP emplea la técnica SfM, la cual permite la reconstrucción 3D de un objeto o escena a partir de un conjunto de imágenes. El flujo de trabajo comienza con un preprocesado de las imágenes empleando algoritmos que permiten la mejora del contraste conservando los detalles de la imagen. Este paso previo permite que la extracción de características de la imagen ofrezca mejores resultados. Para la búsqueda de correspondencias de características entre las imágenes se ha empleado una estrategia de *matching* robusto, la cual permite la eliminación de correspondencias incorrectas mediante el filtrado por el test de ratio[53] y test geométricos basados en la matriz fundamental. Con los *matches* resultantes se realiza el registro de todas las imágenes, triangulación y ajuste de haces que permite obtener la posición y orientación de las cámaras, sus parámetros internos y un modelo ligero formado por los puntos resultantes del ajuste de haces. A partir de la orientación externa y los parámetros internos de la cámara se genera un modelo denso mediante la técnica MVS.

El siguiente paso en el flujo de trabajo de WELDMAP es la clasificación automática de la nube en placa izquierda, placa derecha y cordón. Posteriormente, se generan automáticamente las secciones transversales, cuyo análisis permite identificar los defectos objeto de estudio.

B.4.1. Arquitectura del software

WELDMAP sigue el mismo modelo basado en componentes siguiendo la arquitectura MVP tal y como se ha descrito para el software GRAPHOS.

B.5. SunMap

El software desarrollado en el artículo *"SunMap: Towards Unattended Maintenance of Photovoltaic Plants Using Drone Photogrammetry"* para el análisis de patologías en plantas fotovoltaicas es el resultado de la combinación del software GRAPHOS para el procesamiento fotogramétrico y el plugin de detección de patologías SunMap.

SunMap emplea la técnica SfM para la obtención de la autocalibración y orientación de las imágenes (tanto RGB como IRT). A partir de la reconstrucción 3D se genera una nube de puntos densa basada en la técnica MVS. Seguidamente, se obtienen diversos productos cartográficos que serán empleados en el proceso de detección de puntos calientes. En primer lugar, se determina un modelo digital de superficies (MDS) que será usado en el siguiente paso de generación de las ortoimágenes verdaderas de cada imagen. Finalmente se realiza la fusión de las ortoimágenes para generar una ortofoto.

El proceso automático de detección de puntos calientes se compone de la extracción de las geometrías de los paneles, la corrección de las imágenes termográficas, el análisis estadístico de las mismas, la detección de puntos calientes y la generación de informes periciales B.4. Para cada ortoimagen se realiza un filtrado para la eliminación de ruido, seguido de la búsqueda de contornos, la simplificación de estos con el algoritmo de simplificación de líneas de Douglas-Pecker y el filtrado basado en criterios geométricos y estadísticos. Los contornos resultantes constituyen los módulos del panel y mediante el algoritmo de agrupación espacial basado en la densidad (DBSCAN) se agrupan para obtener el contorno de las filas de paneles.

B.5.1. Arquitectura del software

SunMap sigue el mismo modelo basado en componentes siguiendo la arquitectura MVP tal y como se ha descrito previamente para el software GRAPHOS.
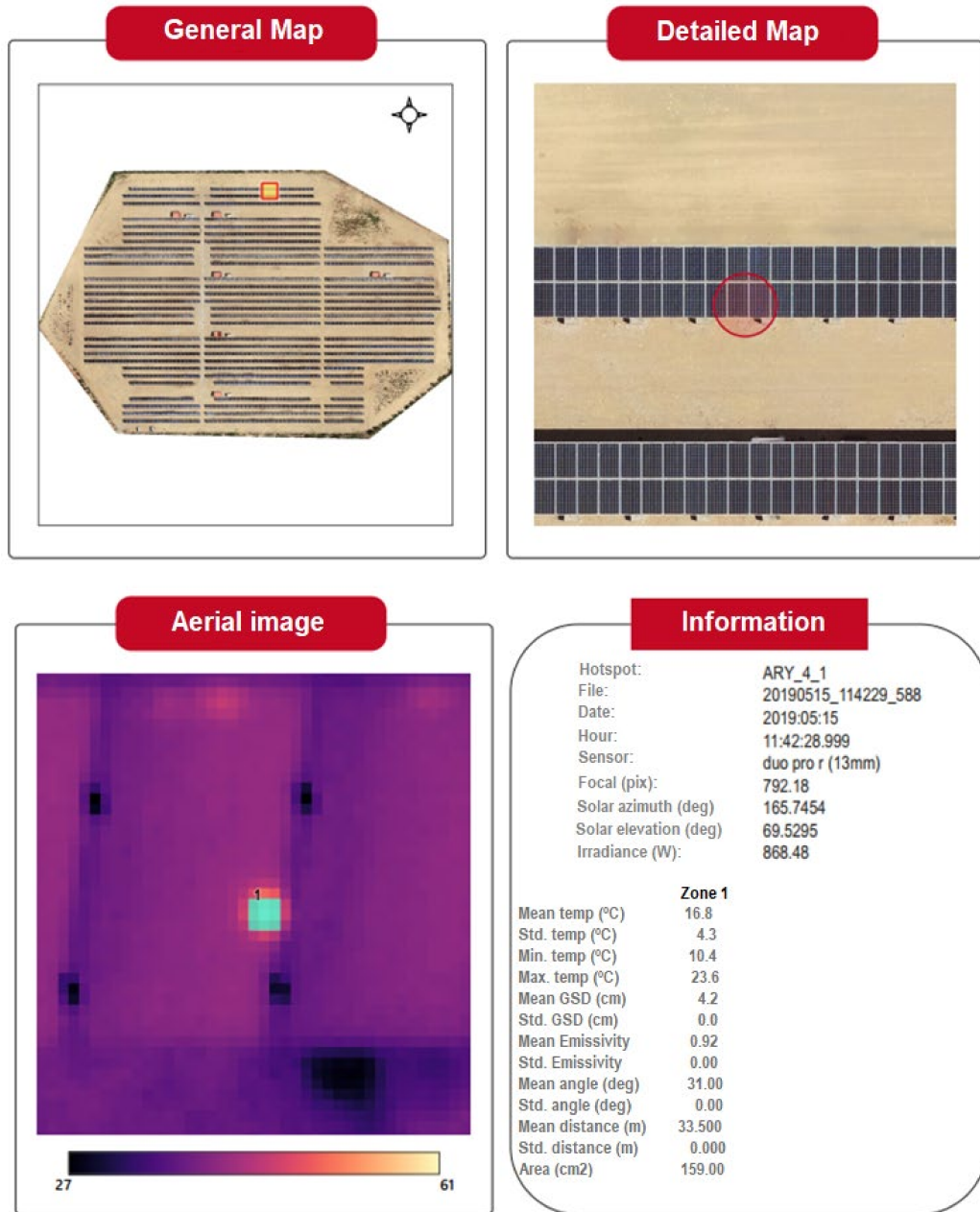
Figura B.4: Informe generado por SunMap

B.6. INSPECTORMAP

INSPECTORMAP es una IDE enfocada a la detección de masas de agua y cambios de la vegetación en las proximidades de las plantas fotovoltaicas desarrollada en el artículo *ÏNSPECTORMAP: A Spatial Data Infrastructure Applied to the Maintenance of Solar Plants Using Free Satellite Imagery"*.
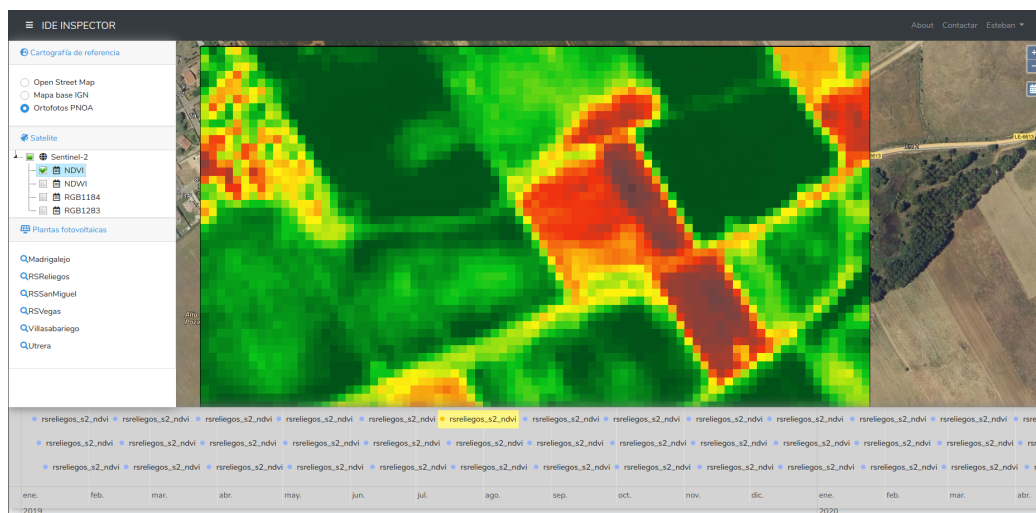

Figura B.5: Visor de la IDE INSPECTORMAP
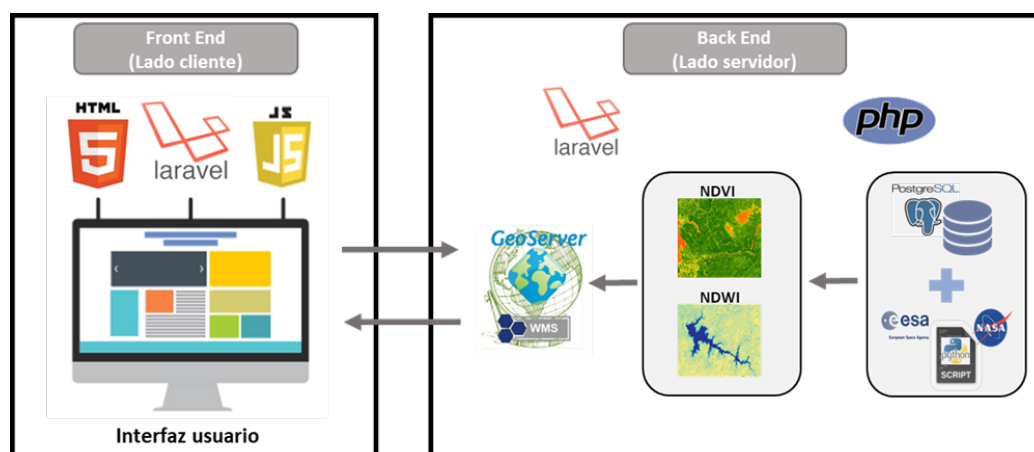
B.6.1. Arquitectura del software

Figura B.6: Arquitectura cliente-servidor

La IDE INSPECTORMAP está construida siguiendo la arquitectura cliente-servidor B.6 empleando el *framework* de desarrollo Laravel.

En el *backend*, un *script* de Python realiza la descarga, el recorte y el cálculo de los índices NDVI y NDWI de las imágenes Landsat-8 y Sentinel-2. Este *script* alimenta una base de datos PostgreSQL y el servidor GeoServer.

En la parte cliente (*frontend*) el usuario puede seleccionar el mapa base y los diferentes índices calculados B.5. En la parte inferior, en forma de calendario, el usuario puede ver y seleccionar las fechas para las que están disponibles las imágenes a partir de las cuales se ha realizado el cálculo de los índices. La parte principal de la Infraestructura de datos espaciales desarrollada es el visor de resultados, donde se muestran los índices espectrales calculados para la fecha seleccionada.

B.6.2. Dependencias

Las siguientes bibliotecas JavaScript han sido usadas en el desarrollo de la IDE:

- **OpenLayers**: Biblioteca JavaScript de código abierto, bajo licencia *BSD 2-Clause "Simplified"License*, para la visualización de la cartografía vectorial y ráster generada.

- **PROJ4JS**: Librería JavaScript de código abierto para la transformación entre diferentes sistemas de coordenadas.

- **VIS Timeline**: Biblioteca de código abierto distribuida bajo las licencias Apache 2.0 y MIT. Se utiliza su módulo *Timeline* para la visualización de los diferentes productos en una línea de tiempo o cronograma.

Para el desarrollo de la parte cliente también se utiliza el *framework* Lavavel, ya que incluye una serie de herramientas que facilita el trabajo con las bibliotecas JavaScript como son NPM y MIX. NPM es el sistema de gestión de paquetes por defecto para Node.js que permite instalar con un sencillo comando las dependencias. La herramienta MIX de Laravel permite hacer un empaquetado del código JavaScript y de las hojas de estilo propias empaquetando todo el código con sus dependencias, así como los estilos en dos únicos ficheros.